DOCTORAL DISSERTATION

Effect of membrane tension and pre-pore line tension on antimicrobial peptide PGLa-induced pore formation

June 2024

Department of Bioscience

Graduate School of Science and Technology,

Educational Division

Shizuoka University

MARZUK AHMED

CONTENTS

FIGURES

TABLES

Page No.

CHAPTER ONE: General Introduction

CHAPTER TWO: Role of membrane tension in antimicrobial peptide PGLa-induced pore formation

Table of symbols

β	Segment length of a hydrocarbon chain
Γ	Line tension at the pre-pore edge
γ	Free energy per unit area
δ	Change in fractional area of a GUV membrane
ε_w	Relative dielectric constant of water
ε_0	Permittivity of free space
κ_B	Bending rigidity
$\overline{\kappa_B}$	Gaussian curvature modulus
$1/\kappa$	Debye length of a solution
λ_B	Bjerrum length in water
μ_i	Chemical potential of lipids
Π	Osmotic pressure
Π_{head}	Repulsive pressure in lipid headgroup
Π_{chain}	Repulsive pressure in lipid chain region
ρ	Surface charge density
σ	Membrane tension
σ_{osm}	Membrane tension induced by osmotic pressure
τ	Mean-first passage time
φ	Flux of AF488 through the membrane
ψ	Electric potential
Ω	Free energy of a pre-pore
Ω_0	Nucleation free energy of a pre-pore
Ω_{max}	Maximum free energy of a pre-pore
ω	Ratio of the surface charge density of a pre-pore wall to that of the total bilayer
A	Total membrane area
a	Area per lipid molecule in a bilayer
B	Parameter of electrostatic interaction
b	Distance between the center of the neighboring cylinders in the H_{II} phase
b_L	Thickness of a lipid monolayer
C_{AF}	Concentration of fluorescent probe (AF488)
C_{AF}^{out}	Concentration of AF488 outside of a GUV
C_{in}^{0}	Osmolarity of the solution inside a GUV
C_{in}^{eq}	Osmolarity of the solution inside a GUV in equilibrium

C_{max}	Maximum curvature of a lipid monolayer
C_{min}	Minimum curvature of a lipid monolayer
C_{out}	Outside osmolarity of a GUV
ΔC^0	Osmolarity difference between the inside and outside of a GUVs
ΔC^{eq}	Osmolarity difference at equilibrium
D_v	Diameter of a GUV's spherical part outside of a micropipette
d_p	Internal diameter of a micropipette
E	Curvature elastic energy of a lipid monolayer
e	Elementary charge
F	Helmholtz free energy
F^{neu}	Helmholtz free energy of a neutral lipid bilayer
F_{ch}	Helmholtz free energy of a hydrocarbon chain
F_{min}	Minimum Helmholtz free energy
H	Mean curvature of a monolayer
H_0	Spontaneous curvature of a monolayer
h	Lipid bilayer thickness
I	Fluorescence intensity of a GUV lumen due to AF488 or AF647
I_N	Normalized fluorescence intensity of the GUV lumen
I_{lumen}	Intensity of the GUV lumen due to CF-PGLa
I_{rim}	Intensity of the GUV membrane due to CF-PGLa
J	Parameter describing repulsion between lipids
K^G	Gaussian curvature
K_{bil}	Elastic modulus of a lipid bilayer
k_B	Boltzmann constant
k_{leak}	Membrane permeability
k_{leak}^s	Membrane permeability at steady state
k_p	Rate constant of pore formation
k_p^{Mag}	Rate constant of nanopore formation induced by magainin 2
k_r	Rate constant of GUV burst
ΔL	Change in projection length of a GUV inside micropipette
l_{hc}	Length of a hydrocarbon chain
M	Number of independent experiments
m	Number of GUVs examined
N	Number of lipid molecules in a bilayer
n_s	Number of segments in a polymer chain

P	Coefficient of membrane permeability
P^{s}	Coefficient of membrane permeability at steady state
P_{B}	Fraction of GUV-burst
P_{LB}	Fraction of GUV-local-burst
P_{entry}	Fraction of cells with damaged cell membrane
P_{intact}	Fraction of intact GUVs
P_{leak}	Fraction of leaking GUVs
P_{single}	Fraction of dead cells
P_{trans}	Fraction of CF-PGLa translocated GUVs
ΔP	Pressure difference between the interior and exterior of a GUV
ΔP_{m}	Pressure difference between outside and inside of a micropipette
P_{out}	Pressure outside of a GUV
P_{in}	Pressure inside of a GUV
Q	Heat
R	Gas constant
R_{0}	Radius of spontaneous curvature
R_{SE}	Stokes-Einstein radius of fluorescent probes
R_{W}	Radius of curvature of lipid monolayer
r	Radius of a GUV
r_{0}	Initial radius of a GUV
r_{p}	Pre-pore radius
r_{p}^{*}	Threshold radius of a pre-pore
Δr	Change in radius of a GUV
S	Entropy of a lipid bilayer
S_{hc}	Entropy of a hydrocarbon chain
T	Absolute temperature
t	Time
U	Internal energy of a lipid bilayer
V	Volume of a GUV
V_{0}	Initial volume of a GUV
V_{hc}	Volume of a hydrocarbon chain
ΔV	Change in GUV volume
W	Work
W_{ch}	Total number of conformations of a hydrocarbon chain
X	Molar fraction of negatively charged lipid in a lipid bilayer

Table of abbreviations

AF488	Alexa Fluor 488 hydrazide
AF647	Alexa Fluor 647 hydrazide
AMPs	Antimicrobial Peptides
BSA	Bovine Serum Albumin
CF	5-(and 6)-carboxyfluorescein
CLSM	Confocal Laser Scanning Microscopy
CPPs	Cell Penetrating Peptides
DIC	Differential Interference Contrast
DIEA	Diisopropylethylamine
DMF	Dimethylformamide
DOPC	Dioleoyl-phosphatidylcholine
DOPG	Dioleoyl-phosphatidylglycerol
DOPE	Dioleoyl-phosphatidylethanolamine
EGTA	Ethylene glycol-bis(2-aminoethyl ether)-N ,*N,N′,N′* -tetraacetic acid
FLM	Fluorescence Microscopy
GUVs	Giant Unilamellar Vesicles
H_{II}	Hexagonal II phase
HBTU	2-(1H-benzotriazol-1-yl)-1,1,3,3-tetramethyl-uronium hexauorophosphate
HOBt	1- Hydroxybenzotriazole
HPLC	High-performance Liquid Chromatography
L_α	Liquid crystalline phase
LUVs	Large Unilamellar Vesicles
Mag	Magainin 2
MFPT	Mean-First Passage Time
MTBE	t-Butyl Methyl Ether
NBD-PE	1,2-dioleoyl-*sn*-glycero-3-phosphoethanolamine-N-(7-nitro-2-1,3-benzoxadiazole-4-yl
ND	Neutral Density
PGLa	Peptidyl-glycylleucine-carboxyamide
PC	Phosphatidylcholine
PE	Phosphatidylethanolamine

PG	Phosphatidylglycerol
PS	Phosphatidylserine
Q_{II}	Inverse bicontinuous cubic phase
R_9	Nona-arginine
SUVs	Small Unilamellar Vesicles
TFA	Trifluoroacetic acid
TP10	Transportan 10

CHAPTER ONE

General Introduction

1.1. Antimicrobial peptides (AMPs)

AMPs are heterogeneous collections of tiny molecules that are created by various living organisms (e.g., bacteria, plants, insects, and mammals). AMPs are defined as the peptides which have antimicrobial activities such as microbiostatic activity (e.g., bacteriostatic activity) and microbicidal activity (e.g., bactericidal activity). To date, over 3000 AMPs (https://aps.unmc.edu/) have been identified, exhibiting a diverse array of structural variations, but most AMPs often possess certain common traits such as highly positively charged peptides, amphipathicity, and a tendency to acquire secondary structures such as α-helices, β-sheets and closed configurations containing disulfide bonds (Zasloff, 2002). The emergence of antimicrobial resistance presents an imminent concern to worldwide public health, underscoring the pressing need for innovative antimicrobial medications. AMPs have attracted significant interest in this particular situation because of their wide range of antibacterial properties (i.e., the ability to kill or inhibit the growth of bacteria) and distinct methods of operation (Melo et al., 2009; Propheter et al., 2017).

It is considered that AMPs exert their effects on bacterial organisms through two primary mechanisms, and thus, AMPs can be classified into two groups (A and B). The mechanism for the group A is the binding and/or the disruption of microbial plasma membranes. For example, it has been reported that some AMPs induce influx or outflux of molecules such as fluorescent probes, indicating that these AMPs induce the creation of pores or the instability of membranes (Brogden, 2005; Hossain et al., 2019; Sochacki et al., 2011; Yeaman and Yount, 2003; Zasloff, 2002). Generally, the binding of proteins to plasma membrane necessitates their attachment to certain receptors there. However, AMPs consisting only of D-amino acids have similar antimicrobial activity to wild-type AMPs (Bobone and Stella, 2019; Wade et al., 1990; Wakabayashi et al., 1999). This suggests that AMPs target the lipid bilayer area in plasma membrane, since D-amino acid AMPs are unable to attach to receptors. Most AMPs belonging to this group A such as LL-37 derived from human cathelicidin, defensins, and magainin 2 (Mag) employ hydrophobic interaction and electrostatic interactions to bind to microbial membranes and perturb them (Schroeder et al., 2011; Sochacki et al., 2011; Zasloff, 2002). It has been an unresolved question whether AMPs-induced leakage of internal contents or damage of

Table 1.1: Different kinds of AMPs with their origins and structures

Name of AMPs	**Origin**	**Amino acid (aa) sequence**	**Structure**
Cecropin A	Silk moth	KWKLFKKIEKVGQNIRDGIIKAGPAV AVVGQATQIAKa	α-helix
Magainin 2	Frog	GIGKFLHSAKKFGKAFVGEIMN	
Dermaseptin	Frog	ALWKTMLKKLGTMALHAGKAALG AAADTISQGTQ	
LL-37	Human	LLGDFFRKSKEKIGKEFKRIVQRIKDF LRNLVPRTES	
Buforin II	Frog	TRSSRAGLQFPVGRVHRLLRK	
PGLa	Frog	GMASKAGAIAGKIAKVALKAL	
Bactenesin 1	Cow	RLCRIVVIRVCR	β-sheet
α-defensin	Human	DC1YC$_2$RIPAC$_3$IAGERRYGTC$_2$IYQGR LWAFC$_3$C$_1$	
Ranalexin	Frog	FLGGLIKIVPAMICAVTKKC	
Protegrin-1	Porcine	RGGRLC1YC2RRRFC2VC1VGRa	
Lactoferricin B	Bovine milk	FKCRRWQWRMKKLGAPSITCVRRAF	
Indolicidin	Cow	ILPWKWPWWPWRRa	Linear, non-α-helix
Histatin 5	Human	DSHAKRHHGYKRKFHEKHHSHRGY	

plasma membrane for a short time can cause the bacterial cell death or not. Recently, Islam et al. (Islam et al., 2023) tackled this important question using the single-cell analysis of antimicrobial activity, i.e., a new method of measurement of bacteriostatic and bactericidal activity of AMPs at single-cell level developed recently (Hossain et al., 2022), and found that a short interaction time with AMPs (Mag, lactoferricin B, and peptidyl-glycylleucine-carboxyamide (PGLa)) damages bacterial plasma membrane through which rapid membrane permeabilization occurs, which induces cell death. Significantly, the quick rate at which AMPs induce bacterial cell death makes them highly potential for fighting against drug-resistant microorganisms (Islam et al., 2023). On the other hand, the mechanism for the group B is the membrane permeation of the AMPs without disruption of microbial plasma membranes to enter the cytosol and the binding of important

biomolecules such as DNA and proteins (Hossain et al., 2021; Park et al., 2000).

1.2. Mag and PGLa as examples of AMPs in the group A

Here, I describe the characteristics of two AMPs as examples of the peptides belonging to the group A in details; Mag and PGLa. They have a common origin, i.e., the skin of the African clawed frog (*Xenopus laevis*) (Zasloff, 1987). They also have a common characteristic in their interaction with single *Escherichia coli* cells: a short time interaction (e.g., for minimum inhibitory concentration (MIC), 5 min) induces damage of their plasma membrane of most single cells, resulting in enhancing membrane permeation, which is a direct cause for the cell death of *E. coli* at single-cell level (Islam et al., 2023).

1.2.1. Magainin 2

Mag has an amino acid sequence of GIGKFLHSAKKFGKAFVGEIMNS (Zasloff, 1987). The studies using NMR spectroscopy indicate that Mag locates in the membrane interface as an α-helix and its orientation is parallel with the surface of a lipid bilayer (Bechinger et al., 1993; Hirsh et al., 1996; Strandberg et al., 2009). Based on its amino acid sequence and structure, this α-helix is an amphipathic one whose hydrophobic side faces the hydrophobic core of the lipid bilayer and hydrophilic side faces the membrane interface. On the other hand, the study using the neutron in-plane scattering indicates that most Mag molecules adopt a transmembrane orientation perpendicular to the membrane surface (Ludtke et al., 1996). According to a theory using elasticity of the membrane, the contradiction between the results obtained by NMR and by neutron scattering may be explained by the ratio of peptides to lipids, P/L, in the membrane: at low P/L the orientation of Mag molecules is parallel with the lipid bilayer surface, but high peptide concentrations most Mag molecules orient perpendicular to the membrane surface (Huang, 1995).

Many studies using a suspension of large unilamellar vesicles (LUVs) and small unilamellar vesicles (SUVs) indicate that Mag induces the leakage (or membrane permeation) of fluorescent probes such as calcein from the liposomes (Boggs et al., 2001; Gregory et al., 2009; Matsuzaki et al., 1998), suggesting that Mag induces damages in these liposome membranes. However, such method cannot provide the direct cause of the

leakage because various kinds of factors can induce leakage (Yamazaki, 2008). In contrast, the studies using the single giant unilamellar vesicle (GUV) method can provide the direct cause of AMPs-induced leakage and the information on the elementary processes of AMPs-induced damage in GUV membranes (Islam et al., 2014). The studies using the single GUV method indicate that Mag induces nanopore formation in the bilayer composed of electrically neutral dioleoylphosphatidylcholine (DOPC) and negatively charged dioleoylphosphatidylglycerol (DOPG) (Tamba and Yamazaki, 2005). In this single GUV method, the onset time of pore formation in each GUV is determined from the onset time of leakage of fluorescent probe from the GUV, and the statistical analysis of the onset time of pore formation in many GUVs provides the information on the rate constant of Mag-induced nanopore formation (k_p^{Mag}) as the two-state transition from the intact GUV to the pored GUV (Tamba and Yamazaki, 2005). The value of k_p^{Mag} increases with increasing electrostatic interaction owing to the surface charges of lipid bilayers due to DOPG, and the quantitative analysis of this phenomenon revealed that the determining factor of k_p^{Mag} is the Mag concentration in the membrane interface (or surface concentration) (Tamba and Yamazaki, 2009). The interaction between Mag and DOPC/DOPG-GUVs results in an increase in the GUV membrane area (and thus, its fractional area change, δ), which is directly related to the Mag surface concentration, and the value of k_p^{Mag} increases with increasing δ, indicating that Mag-induced pore is stretch-activated (Karal et al., 2015a). The observation of the interaction of fluorescence probe-labeled Mag with single DOPC/DOPG-GUVs using confocal laser scanning microscopy (CLSM) can reveal the existence position of Mag in the GUV and its relation to Mag-induced pore formation: Mag molecules are transferred from the outer to the inner monolayer just before the leakage of fluorescent probes (Karal et al., 2015a). This result demonstrates that the asymmetric binding of Mag to the GUV bilayer (i.e., only outer monolayer) induces pore formation (Levadnyy et al., 2019).

1.2.2. PGLa

PGLa has an amino acid sequence of GMASKAGAIAGKIAKVALKAL (Hoffmann et al., 1983). The studies using NMR spectroscopy indicate that PGLa locates in the

membrane interface as an α-helix and its orientation is parallel with the surface of a lipid bilayer (S-state) at low peptide concentration (the ratio of peptides to lipids, P/L, is 1/200) but tilted against the membrane surface at an oblique angle about 125° (T-state) at high peptide concentrations (P/L = 1/50 and 1/35) (Bechinger et al., 1998; Glaser et al., 2005; Tremouilhac et al., 2006). Based on its amino acid sequence and structure, PGLa adopts an amphipathic α-helix. Thus, the helix at the C-terminus is located in the membrane surface at S-state and inserted into the bilayer at T-state, while the N-terminus stays firmly in the membrane interface at both states.

Many studies using a suspension of small liposomes indicate that PGLa induces the leakage from the liposomes. For example, the interaction of PGLa with SUVs comprising a ternary mixture of lipids (brain PC/brain phosphatidylethanolamine (PE)/brain phosphatidylserine (PS)) caused the release of carboxyfluorescein from the interior of the vesicles within short time (Williams et al., 1990). The quenching of calcein by Co^{2+} was another way to test the PGLa-induced membrane permeability for SUVs (Vaz Gomes et al., 1993). PGLa also induces leakage of fluorescent probes from LUVs composed of bacterial lipids (Blazyk et al., 2001). These results suggest that PGLa induces damages in these liposome membranes.

The studies using the single GUV method indicate that PGLa induces pore formation in DOPC/DOPG-GUVs and the rate of PGLa-induced pore formation is enhanced as PGLa concentration is increased (Parvez et al., 2018). The observation of the interaction of fluorescence probe-labeled PGLa with single DOPC/DOPG-GUVs using CLSM revealed that PGLa transfers from the outer to the inner monolayer without pore formation until its concentrations in both monolayers are the same, and after this symmetric binding remains for an extended time, pore formation occurs (Parvez et al., 2018). This result demonstrates that the symmetric binding of PGLa to the GUV bilayer (i.e., equal binding to both monolayers) induces the pore formation. This transfer of PGLa without pore formation was also detected in the interaction of label-free PGLa with same GUVs, indicating that this phenomenon is not due to the labeling of fluorescent probe to the peptides (Ali et al., 2021).

1.3. Membrane tension of cells and lipid vesicles

As described in the above sections, the target of AMPs belonging to the group A is the lipid bilayer region of bacterial plasma membrane. Thus, various physical properties of lipid bilayer can affect the interaction of AMPs with the lipid bilayers and AMPs-induced damage of the lipid bilayers such as pore formation. Lipid bilayers can be divided into two membrane interfaces and one hydrophobic core (Fig. 1.1 (a)). The membrane interface is composed of hydrophilic segments of lipids (so-called lipid headgroup), hydrocarbon chains of lipids (so-called lipid tails) and water molecules. At the membrane interface, there is a repulsive interaction between the neighboring lipid headgroups that originates from interchain interaction of hydrophilic segments (entropic effect), hydration of the hydrophilic segments, steric-hydration forces, and electrostatic interaction. Generally, the repulsive pressure between the headgroups in the membrane interface owing to these various causes is expressed as Π_{head}. The hydrophilic segment of lipids is a short polymer chain, and thus, the entropy of the conformation of chain decreases as the distance between neighboring lipids decreases, inducing a repulsive force. In the liquid-crystalline (L_α) phase, water content in the membrane interface is large. Among them, some water molecules interact with the hydrophilic segments, resulting in a limited excluded volume of the segment forces (Israelachvili, 2011). It is considered that these water molecules are strongly structured near the hydrophilic segment (Rand and Parsegian, 1989), and thus, this hydration contributes the repulsive interaction between the hydrophilic segments when water content in the membrane interface becomes very small. When thermal fluctuations of lipid molecules and lipid bilayers such as protrusion of lipids and undulation of lipid bilayer is large, steric-hydration forces also appear (Ayala et al., 2023; Matsuki et al., 2019; Shkulipa et al., 2006), which contributes significantly the intermembrane repulsive interaction. However, it is not sure whether these fluctuations contribute to the interlipid interaction in the same monolayer. On the other hand, among biological lipids, several lipids (such as PG and PS) have net negative charges, whereas the other lipids (such as PC and PE) do not have net charges but have an electric dipole moment. Repulsive force between negatively charged lipids is induced. Besides, the electrostatic interaction also depends on the pH (Lowe et al., 2022; Petelska and Figaszewski, 2002) and ionic concentration of the solution (Lin and Alexander-Katz,

2016; Träuble and Eibl, 1974).

In contrast, at the interface between the hydrophobic core and the membrane interface, a strong attractive interaction between neighboring lipids exists due to hydrophobic interaction between the lipid hydrocarbon chains and water, which is responsible for the membrane's cohesiveness. This attractive lateral tension, γ, can be considered the interfacial tension in lipid bilayers, which has another physical meaning: free energy per unit area. A typical value of γ is 39 mJ m^{-2} (Marsh, 1996). Furthermore, the entropic and steric interactions between the hydrocarbon chains in the hydrophobic core are responsible for a repulsive pressure, Π_{chain}. At mechanical equilibrium, the attractive lateral tension is counterbalanced by the repulsive lateral pressure in the membrane interface and hydrophobic cores (Anishkin et al., 2014; Marsh, 2007), i.e., $\gamma = \Pi_{head} + \Pi_{chain}$. Under this mechanical equilibrium, lipid molecules have a specific area per lipid, called optimal area.

If an external force is applied to a lipid bilayer in the direction parallel with the membrane surface, the lipid bilayer is stretched, and thus, the above mechanical equilibrium is broken. As a result, the area per lipid increases from the optimal area, which induces a lateral positive tension that tends to compress the membrane laterally. This lateral tension is defined as membrane tension, σ. The direction of membrane tension is depicted in Fig. 1.1(b).

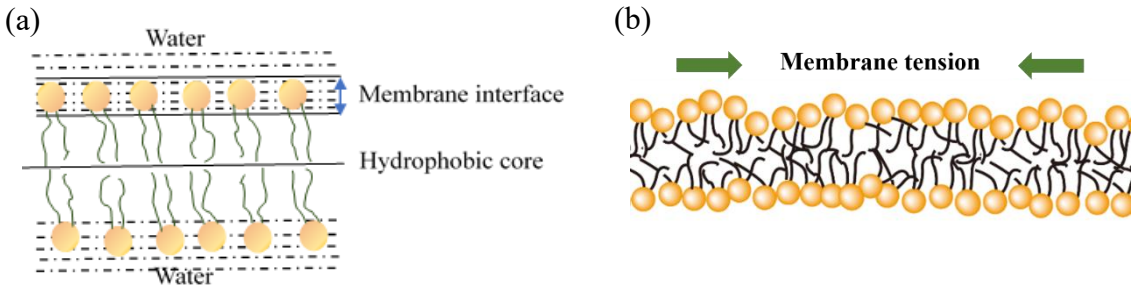

Figure 1.1: Scheme of a lipid bilayer. (a) A small area of a lipid bilayer showing membrane interface and hydrophobic core region in aqueous environment. (b) Direction of membrane tension in a lipid bilayer.

It has been reported that the membrane tension effect is substantial in the activity of mechano-sensitive ion channels and other membrane proteins (Levina et al., 1999;

Rangamani, 2022; Sachs, 2010; Sukharev et al., 1994) as well as mechanical properties of plasma membrane and lipid bilayers such as pore formation (Ahmed et al., 2024b; Akimov et al., 2017; Fuertes et al., 2011; Karal et al., 2015a; Moghal et al., 2020). A number of methods such as the tether force method with laser tweezers (Dai and Sheetz, 1999) and the micropipette aspiration method (Hochmuth, 2000; Levadny et al., 2013), and other approaches (Karatekin et al., 2003; Mou et al., 2023; Sandre et al., 1999), are used to quantitatively regulate and create membrane tension. The micropipette aspiration technique is a key approach used in cellular biomechanics research to study the mechanical characteristics of cells and their components. In its standard method, cells and GUVs are held at the edge of a micropipette using a precise aspiration pressure (ΔP_m). An adjustable water reservoir or pump is used to provide ΔP_m (González-Bermúdez et al., 2019). This procedure applies (lateral) membrane tension, σ, to cells and vesicles, and its magnitude is expressed by ΔP_m as follows.

$$\sigma = \frac{\Delta P_m d_p}{4\left(1 - \frac{d_p}{D_v}\right)} \tag{1.1}$$

where, $\Delta P_m = P_{out} - P_{in}$ (P_{out} and P_{in} are the pressure outside and inside a micropipette, respectively), d_p is the micropipette inner diameter, and D_v is the diameter of the cell or GUV outside the micropipette after applying tension.

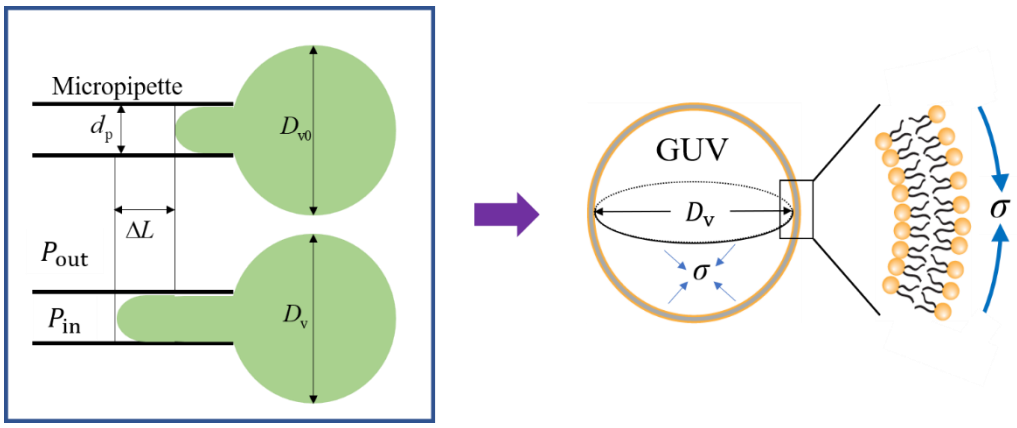

Figure 1.2: Micropipette aspiration of a GUV applying tension to the membrane. Left: A GUV is held at the micropipette tip of diameter d_p by aspiration pressure where D_{v0} and D_v are the diameter of the GUV before and after applying σ. Right: Membrane tension, σ is induced in the membrane by the aspiration pressure.

In the measurement of elastic modulus, when membrane tension reaches a critical one, a GUV or a cell is sucked into the inside of micropipette completely because large membrane tension induces pore formation in their membrane, resulting in their burst. This tension inducing their aspiration provides a measure of the mechanical strength of lipid bilayers or plasma membrane, which ranges 1–25 mN/m for lipid bilayers, depending on lipid compositions and measuring techniques (Evans et al., 2003; Hallett et al., 1993; Li et al., 2014; Mui et al., 1993; Needham and Nunn, 1990). The micropipette aspiration technique also allows researchers to determine viscoelasticity (Evans and Rawicz, 1990), membrane dynamics (Hochmuth, 2000), and deformability of cells (Guo et al., 2012).

It is well known that osmotic pressure (Π) induces swelling (under hypotonic condition) or shrinkage (under hypertonic condition) of cells and lipid vesicles, resulting in membrane tension. However, the value of the membrane tension in LUVs has not been accurately measured experimentally (see the details in Shibly et al., 2016). Recently, membrane tension values of GUVs under osmotic pressure (hypotonic condition) has been successfully estimated by applying the constant-tension-induced GUV burst method (Shibly et al., 2016; Saha et al., 2020). This estimation method has been applied to determine the negative membrane tension of GUVs under hypertonic condition (Ahmed et al., 2024a). As described in the following section, the micropipette aspiration method has a disadvantage for elucidation of the membrane tension effect of AMP activity. However, the method of application of membrane tension due to osmotic pressure (i.e., the Π method) can conquer this disadvantage of the micropipette aspiration method (Billah et al., 2022). Therefore, the Π method may be a promising method to reveal the membrane tension effect of the AMPs-induced damage of lipid bilayers such as pore formation.

1.4. Role of membrane tension in the AMPs-induced pore formation

The membrane tension effect of Mag-induced pore formation was examined by applying the micropipette aspiration method (Karal et al., 2015a). In the interaction of Mag with a GUV under membrane tension due to the aspiration by a micropipette, the GUV was sucked into the inside of the micropipette completely immediately after the

Mag-induced nanopore formation in the membrane. This phenomenon can be explained as follows. After Mag induces nanopore formation in the membrane, membrane tension expands the pore diameter, resulting in GUV burst and aspiration into the micropipette. Based on this interpretation, the onset time of pore formation was determined as the time of the aspiration because the aspiration completes within 1 s. The statistical analysis of the onset time of many GUVs provided the rate constant of Mag-induced pore formation, k_p^{Mag}. As membrane tension was enhanced, the k_p^{Mag} increased. However, the characteristics of a pore and the change of the pore over time were not revealed.

Osmotic pressure in a hypotonic solution is reported to affect the interaction of lytic peptides with LUVs (Polozov et al., 2001). This result can provide the qualitative information on the role of membrane tension in the activity of lytic peptides, but it is difficult to determine the accurate of membrane tension and to reveal which process of the leakage is affected by tension. To overcome the disadvantages of the micropipette aspiration technique and the application of osmotic pressure to LUVs, the Π method was developed to examine the membrane tension effect of Mag-induced nanopore formation in DOPC/DOPG (4/6)-GUV (Billah et al., 2022). In this experiment, the GUVs were able to be observed after the leakage of fluorescent probe from the GUV started, i.e., Mag-induced nanopore formation initiated, indicating that the evolution of pores can be followed. When small membrane tension was applied to a GUV, the size and the shape of the GUV did not change after Mag-induced pore formation, indicating that nanopore formation occurred, but the k_p^{Mag} was elevated. However, when the value of applied membrane tension was increased, certain GUVs were converted to lipid aggregates after the leakage. Such phenomenon is called GUV burst (Billah et al., 2024). Observation of the Mag-induced GUV burst using the labeling of the membrane by a fluorescent lipid at a high time resolution (10 ms) provided its detailed process as follows (Fig. 1.3). Initially, the GUV membrane emits fluorescence homogenously due to the fluorescent probe. After starting the interaction, suddenly a tiny micropore (~ 0.5 μm in diameter), represented as a black part in the bright GUV membrane (indicated by a white arrow), forms in the membrane, and then the radius of this micropore expands over a period of approximately 100 ms without affecting the diameter of the GUV. Afterwards, the fluorescence intensity at the edge of the pore increased with time, indicating that membrane folding occurs there.

The results can be interpreted reasonably as follows. First, Mag induces a nanopore formation. Membrane tension increases its radius, which converts the nanopore to a micrometer-sized pore (i.e., micropore). The radius of a micropore continues to increase until the membrane tension becomes 0. Since a Mag-induced pore is a toroidal pore, and thus, its radius can easily change because the size of the pore is not fixed. Therefore, the Π method successfully provided the quantitative information on the effect of membrane tension on Mag-induced pore formation such as k_p^{Mag} and the evolution of Mag-induced nanopore.

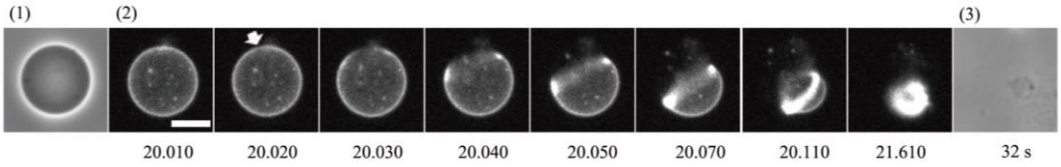

Figure 1.3: Changes in shape and structure of a GUV interacting with Mag when GUV burst occurs under osmotic pressure. This figure is reprinted from ref. (Billah et al., 2022), with permission from the Royal Society of Chemistry.

1.5. Line tension in lipid membrane

Interfacial tension, or surface tension arises when two different 3-dimensional substances contact each other, especially surface tension between liquid (or solid) and gas is well known. In this case, the 2-dimensional contact region has an extra free energy per unit area, which tends to decrease its area. Similarly, when two different 2-dimensional substances contact each other, the 1-dimensional contact line has an extra free energy per unit length, called line tension, which tends to decrease the length of the contact line. Thus, the line tension has a unit of J m^{-1} or N.

Line tension plays various roles in biomembranes and lipid bilayers. The clear example can be seen in the phase separation or domain formation in biomembranes and lipid bilayers. When two regions composed of different lipid compositions contact each other, line tension is produced in the contact line of two regions. It is considered that the production of membrane protrusions and invaginations is facilitated by domain borders, so enabling cellular functions such as endocytosis and exocytosis (Baumgart et al., 2003).

Another example of line tension in biomembranes and lipid bilayers can be seen when a pore is formed in the membrane. In this case, inside the pore water region exists, whereas the outside of the pore is lipid bilayers or proteins/peptides comprising the pore, and thus, the edge (or the rim) of a pore has line tension. For example, when a large force is applied to a GUV due to a photochemical reaction, a micropore is formed in the GUV membrane (Brochard-Wyart et al., 2000). This micropore is composed of only lipid bilayers, and thus, sometimes called a lipidic pore. The line tension of the edge of such a lipidic micropore is large, and thus, the pore closes rapidly if the membrane tension disappears immediately after the pore formation. The analysis of the decrease in the micropore diameter can provide the values of line tension at the micropore edge (Brochard-Wyart et al., 2000). It is considered that the micropore edge has a toroidal pore structure, whose edge is composed of the curved monolayer connected to the outer and the inner monolayers.

It is well known that when a large force stretches a lipid bilayer, a pore is formed. As a mechanism underlying the pore formation induced by tension, a following model has been considered. In the L_α phase, thermal force induces the fluctuation of lipid density laterally in the lipid bilayers (Fig. 1.4). In some cases, a nanometer-sized region with lower density is transiently formed, which is called a pre-pore (Evans et al., 2003; Glaser et al., 1988). In most cases, this pre-pore is so unstable that it closes rapidly, but if a pre-pore with larger radius is formed, this pre-pore is converted to a pore. Two structural models for a pre-pore have been considered: one is the hydrophobic pre-pore where its edge is composed of lipid hydrocarbon chains and the other is the hydrophilic pre-pore where its edge is composed of the lipid hydrophilic segments (its typical structure is a toroidal pore structure (Fig. 1.4 (a)) (Glaser et al., 1988; Karal and Yamazaki, 2015). The values of line tension of the edge of a pre-pore has been estimated by the constant-tension-induced GUV burst (Karal et al., 2015b; Levadny et al., 2013; Tazawa and Yamazaki, 2023) and by the dynamic tension spectroscopy (Evans et al., 2003; Evans and Smith, 2011). The line tension of a pre-pore edge depends on the length and the number of double bonds of lipid hydrocarbon chains (Evans et al., 2003) and the monolayer spontaneous curvature (Tazawa and Yamazaki, 2023).

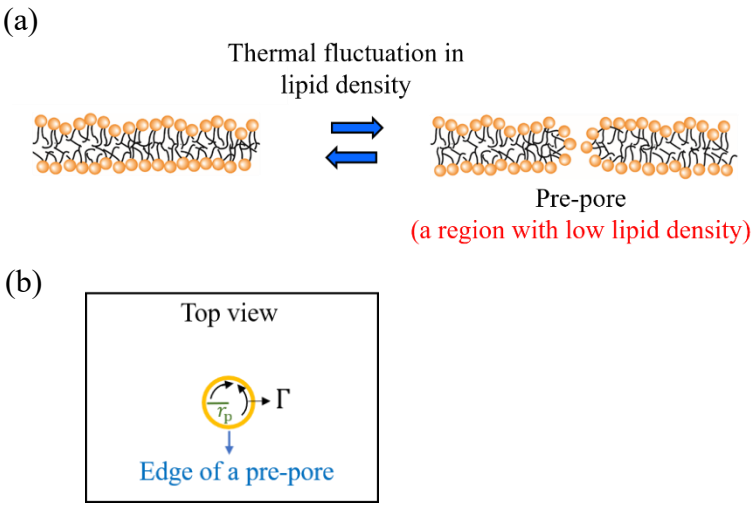

Figure 1.4: Structure of a Pre-pore and its line tension. (a) Formation of a pre-pore due to thermal fluctuation in lipid molecules in a bilayer membrane (side view). (b) Top view of a pre-pore showing line tension, Γ at the edge of a pre-pore of radius r_p.

The energy barrier of constant tension-induced pore formation decreases with decreasing line tension, and thus, the rate constant of constant tension-induced GUV burst increases with a decrease in line tension (Sharmin et al., 2016; Tazawa and Yamazaki, 2023). It is considered that cell-penetrating peptides (CPPs) can be transferred across lipid bilayers. One of the mechanisms underlying the transfer of CPPs can be explained by the pre-pore model (Islam et al., 2018, 2017; Sharmin et al., 2016). A CPP molecule bound in the outer monolayer can bind to a pre-pore rim located at the position of CPP, which stabilizes the pre-pore edge, resulting in decrement of the line tension. CPP molecules can diffuse from the membrane surface at the pre-pore edge of toroidal structure, to the inner monolayer.

1.6. Purpose of the thesis

A recent study using the single-cell analysis of antimicrobial activity and cell membrane damage demonstrates that after interaction of single *E. coli* cells with PGLa for a specific time t ($\leq$ 5 min), the values of fraction of dead cells, P_{single} (t), are similar to the values of fraction of cells with damaged cell membrane, P_{entry} (t), indicating that a

short-time interaction of PGLa with single cells damages their cell membrane, inducing their cell death (Islam et al., 2023). It is well recognized that most AMPs target the lipid bilayer region in plasma membrane. Moreover, it is reported that PGLa forms nanopores in the interaction with DOPC/DOPG (6/4)-GUVs (Parvez et al., 2018). Therefore, to elucidate the mechanism underlying the PGLa-induced nanopore formation in lipid bilayers, it is indispensable to elucidate the effect of physical properties of lipid bilayers on the pore formation. Among the physical properties, here I focus on membrane tension and line tension at the pre-pore edge. As described in the sections 1.3 and 1.4, the micropipette aspiration method is the standard method to apply membrane tension to cells and GUVs, but cannot be used for the studies on the interaction of AMPs with GUVs due to a serious problem. A new osmotic pressure (Π) method has conquered this problem, and thus, it was applied to the studies of the interaction of Mag with a lipid bilayer (Billah et al., 2022). Membrane tension (σ) enhances the rate constant of Mag-induced nanopore formation and converts a nanopore to a micropore, resulting in GUV burst. However, the effect of σ on PGLa-induced nanopore formation has not been elucidated yet. On the other hand, the line tension at the pre-pore edge (Γ) plays an important role in the tension-induced GUV burst, stability of a micropore in lipid bilayers, and the interaction of CPPs with lipid bilayers. It is expected that the line tension affects the PGLa-induced nanopore formation. In this thesis, I investigated the effect of σ and Γ on PGLa-induced nanopore formation in single GUVs and the evolution of the nanopore.

(Chapter two) Using the Π method developed recently (Billah et al., 2022), I examined the role of σ in the PGLa-induced nanopore formation by fluorescence microscopy. As described in section 1.4, the Π method can provide the quantitative value of σ in GUVs and enables to observe directly the AMP-induced pore formation in a GUV with membrane tension and the pore evolution. First, I examined the PGLa-induced membrane permeation of fluorescent probe, AF488, from a DOPC/DOPG (6/4)-GUV under Π. By analyzing these results, I obtained the information on the effect of σ and/or Π on the rate of PGLa-induced nanopore formation and the membrane permeability coefficient of AF488. The location of AMPs in the GUV membrane plays an important role in the AMPs-induced nanopore formation. It was reported that PGLa transfers across a lipid

bilayer without pore formation and the resulting symmetric binding of PGLa across the bilayer is required for the nanopore formation (Parvez et al., 2018). To elucidate the location of PGLa during the PGLa-induced nanopore formation, I investigated the interaction of a mixture of fluorescent probe-labeled PGLa and label-free PGLa with single GUVs under Π using CLSM. By analyzing these results, I obtained the information on the effect of σ on the rate of transfer of PGLa across lipid bilayers. Finally, I discussed the mechanism underlying the role of σ on PGLa-induced nanopore formation and the transfer of PGLa across a lipid bilayer. I also compared the effect of σ on nanopore formation by PGLa and its evolution with those induced by Mag, and discussed the mechanism underlying the difference.

(Chapter three) I investigated the effects of Γ on PGLa-induced nanopore formation. A recent study demonstrated that the Γ depends greatly on the monolayer spontaneous curvature, and thus, the Γ of DOPE/DOPG (6/4) (15.6 pN) is much larger than that of DOPC/DOPG (6/4) (10.7 pN) (Tazawa and Yamazaki, 2023). Thus, I selected these two lipid compositions for this research, and investigated the interaction of PGLa with single GUVs. Firstly, I examined the PGLa-induced AF488 membrane permeation from DOPE/DOPG (6/4)-GUVs. I found that PGLa induces nanopore formation in DOPE/DOPG (6/4)-GUV as well as GUV burst, where rapid membrane permeation occurs concomitantly with a significant decrease in GUV diameter. Then, to reveal the mechanism underlying the PGLa-induced nanopore formation and GUV burst, I examined the connection between the binding of PGLa in the lipid bilayer and AF647 membrane permeation in DOPE/DOPG (6/4)-GUVs. To clarify the process of the GUV burst in detail, I observed the PGLa-induced structural change of the GUVs at a high time resolution (10 ms). To reveal the effect of Γ, I compared all the results of DOPE/DOPG (6/4)-GUVs with those obtained for DOPC/DOPG (6/4)-GUVs (Chap. 2). Based on the obtained results, I discussed the mechanisms underlying the effect of Γ on PGLa-induced nanopore formation.

CHAPTER TWO

Role of membrane tension in antimicrobial peptide PGLa-induced pore formation

2.1. Introduction

As described in the previous chapter, AMPs have the ability to disrupt the integrity of the cell membrane in bacterial cells (Sochacki et al., 2011; Yeaman and Yount, 2003; Zasloff, 2002). Membrane tension (σ) is one of the important physical quantities governing the mechanical characteristics of biomembranes and lipid bilayers (Evans et al., 2003; Karal et al., 2015b; Karatekin et al., 2003), as well as influencing the functionality of mechanosensitive ion channels and other proteins interacting with plasma membranes (Rangamani, 2022; Sachs, 2010). The micropipette aspiration method (Evans et al., 2003; Karal et al., 2015b) is often used to apply membrane tension to cells and GUVs. This approach involves applying aspiration pressure to produce membrane tension. Nevertheless, when this technique was used to investigate the impact of σ on pore formation induced by Mag in a GUV, the prompt aspiration of the GUV occurred entirely into the micropipette after pore formation, rendering the observation of the pore and its progression unattainable (Karal et al., 2015a).

To overcome the disadvantages of this method, the Π method was developed to examine the quantitative effect of σ on the activities of peptides/proteins interacting with lipid bilayers, and successfully applied to the investigation of the impact of σ on Mag-induced nanopore formation in DOPC/DOPG (4/6)-GUV (Billah et al., 2022). It was possible to directly observe the Mag-induced pore formation and the evolution of the pore.

To reveal the mechanism underlying the action of AMPs against lipid bilayers, it is vital to elucidate the effect of σ on AMPs-induced pore formation or membrane damage. In the Chap.2, I used the Π method to reveal the effect of σ on the PGLa-induced nanopore formation in DOPC/DOPG (6/4)-GUVs. To apply Π to GUVs, I transferred the GUVs whose lumen contains water-soluble fluorescent probes AlexaFluor 488 or 647 hydrazide (AF488 or AF647) into the same buffer with lower osmolarity. Under this condition, I made the experiments of the interaction of PGLa with single DOPC/DOPG (6/4)-GUVs using the single GUV method and obtained the information on the Π effect on the rate of pore formation and the membrane permeability coefficient. To elucidate the mechanism underlying the AMP-induced pore formation, it is indispensable to reveal the location of AMP in lipid bilayers before pore formation. It is reported that PGLa transfers across a lipid bilayer without nanopore formation (Parvez et al., 2018), indicating the symmetric binding of PGLa in a lipid bilayer induces nanopore formation. Thus, to elucidate the

mechanism of the effect of osmotic pressure on PGLa-induced nanopore formation, it is essential to reveal the effect of osmotic pressure on the location of PGLa in a GUV during their interaction and on the transfer of PGLa across the GUV bilayer. To examine the location of PGLa in a GUV, I used fluorescence probe (5-(and 6)-carboxyfluorescein, CF)-labeled PGLa (CF-PGLa) for observation of the interaction of PGLa with single GUVs using CLSM. Finally, I discussed the mechanism of the effect of σ on PGLa-induced nanopore formation and PGLa transfer across the GUV bilayer.

2.2. Materials and methods

2.2.1. Chemicals

DOPC and DOPG were purchased from Merck & Co. (Avanti Polar Lipids Inc.) (NJ, USA). CF succinimidylester, AF488 and AF647 were purchased from Thermo Fisher Scientific. (Invitrogen) (MA, USA). Bovine serum albumin (BSA) was purchased from FUJIFILM Wako Chemical Co. (Osaka, Japan). EGTA (ethylene glycol-bis(2-aminoethyl ether)-N *,N,N′,N′* -tetraacetic acid) was purchased from Dojindo Molecular Technologies, Inc. (Kumamoto, Japan). Various Fmoc-amino acids, 1-Hydroxybenzotriazole (HOBt) and 2- (1H-benzotriazol-1-yl)-1,1,3,3-tetramethyl-uronium hexauorophosphate (HBTU) were bought from Peptide Institute Inc. (Osaka, Japan).

2.2.2. GUV synthesis and purification

GUVs containing AF488 and AF647 in their lumen were used for the experiments of PGLa-induced leakage using FLM and for the experiments of PGLa transfer across the GUV membrane using CLSM, respectively. Natural swelling method (Billah et al., 2022; Parvez et al., 2018; Tamba et al., 2011) was used to prepare DOPC/DOPG (6/4)-GUVs described as follows. At first, 120 μL DOPC (1 mM chloroform solution) and 80 μL DOPG (1 mM chloroform solution) (molar ratio = 6/4) were taken in a 5 mL glass vial by a pipetman (Gilson, WI, USA) and mixed gently. To evaporate chloroform, this mixture was placed under a mild flow of N_2 gas. Afterwards, the glass vial was kept inside a vacuum desiccator, which was evacuated by a rotary vacuum pump (GCD-051X, ULVAC, Nagoya, Japan) overnight, resulting in dried lipid sheets on the glass surface.

These dry lipid sheets were pre-hydrated by addition of 20 μL Milli-Q and the following incubation at 45–47 °C for 7 min. This step induces the swelling of the lipid multilayer, which facilitates the formation of unilamellar vesicles. Next, 1.0 mL buffer (10 mM PIPES, 150 mM NaCl and 1 mM EGTA; pH 7.0) comprising sucrose (100 mM) and 6 μM AF488 (or AF647) was added to the pre-hydrated lipid sheets and incubated at 37 °C for 2.5 h. The osmolarity of the solution (C_{in}^0 = 388 mOsm L^{-1}) was calculated by the previously described method (Saha et al., 2020). Then, this solution was centrifuged at 14000 g × 20 min at 20 °C by a centrifuge (himac CF 15R, Hitachi, Japan) to remove lipid membrane aggregates. Its supernatant is a GUV suspension, but it contains various impurities such as fluorescent probes, LUVs, and small GUVs. The membrane filtering method (Tamba et al., 2011) was applied to purify the GUV suspension. Briefly, the supernatant was passed through a 10 μm pore sized polycarbonate membrane (Whatman, Buckinghamshire, UK) at a flow rate of 1 mL min^{-1} for 50−60 min. Buffer containing 93 mM glucose (osmolarity, C_{out} = 388 mOsm L^{-1}) was used as a bulk solution for the purification to eliminate the osmotic pressure effects at this step. Finally, the unfiltered solution (i.e., purified GUV solution) was collected and used for experiments.

2.2.3. Method of applying Π to GUVs

To apply Π to the GUVs, an amount of purified suspension of DOPC/DOPG (6/4)-GUVs (C_{in}^0) was mixed with a hypotonic glucose solution in buffer inside an eppendorf tube (final osmolarity outside the GUVs: C_{out}) and incubated until the swelling equilibrium is reached. The osmolarity difference between the inside and outside of the GUVs, ΔC^0 (= $C_{in}^0 - C_{out}$) produces an osmotic pressure ($\Pi = RT\Delta C^0$, where R is the gas constant and T is absolute temperature). The unit of osmolarity used here is 'mOsm L^{-1}', which is identical to mM or mol m^{-3}. At swelling equilibrium, membrane tension was induced in the GUV bilayer. According to the theory developed in the ref. (Saha et al., 2020), the value of membrane tension can be obtained quantitatively (see the details in the following section 2.3.2).

2.2.4. Synthesis, purification, and identification of PGLa and CF-PGLa

PGLa with the amino acid sequence (GMASKAGAIAGKIAKVALKAL-NH_2) was

synthesized by the peptide synthesizer (Initiator+ Alstra, Biotage, Uppsala, Sweden) using the FastMoc method. Trifluoroacetic acid (TFA) was used for the cleavage of peptides from the amide resin and the deprotection of side chains. A cleavage TFA solution contains 0.75 g phenol, 0.25 mL 1,2- ethanedithiol, 0.5 mL thioanisole, 0.5 mL Milli-Q (for 10 mL TFA), which are used as scavengers to prevent the production of byproducts of peptides and to protect the side chain groups from their oxidation and alkylation by chemical reaction. A cleave solution was added on peptide resin (e.g., 100 mg) at low temperature (~ 4°C), which was kept for 10 min. Then, at room temperature this mixture was stirred by a magnetic stirrer for 2−3 h, and then, it was filtered through glass wools to a falcon tube and its filtrate was mixed with cold t-butyl methyl ether (MTBE) (e.g., 35 mL) to induce precipitation of peptides. The peptide suspension in the falcon tube was centrifuged with 3000 rpm for 30 min at 4 °C using a centrifuge (himac CF 15R). After that, precipitated peptides were collected and again mixed with MTBE at low temperature, then the suspension was centrifuged. This cycle was continued for 2−3 times to purify the peptides partially. Then, MTBE were removed from the peptides, and then, the precipitation was solubilized by Milli-Q. This peptide solution was lyophilized using a VD-800R freeze dryer (TAITEC, Nagoya, Japan). When the lyophilization was completed, this peptide (crude PGLa) was purified by a reversed-phase HPLC (SPD-20A, Shimadzu, Japan) with a reverse phase HPLC column (COSMOSIL, 5C_{18}-AR-II, 10ID × 250 mm, Nacalai tesque, Japan). For the elution, a linear gradient from 0 to 70% (v/v) solvent B (90% acetonitrile, 10% Milli-Q and 0.1% TFA) over a period of 90 min in the mixture of solvent B and solvent A (0.1% TFA in Milli-Q) was used with a flow rate of 3 mL min^{-1}. Then, the collected fraction of PGLa solution was lyophilized. A reverse phase HPLC analytical column (COSMOSIL, 5C_{18}-AR-II, 4.6ID × 250 mm) was used to assess the purity of the purified PGLa.

The protocol for the CF labeling of the N-terminus of PGLa is as follows. At first, a mixture of 10 mL dimethylformamide (DMF) and 3.4 μL diisopropylethylamine (DIEA) (0.2 mM) was prepared. An amount of 100 mg PGLa resin was added to the 9 mL mixture of DMF and DIEA in a reaction vessel, then was shaken gently up to 30 min by a flask shaker for the swelling of the resin. Then, 9.46 mg (0.02 mmol scale) of CF in 1 mL mixture of DMF and DIEA was added into the shaker and the resulting mixture was gently

shaken for 24 h. After removing the reaction vessel from the shaker, the mixture was washed 3−4 times with DMF for the complete removal of dye. Finally, it was dried inside a vacuum desiccator overnight for complete drying. In the following steps such as the cleavage and the purification using HPLC, similar methods described for PGLa were used. The mass of the purified peptides, PGLa and CF-PGLa was measured using the liquid chromatography–mass spectrometry (LC–MS) (Parvez et al., 2018). The absorbance of CF-PGLa in buffer containing glucose was measured at 492 nm and then the concentration of CF-PGLa was calculated utilizing the molar absorption coefficient 81,000 $M^{-1}cm^{-1}$ of CF.

2.2.5. PGLa-induced AF488 membrane permeation from single DOPC/DOPG (6/4)-GUVs under Π

The interaction of PGLa with single DOPC/DOPG (6/4)-GUVs encapsulating AF488 (6.0 μM) in buffer was examined under a fluorescence microscope (IX-73, Olympus, Tokyo, Japan) using the single GUV method. A hand-made chamber for observation of GUVs was prepared using a cover slip, a slide glass, and silicon spacer with a 3 mm thickness. Just before the experiments, the glass surfaces in the chamber were coated with BSA to prevent strong interaction between GUVs and the glass surfaces. Then, a chamber containing GUVs in a hypotonic solution or an isotonic solution was placed above a 20× objective in the microscope. A thermoplate (TPi-110RX, Tokai Hit, Shizuoka, Japan) was connected to the microscope to maintain the temperature of sample solution in a chamber at 25 ± 1 °C.

To apply a PGLa solution near a GUV, a micropipette with a 20 μm diameter was used. To prepare the micropipette, first a glass capillary with a 1.0 mm diameter (G-1, Narishige) was pulled two-stepwise using a puller (PC-10, Narishige, Tokyo, Japan), and then, an extended narrow region of the capillary was cut using a cleaving tool (Supelco Inc., Bellefonte, PA). Micropipettes whose tip has a smooth edge were selected by observation using a microscope. A PGLa solution was aspirated into a micropipette using an oil-free vacuum pump.

At $t = 0$ (where t is the interaction time), a PGLa solution was started to add to the neighborhood of a target GUV from a micropipette by applying a positive pressure inside

the micropipette against its outside. The value of the positive pressure was controlled using the pressure difference transducer (DP15, Validyne, Northridge, CA) and adjusted to be 30 Pa. The distance between the target GUV and the tip of the micropipette was adjusted to 70 μm using a micromanipulator (MHW-3, Narishige). During the interaction, the PGLa solution was continuously added, and thus, the PGLa concentration in the vicinity of the GUV remained constant, which was determined using the ratio of the PGLa concentration in the solution near a GUV to that in the micropipette (i.e., 0.75) (Parvez et al., 2018).

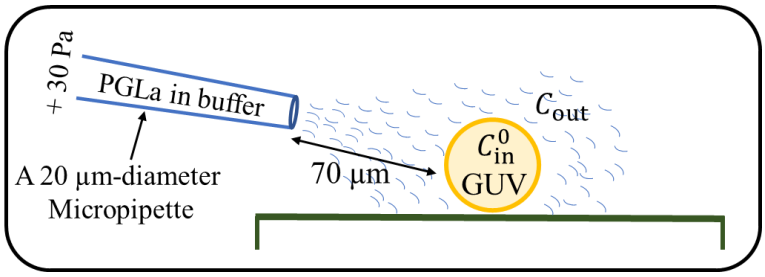

Figure 2.1: Method of applying PGLa solution to a single GUV by a micropipette. PGLa solution is applied to a single GUV from a micropipette of 20-μm-diameter at a distance of 70 μm by 30 Pa positive pressure.

The fluorescence intensity of the lumen of single GUVs due to AF488 was measured using a digital CMOS camera (ORCA-Flash 4.0 V3, Hamamatsu Photonics K.K., Hamamatsu, Japan). A neutral density (ND)-6 filter, and a ND-25 filter were used to attenuate the incident light emitting from mercury arc lamp, which decreased the photobleaching of AF488. The conditions of CMOS camera (binning: 2, sub-array: 512 × 512 pixels, exposure time: 1.0 s) were used. HCImage software (v 4.8, Hamamatsu Corporation, Bridgewater, NJ, USA) was used to analyze the fluorescence intensity of the GUV.

2.2.6. Effect of Π on the PGLa binding in a GUV membrane during their interaction

A confocal laser scanning microscope (FV1000-D, Olympus) was used to observe the interaction of a mixture of label-free PGLa and 0.2 μM CF-PGLa with single DOPC/DOPG (6/4)-GUVs. The 60× objective lens (NA 1.35; UPLSAPO060X0,

Olympus) of the microscope was cleaned by lens cleaning tissue (105, Whatman, Buckinghamshire, UK) containing lens cleaner before the observation. To suppress the refraction of light, an immersion oil (IMMOIL-F30CC, Olympus) was applied to the contact surface between the cover slip and the objective. A thermoplate (TP-110RH20, Tokai Hit) was connected to the microscope to maintain the temperature of sample solution in a chamber at 25 ± 1 °C. The confocal microscopic images of GUVs due to AF647 and CF-PGLa were obtained using the following conditions of laser and the detector system (Table 2.1). DIC mode was also used simultaneously during the interaction of GUVs with PGLa.

Table 2.1: The CLSM conditions for different measurements

Measurements	Laser (nm)	High voltage, HV (Volts)	Gain (X)	Offset (%)
AF647 fluorescence	635 (0.3%)	720	5.75	6
CF-PGLa fluorescence	473 (2.2 %)	760	5	5
DIC mode	-	200	2	5

PGLa/CF-PGLa solution (i.e., buffer with the same osmolarity as the outside solution of GUVs) was applied to a target GUV using the same method as described in the previous section. Here, the micropipette was placed at a distance of 50 μm from a GUV using the micromanipulator (Parvez et al., 2018). Time course of the fluorescence intensity of GUV lumen due to AF647 (I), the fluorescence intensity of the GUV membrane due to CF-PGLa (I_{rim}), and the fluorescence intensity of GUV lumen due to CF-PGLa (I_{lumen}) were analyzed using the Fluoview software (v 4.2). For the analysis of I, a small area (around the center) inside the GUV was selected which is about 60% of the GUV diameter, and the time course of intensity, I_{AF647}, was measured for the observation time. The background intensity (I_{back}) was also measured by selecting a small area outside of the GUV (buffer). The final value of the lumen intensity with time was calculated by subtracting the above values: $I_{AF647} - I_{back} = I$. By the same method, I_{lumen} was also calculated. On the other hand, rim intensity (I_{rim}) owing to the binding CF-PGLa to the GUV membrane was obtained as follows. First, 8 lines originated from the center

of the GUV were drawn and the sharp and highest intensity along each line was measured at a certain time (Karal et al., 2015a). This point with highest intensity corresponds to the rim of the GUV, where the I_{AF647} diminished greatly because AF647 is located only at the GUV lumen. Finally, the background intensity was subtracted, and the intensities obtained from the 8 lines were averaged to find I_{rim}. This method was used in the measurement for each time at 5–30 s intervals.

2.3. Theory

2.3.1. Connection between membrane tension and the pressure difference between the interior and exterior of the GUV

In general, the Laplace law for interfaces can be used to characterize the connection between interfacial tension (or surface tension) and the pressure difference (ΔP) between the interior and exterior of a curved body in a different medium (De Gennes et al., 2004). This Laplace law can be applied to the connection between the membrane tension (σ) in a GUV and the pressure difference (ΔP) between the interior and exterior of the GUV by substituting the membrane tension for the surface tension (Evans et al., 1976). Here, I derive this connection in a GUV using a different approach (Ahmed et al., 2024a). This new approach can be useful to estimate negative membrane tension, whereas the Laplace law cannot be applicable in describing negative membrane tension because surface tension has always positive values. In this new approach, I used the free energy (F) of the lipid bilayer to determine the connection between σ and ΔP.

Here, I consider a lipid bilayer composed of several kinds of lipids as a system. The internal energy, U, of a lipid bilayer can be described as a function of its entropy S, volume V, area A, and the number of lipid molecules N_i of lipid i. From the first law of thermodynamics,

$$dU = d'Q + d'W \qquad (2.1)$$

Here, $d'W$ is generalized work and $d'Q$ is the amount of heat absorbed by the system from the surroundings. Hence,

$$dU = TdS - PdV + \sigma dA + \sum_i \mu_i dN_i \qquad (2.2)$$

where, μ_i is the chemical potential of lipids, σ is the membrane tension. In general, the volume of lipid bilayer does not change, and thus, $dV \simeq 0$. Therefore,

$$dU = TdS + \sigma dA + \sum_i \mu_i dN_i \qquad (2.3)$$

Here, we assume that no exchange of lipids between the system (lipid bilayer) and the surroundings (i.e., closed system), and thus, $dN_i = 0$. In this case, the Helmholtz free energy (F) is expressed as follows,

$$dF = dU - TdS - SdT \;\; = \sigma dA - SdT \qquad (2.4)$$

From Eq. (2.4), the membrane tension can be expressed as follows

$$\sigma = \left(\frac{\partial F}{\partial A}\right)_T \qquad (2.5)$$

At equilibrium, the free energy has its minimum, and thus, the lipid bilayer is tension-free (i.e., $\sigma = 0$).

The subsequent equation represents the F of a bilayer composed of one kind of electrically neutral lipid, F^{neu}, which consists of a repulsive interaction and an attractive interaction between adjacent lipids (Israelachvili, 2011). Its applicability to a variety of phenomena in lipid bilayers has been established (Marsh, 1996). If N is the number of lipids in a GUV monolayer, a denotes the area per lipid in the lipid bilayer, F^{neu} is described by the following expression,

$$F^{\mathrm{neu}} = 2N\left(\gamma a + \frac{J_{\mathrm{n}}}{a^{\mathrm{n}}}\right) \qquad (2.6)$$

Here, the first term inside the bracket, γa, stands for the hydrophobic interaction where, γ denotes hydrophobic interaction energy per unit area between hydrocarbon chains and water, and the second term, J_n/a^n, represents general form of repulsive interaction between the headgroups of neighboring lipids, J_n is a quantity that characterizes the repulsion between lipids that have no electrical charge. The repulsion between neutral headgroups arises from the interchain interaction of hydrophilic segments (entropic effect) and steric-hydration forces (see section 1.3). It is considered that in most cases, $n = 1$ is suitable in Eq. (2.6) (Marsh, 1996), and here I use $n = 1$ in Eq. (2.6).

When an external force is applied to the membrane laterally, the corresponding membrane tension arises from Eqs. (2.5) and (2.6) as follows,

$$\sigma^{\mathrm{neu}} = \left(\frac{\partial F^{\mathrm{neu}}}{\partial A}\right) = 2\left(\gamma - \frac{J}{a^2}\right) \tag{2.7}$$

where $J = J_1$ in Eq. (2.6). The inclusion of electrostatic interaction due to the surface charge in the lipid bilayer is necessary for a charged lipid bilayer. Here, to calculate the tension due to the electrostatic interaction, I adopt the low electric potential assumption which is used at $|\psi| < k_B T/e$, where ψ is the electric potential near the lipid bilayer, e is elementary charge, and k_B is the Boltzmann constant. Then, the tension owing to the electrostatic interaction (σ^{el}) is described by the following equation (Eibl and Woolley, 1979; Jähnig, 1976; Marsh, 1996),

$$\sigma^{\mathrm{el}} = -\frac{X^2 e^2}{\varepsilon_w \varepsilon_0 \kappa}\frac{1}{a^2} = -2\frac{J^{\mathrm{el}}}{a^2} \tag{2.8}$$

where J^{el} is the electrostatic repulsion parameter between charged lipid molecules ($J^{\mathrm{el}} = X^2 e^2/2\varepsilon_w \varepsilon_0 \kappa$), X is the charged lipids' fraction in the membrane, ε_w and ε_0 denotes the relative permittivity of water and the permittivity of free space respectively, $1/\kappa$ is the Debye length. Thus, combining two kinds of membrane tensions expressed in Eqs. (2.7) and (2.8) gives the total membrane tension, σ, as follows,

$$\sigma = \sigma^{\mathrm{neu}} + \sigma^{\mathrm{el}} = 2\left(\gamma - \frac{Q}{a^2}\right) \tag{2.9}$$

where $Q = J + J^{\mathrm{el}}$. At mechanical equilibrium, $\partial F/\partial A = 0$ at $a = a_{\mathrm{fr}}$, which is called the optimal area. In this case, $Q = \gamma a_{\mathrm{fr}}^2$ and if $a > a_{\mathrm{fr}}$, $\sigma > 0$. Hence, the total free energy becomes,

$$F = 2N\left(\gamma a + \frac{Q}{a}\right) = 2N\gamma\left(a + \frac{a_{\mathrm{fr}}^2}{a}\right) = 2\,\gamma\left(A + \frac{A_{\mathrm{fr}}^2}{A}\right) \tag{2.10}$$

In the above equation, $A_{\mathrm{fr}} = Na_{\mathrm{fr}}$. Fig. 2.2 shows the free energy profile of a lipid bilayer (i.e., F as a function of A). This curve has positive and negative slopes in two different regions: a positive slope at $A_1 > A_{\mathrm{fr}}$ and a negative slope at $A_2 < A_{\mathrm{fr}}$, indicating that $\sigma_1 > 0$ and $\sigma_2 < 0$, respectively (Fig. 2.2 (c)). Now, I consider a GUV with radius, r, at mechanical equilibrium, and thus, its membrane area A is A_{fr}. If its radius increases by dr (> 0), the corresponding increment of the GUV membrane area, dA (> 0), is Nda (= $8\pi rdr$), and the corresponding increment of the free energy, dF, is described as follows,

$$\begin{aligned} dF &= 2N\left[\gamma(a + da) + \frac{Q}{a + da} - \gamma a - \frac{Q}{a}\right] \\ &= 2N\left(\gamma - \frac{Q}{a^2}\right)da = \sigma dA \end{aligned} \tag{2.11}$$

During the increment of the GUV radius by dr, the GUV volume V expands by dV (= $4\pi r^2 dr$, since dr is small), and thus, the total work (δW) due to the pressure inside (P_{in}) and outside (P_{out}) of the GUV and due to the change in the GUV area, dA, can be expressed by the following equation (De Gennes et al., 2004),

$$\delta W = dF - (P_{\mathrm{in}} - P_{\mathrm{out}})dV \tag{2.12}$$

In case of mechanical equilibrium, the total work done is zero. Therefore, the following equation is derived from Eqs. (2.11) and (2.12),

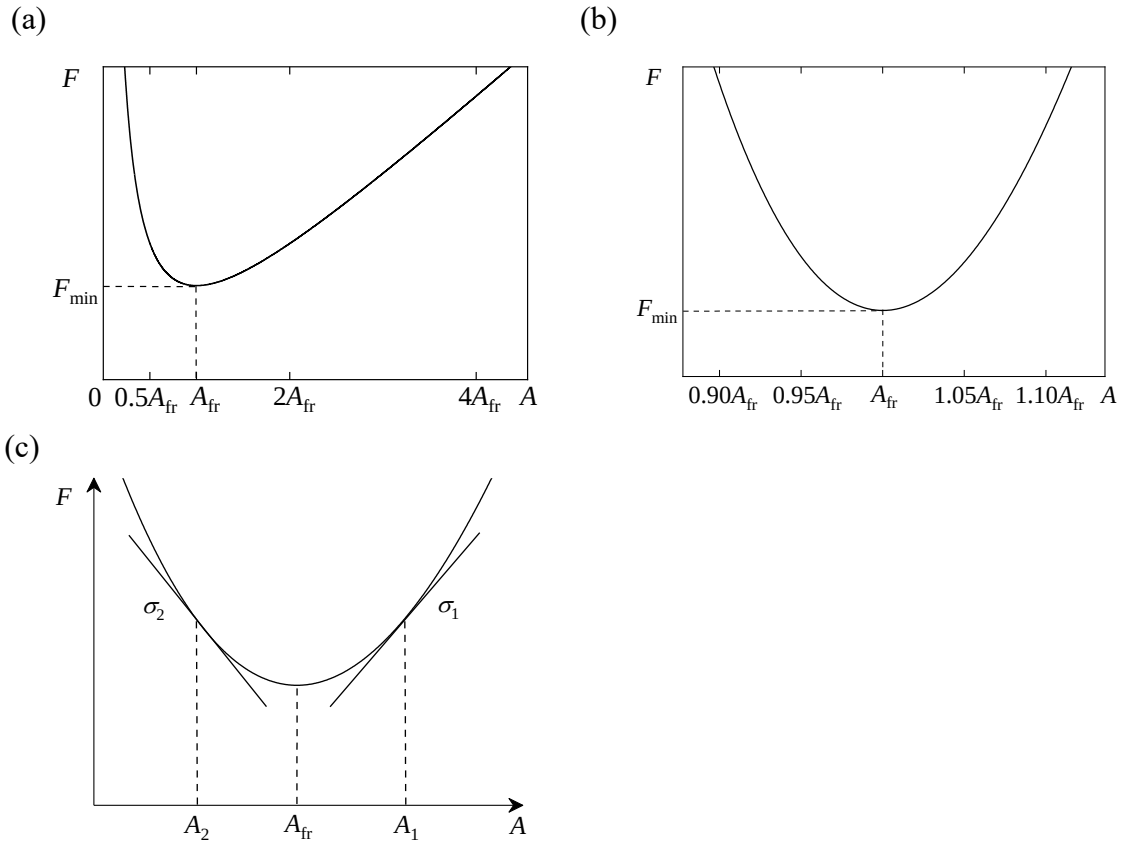

Figure 2.2: Free energy of a lipid bilayer and membrane tension. (a) The free energy, F, determined by Eq. (2.10) vs. the area of lipid bilayer, A (= Na). The y-axis has an arbitrary unit. F_{min} is the minimum of F at the optimal area, A_{fr} (= Na_{fr}). (b) An expanded figure of the region around A_{fr} in the panel a. (c) A scheme representing the connection between F and σ. A positive slope of the curve at A_1 (> A_{fr}) indicates positive membrane tension, σ_1. In contrast, a negative slope of the curve at A_2 (< A_{fr}) indicates negative membrane tension, σ_2.

$$\Delta P = P_{\text{in}} - P_{\text{out}} = \frac{2\sigma}{r} \qquad (2.13)$$

Under this condition, $\sigma > 0$ (i.e., σ_1), and thus, $P_{in} > P_{out}$. Eq. (2.13) is analogous to the Laplace law when the membrane tension term (σ) in Eq. (2.13) is substituted with the surface tension between water and air (De Gennes et al., 2004).

If a spherical GUV membrane is compressed due to an external stress, the area per

lipid molecule is smaller than the optimal area (i.e., $a < a_{fr}$), and thus, Eq. (2.9) indicates $\sigma < 0$ because $Q = \gamma a_{fr}^2$. A negative slope is found at $A < A_{fr}$ (Fig. 2.2), which also indicates $\sigma < 0$ (i.e., σ_2). Since r is increased by dr (> 0), Eqs. (2.11) and (2.12) are valid, therefore indicating that Eq. (2.13) is likewise valid. In light of this circumstance, $\sigma < 0$, and thus, $P_{in} < P_{out}$. Consequently, for GUVs with a negative σ, Eq. (2.13) provides the pressure difference between the interior and exterior of the GUV.

2.3.2. Membrane tension in a GUV induced by osmotic pressure (Π)

As described in the section 2.1, when a GUV is placed in a hypotonic solution, it creates a positive osmotic pressure that acts against the GUV. The increase in volume of the GUV leads to stretching its membrane, causing a positive membrane tension in the GUV. In contrast, when a GUV is placed in a hypertonic solution, it creates a negative osmotic pressure that acts against the GUV. The decrease in volume of the GUV leads to compressing its membrane, causing a negative membrane tension in the GUV.

Using the theory for positive osmotic pressure developed previously (Shibly et al., 2016; Saha et al., 2020), the equation of the membrane tension of a GUV under both osmotic pressure (Π), positive Π and negative Π, can be obtained as follows. When a GUV (with initial radius r_0, membrane area A_0, and volume V_0) containing buffer with initial osmolarity (C_{in}^0) is transferred into a hypotonic or a hypertonic solution where the osmolarity is C_{out}, the difference in the osmolarity, ΔC^0 (= $C_{in}^0 - C_{out}$) induces Π against the GUV. If the osmolarity is low, Π is proportional to ΔC^0 (i.e., $\Pi = RT\Delta C^0$). If the solution outside the GUV is hypotonic, $\Pi > 0$, whereas if the solution is hypertonic, $\Pi < 0$. This ΔC^0 induces a change in the radius of the GUV until its expansion or shrinkage equilibrium is attained. The GUV at this equilibrium has a radius of ($r_0 + \Delta r$), a membrane area of ($A_0 + \Delta A$), and a volume of ($V_0 + \Delta V$). Using Eq. (2.13), the pressure difference between the interior and exterior of the GUV at equilibrium, ΔP_{eq}, can be described using the membrane tension induced by Π, σ_{osm}, as follows:

$$\Delta P_{eq} = P_{in} - P_{out} = \frac{2\sigma_{osm}}{r_0 + \Delta r} \tag{2.14}$$

Due to the volume change in the GUV, C_{in}^0 changes to C_{in}^{eq}, resulting in change in the

difference in the osmolarity at equilibrium (ΔC^{eq}) (i.e., $\Delta C^{eq} = C_{in}^{eq} - C_{out}$). Thus, $\Delta P_{eq} = RT\Delta C^{eq}$. Therefore,

$$\sigma_{osm} = \frac{RT(r_0 + \Delta r)}{2}\Delta C^{eq}$$
$$\approx \frac{RT(r_0 + \Delta r)}{2}\left[\frac{C_{in}^0}{1 + 3(\Delta r/r_0)} - C_{out}\right] \quad (2.15)$$

where $C_{in}^{eq} = C_{in}^0 V_0 / (V_0 + \Delta V)$ we used an approximation for $\Delta V/V_0 \approx 3(\Delta r/r_0)$ because the GUV is spherical and $\Delta r_{eq}/r_0 << 1$ (Shibly et al., 2016). As described in Chap.1, membrane tension, σ_{osm}, is proportional to the fractional area change, $\delta (= \Delta A/A_0)$, if δ is small.

$$\sigma_{osm} = K_{bil}\delta \approx 2K_{bil}\frac{\Delta r}{r_0} \quad (2.16)$$

where $\Delta A/A_0 \approx 2(\Delta r/r_0)$ is used.
By combining Eqs. (2.15) and (2.16), a following equation is obtained (Shibly et al., 2016).

$$\frac{\Delta r}{r_0} = \frac{RT\Delta C^0/2}{\frac{2K_{bil}}{r_0} + \frac{3RTC_{out}}{2} - \frac{RT\Delta C^0}{2}} \quad (2.17)$$

When C_{out} is large, e.g., ~300 mOsm L^{-1}, which is the osmolarity of buffer containing 150 mM NaCl, Eq. (2.17) can be approximated as (Saha et al., 2020),

$$\frac{\Delta r}{r_0} = \frac{\Delta C^0}{3C_{out}} \quad (2.18)$$

By combining Eqs. (2.17) and (2.18), a following equation is obtained.

$$\sigma_{\mathrm{osm}} = \frac{2K_{\mathrm{bil}}\Delta C^0}{3C_{\mathrm{out}}} \tag{2.19}$$

If $\Delta C^0 > 0$, $\sigma_{\mathrm{osm}} > 0$, indicates a positive membrane tension, whereas if $\Delta C^0 < 0$, $\sigma_{\mathrm{osm}} < 0$, demonstrates a negative membrane tension in the GUV.

2.4. Results

2.4.1. Effect of osmotic pressure on PGLa-induced nanopore formation

To examine the impact of osmotic pressure on PGLa-induced nanopore formation, firstly I studied the release of AF488 from single DOPG/DOPC (4/6)-GUVs under Π due to their interaction with PGLa using the single GUV method. For this purpose, GUVs encapsulating sucrose and AF488 in buffer (the osmolarity of GUV lumen, C_{in}^0, 388 mOsm L^{-1}) was mixed with buffer containing 81.0 mM glucose to produce a final osmolarity of the outside of the GUV, C_{out}, of 376 mOsm L^{-1}. The difference in the osmolarities between the inside and the outside of GUVs, ΔC^0 (= $C_{\mathrm{in}}^0 - C_{\mathrm{out}}$), was 12 mOsm L^{-1}, which induces osmotic pressure against GUVs ($\Pi = RT\Delta C^0$), resulting in a membrane tension of 2.6 mN m^{-1} in the GUVs according to Eq. (2.19). After the swelling equilibrium of GUVs, I examined the interaction of 4.0 μM PGLa with a single GUV using fluorescence microscopy (FLM). At $t = 0$, the GUV showed strong phase contrast because the inner solution (containing sucrose) of the GUV possesses a different refractive index compared to its surroundings (containing glucose) (Fig. 2.3 (a) (1)) and a high fluorescence intensity (I) of the GUV lumen due to AF488 (Fig. 2.3 (a) (2)). To analyze the membrane permeation of AF488 more quantitatively, the normalized fluorescence intensity of the GUV lumen due to AF488 (i.e., $I_{\mathrm{N}}(t) = I(t)/I(0)$, where $I(t)$ and $I(0)$ are the fluorescence intensity of the GUV lumen at time t and $t = 0$, respectively) was plotted as a function of time (Fig. 2.3 (b)). Initially, there was no noticeable change in $I_{\mathrm{N}}(t)$, however, $I_{\mathrm{N}}(t)$ began to drop at 135 s and reached zero at 360 s (Fig. 2.3 (b), 2.3 (a) (2)), indicating that AF488 concentration in the GUV lumen, C_{AF}, began to decrease at 135 s since the fluorescence intensity I is proportional to C_{AF}. Fig. 2.3 (a) (3) depicts a phase-contrast image of the same GUV captured at 370 s, showing a significant reduction in phase contrast, whereas the form and size of the GUV remained unchanged. Based on

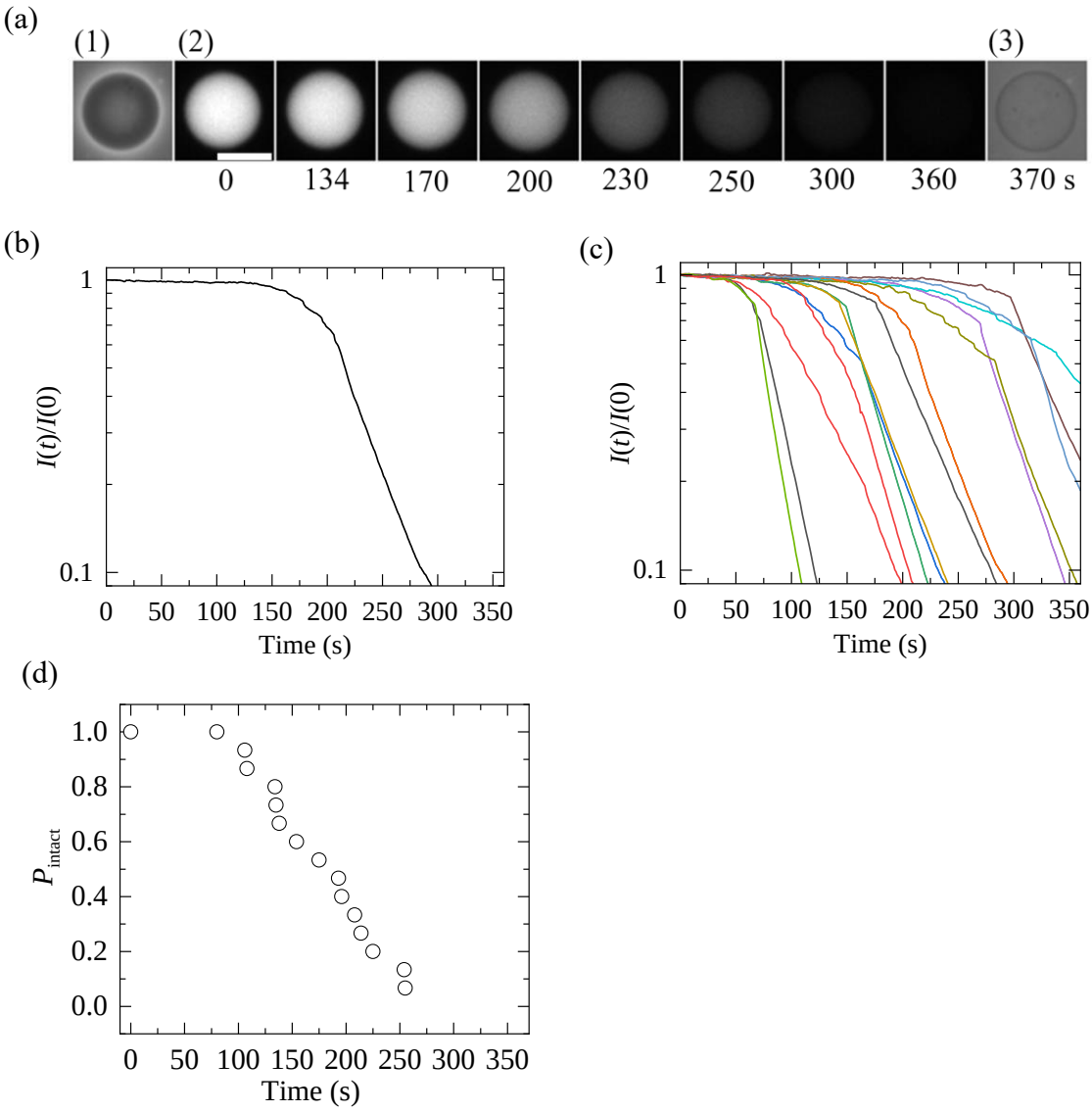

Figure 2.3: AF488 membrane permeation from single DOPC/DOPG (6/4)-GUVs under osmotic pressure (ΔC^0 = 12 mOsm L^{-1}) induced by 4.0 µM PGLa. (a) Microscopic images of a GUV due to phase contrast (1 and 3) and due to AF488 fluorescence (2) during its interaction with PGLa are shown. The interaction time is described below each image. Bar, 20 µm. (b) Change in normalized fluorescence intensity, $I_N(t)$, of the GUV lumen over time. It corresponds to the data shown in panel a. (c) Change in $I_N(t)$ of several different GUVs over time under the same condition. (d) The time course of the fraction of intact GUVs among all GUVs, P_{intact}.

these results, it is reasonably inferred that PGLa induces nanopores in the GUV membrane, and then, membrane permeation of AF488 and sucrose occurs through these nanopores from the GUV inside to the GUV outside. The starting time of the decrease in I_N (135 s) is that of membrane permeation of AF488, and thus, that of nanopore formation. The same experiments were repeated using 14 single GUVs (m = 14). The results revealed that the starting time of AF488 membrane permeation differed in each GUV (Fig. 2.3 (c)). This result indicates that the nanopore formation occurs in each GUV at different time, suggesting the stochastic pore formation induced by PGLa. Burst of GUVs did not occur in all GUVs.

The time course of $I_N(t)$ after the starting time of membrane permeation can provide the information of the membrane permeation of AF488 through the PGLa-induced nanopores. The rate constant of AF488 membrane permeation in a GUV ($k_{leak}(t)$) is defined as follows,

$$\frac{C_{AF}(t)}{C_{AF}(0)} = \frac{I(t)}{I(0)} = I_N(t) = \exp(-k_{leak}(t)t) \qquad (2.20)$$

where $C_{AF}(t)$ and $C_{AF}(0)$ are AF488 concentrations in the GUV lumen at time t and time t = 0, respectively. The disadvantage of the value of $k_{leak}(t)$ is that it depends on the diameter of GUVs. In contrast, the membrane permeability coefficient per unit area of the membrane, $P(t)$, does not depend on the GUV diameter, and it is defined using the flux of AF488 through the membrane, φ, as follows,

$$\varphi = -P(t)[C_{AF}(t) - C_{AF}^{out}(t)] \qquad (2.21)$$

Here, $C_{AF}^{out}(t)$ is the concentration of AF488 outside the GUV, which can be approximated as 0 under this experimental condition. $P(t)$ can be determined by $k_{leak}(t)$ using $P(t) = rk_{leak}(t)/3$, where r is the GUV radius (Alam et al., 2012). Figure 2.3 (b) shows that after the starting time of membrane permeation $P(t)$ of AF488 gradually increased over time until it reached its steady value, P^s, which persisted for a prolonged period. The values of P^s can be obtained by the radius of the GUV and the slope of the steady region of the curves in Fig. 2.3 (b)(c). For a GUV shown in Fig. 2.3 (b), the steady membrane

permeation started at t = 206 s with $k_{leak}{}^{s} = 5.6 \times 10^{-2}$ s^{-1}. Since the radius of the GUV is 15 μm, the value of $P^{s} = 2.8 \times 10^{-1}$ μm s^{-1}. The analysis of the results of 32 GUVs (m = 32) provided that the mean value ± the standard error (SE) of P^{s} under this condition (ΔC^{0} = 12 mOsm L^{-1}) is (2.3 ± 0.2) × 10^{-1} μm s^{-1}. To examine the effect of osmotic pressure on P^{s}, the interaction of 4.0 μM PGLa with single GUVs under isotonic conditions was examined. The analysis of the result provided that $P^{s} = (1.1 \pm 0.2) \times 10^{-1}$ μm s^{-1} (m = 16). These results indicate that osmotic pressure enhances the P^{s} value significantly. Under isotonic condition, the value of P^{s} of AF488 is higher than that of another fluorescent probe, calcein under the same conditions of PGLa-induced nanopore formation (Parvez et al., 2018). This difference can be attributed to the size of fluorescent probes (i.e., the Stokes-Einstein radius (R_{SE}) of calcein is 0.73 nm (Tamba et al., 2010) and R_{SE} of AF488 is 0.58 nm (Heyman and Burt, 2008)).

As described above, Fig. 2.3 (c) shows that the starting time of nanopore formation differs for each GUV. Based on this characteristic, the rate of PGLa-induced nanopore formation in the lipid bilayer can be estimated using the fraction of intact GUVs among all examined GUVs, $P_{intact}(t)$. If the pore formation occurs by a transition from the intact state of a GUV to its pored state, the rate constant for pore formation, k_p, can be obtained (Tamba and Yamazaki, 2005). However, it was reported that for PGLa-induced pore formation in DOPC/DOPG-GUVs, PGLa molecules transfer from the outer to inner monolayer without pore formation and under the symmetric binding of the peptides the pore formation occurs (Parvez et al., 2018). Therefore, this type of pore formation cannot be regarded as the two-state transition. In this situation, the rate of pore formation is estimated by another parameter, $P_{leak}(t)$ (= 1 − $P_{intact}(t)$), i.e., the fraction of leaking GUVs where leakage had begun or was complete at interaction time (t) (Tamba and Yamazaki, 2005). I performed 4 independent experiments (M = 4) under the same conditions (ΔC^{0} = 12 mOsm L^{-1}), and obtained that mean values and SEs of P_{leak}(200 s) and P_{leak}(300 s) are 0.70 ± 0.06 and 0.95 ± 0.03, respectively. To examine the effect of osmotic pressure on $P_{leak}(t)$, the interaction of 4.0 μM PGLa with single GUVs under isotonic conditions was investigated, providing P_{leak}(200 s) = 0.22 ± 0.05 and P_{leak}(300 s) = 0.53 ± 0.03 (M = 3). These results indicate that osmotic pressure enhances the $P_{leak}(t)$ value significantly, i.e., the membrane tension elevates the rate of PGLa-induced nanopore formation.

I also examined the effect of higher Π (ΔC^0 = 17 mOsm L^{-1}) on PGLa-induced nanopore formation. Membrane tension due to this osmotic pressure is 3.4 mN m^{-1}. Figure 2.4(a) shows that $P_{intact}(t)$ in a typical experiment (m = 16) decreased rapidly with time to reach 0 (i.e., pore formation occurred in all GUVs) at 190 s. Burst of GUVs did not occur in all GUVs. Figure 2.4(b) shows the effect of osmotic pressure on $P_{leak}(t)$, indicating that P_{leak}(200 s) and P_{leak}(300 s) increased with increasing Π. This indicates that σ (due to Π) is responsible for the increased rate of pore formation in lipid bilayer induced by PGLa.

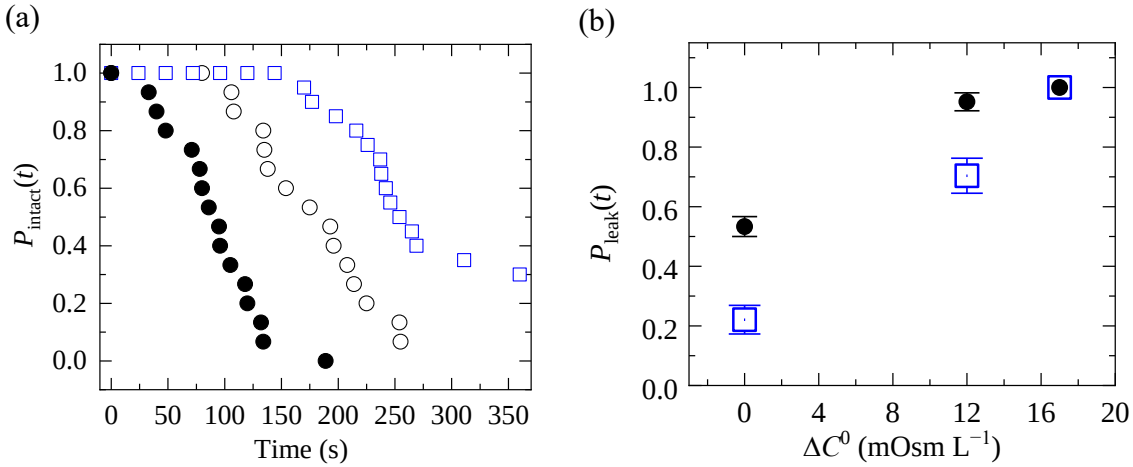

Figure 2.4: Effect of Π on rate of PGLa-induced nanopore formation in GUVs 4.0 μM PGLa. (a) Change of P_{intact} over time. (●) ΔC^0 = 17, (○) 12, and (blue □) 0 mOsm L^{-1}. (b) The effect of osmotic pressure on P_{leak}(200 s) (blue □) and P_{leak}(300 s) (●). Mean values and SEs (M = 3) are shown.

2.4.2. Effect of osmotic pressure on the location of PGLa in a GUV membrane during their interaction

To examine the location of PGLa in a GUV during their interaction, its fluorescent analogue, CF-PGLa was used here. It is noted that if there is no fluorescence quenching, the fluorescence intensity of GUV membrane due to CF-PGLa observed using CLSM, i.e., rim intensity (I_{rim}), is proportional to the peptide concentration in the GUV membrane (Islam et al., 2017). Since high concentration of fluorescent dye-labeled peptides in a

GUV membrane induces the self-quenching of its fluorescence (Islam et al., 2017), a mixture of label-free PGLa and 0.2 μM CF-PGLa was used here.

At first, I examined the effect of Π (ΔC^0 =17 mOsm L^{-1}) on the transfer of PGLa across the GUV bilayer. For this purpose, the interaction of a mixture of 4 μM PGLa and 0.2 μM CF-PGLa (19:1 ratio) with single DOPC/DOPG (6/4)-GUVs were examined using CLSM. Confocal images of the GUV during the interaction are shown in Fig. 2.5 (a), where panel (1) corresponds to the fluorescence image of the GUV lumen due to AF647 and panel (2) is the fluorescence image of the GUV due to CF-PGLa. By analyzing the fluorescence intensity of these images quantitatively, the time course of the fluorescence intensity of three places were obtained (Fig. 2.5 (b)). The blue line indicates the fluorescence intensity of GUV lumen due to AF647, I, as its normalized intensity (i.e., $I_N(t)$). $I_N(t)$ remained constant until 178 s, indicating that the GUV was intact. Then, it decreased slowly, indicating that the rate of AF647 membrane permeation was small. Thus, the starting time of decrease in $I_N(t)$ (178 s) is the onset time of AF647 membrane permeation, indicating that pore formation was started at 178 s.

Red triangles (▲) in Fig. 2.5 (b) denote the rim intensity due to CF-PGLa (I_{rim}). After initiating the interaction between PGLa/CF-PGLa with the GUVs, I_{rim} increased gradually with time and at 42 s it reached a stable value, which remained constant for ~40 s. This state can be called the first stable state, which has a stable rim intensity, $I_{rim}(1^{st})$. At 81 s I_{rim} increased abruptly, and it reached another stable value at t = 113 s, which did not change for a long period and even after the AF647 membrane permeation, i.e., pore formation. This state can be called the second stable state with a rim intensity of $I_{rim}(2^{nd})$. The ratio of these stable rim intensity, $I_{rim}(2^{nd})/I_{rim}(1^{st})$, was 1.9. Black line in Fig. 2.5 (b) represent the fluorescence intensity of GUV lumen due to CF-PGLa (I_{lumen}), which had a quick rise starting at 87 s, a little after the starting time of increase in I_{rim} from the first stable state. I_{lumen} reached its maximum at 116 s and remained steady even after pore formation.

Similar results of the time courses of three kinds of fluorescence intensities were found in 45 GUVs (m = 45) from M = 3, whereas the starting time of increase in I_{rim} from the first stable state as well as that of pore formation differed in each GUV.

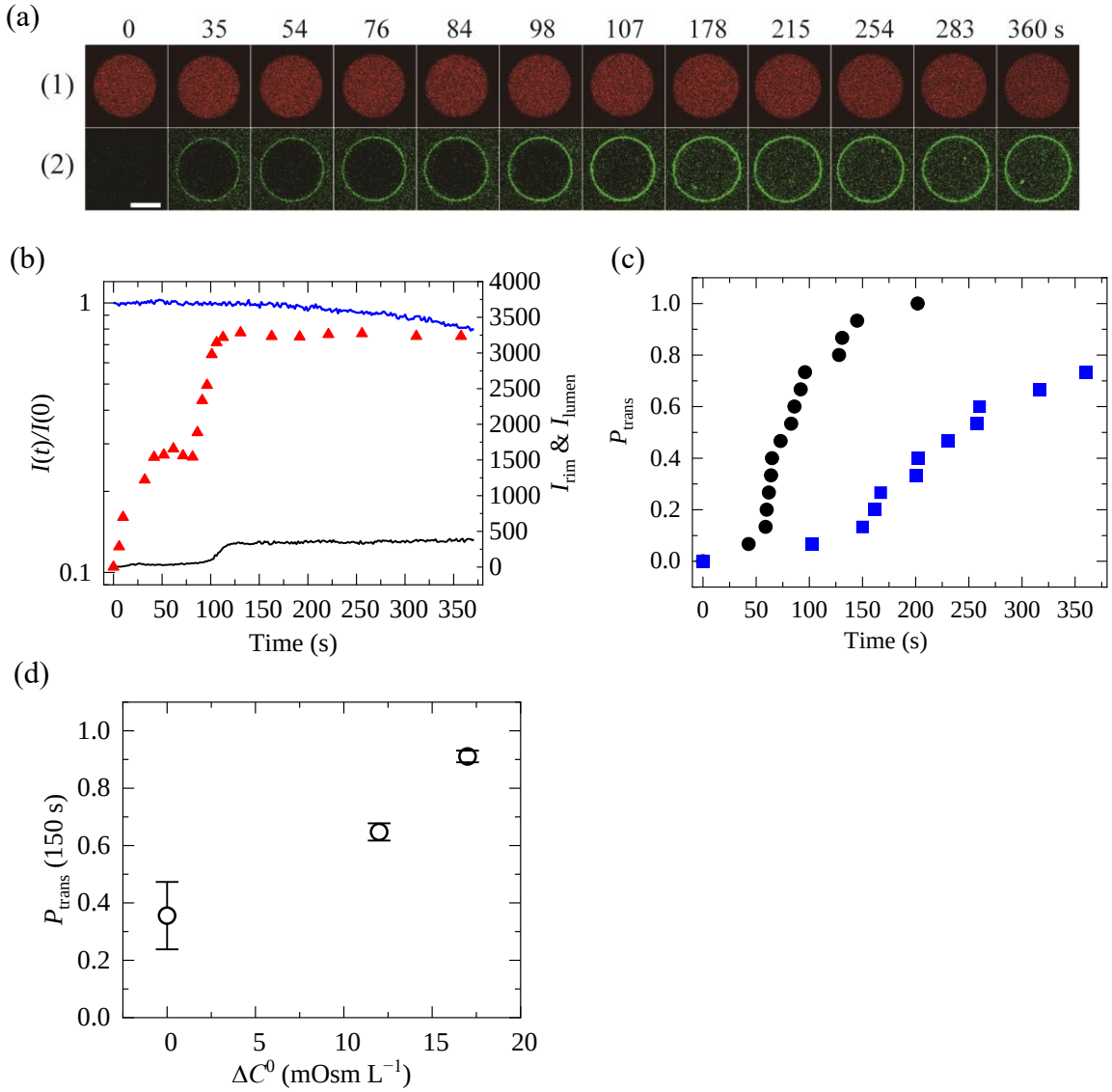

Figure 2.5: Effect of osmotic pressure on the transfer of PGLa across the GUV bilayer. Interaction of 4.0 µM PGLa/CF-PGLa with single DOPC/DOPG (6/4)-GUVs. (a) Confocal microscopic images of a GUV under Π (ΔC^0 = 17 mOsm L^{-1}) due to AF647 (panel 1) and CF-PGLa (panel 2). Bar, 10 µm. The interaction time is described above each image. (b) Change of three kinds of fluorescence intensities of the GUV over time. These intensities were obtained by analyzing the GUV images shown in panel a. Left axis: blue line indicates $I_N(t)$ of the GUV lumen due to AF647. Right axis: red ▲denotes the I_{rim} and black line denotes I_{lumen} due to CF-PGLa. (c) Change of the fraction of GUVs where PGLa transfer across the GUV bilayer occurs, P_{trans}, as a function of t. (●) ΔC^0 = 17, (blue ■) 0 mOsm L^{-1} (i.e., isotonic). (d) Relationship between Π and P_{trans} at t = 150 s. Mean values and SEs (M = 3) of P_{trans}(150 s) are shown.

These results can be interpreted reasonably as follows. After the interaction of PGLa with a GUV starts, PGLa molecules rapidly bind to the GUV outer monolayer from the solution outside the GUV until the PGLa concentration in the outer monolayer reaches an equilibrium, resulting in the first stable state. After a specific time, PGLa molecules starts to transfer across the GUV bilayer from the outer to the inner monolayers. The PGLa concentration in the solution outside the GUV remains constant during the interaction owing to the continuous application of PGLa solution from the micropipette. After PGLa transfers into the inner monolayer, its concentration in the outer monolayer decreases, resulting in the rapid binding of PGLa to the GUV outer monolayer from the solution to recover its equilibrium binding. Thus, the PGLa concentration in the outer monolayer did not change during the transfer. Therefore, the result of $I_{rim}(2^{nd})/I_{rim}(1^{st}) = \sim 2$ indicates that the PGLa concentrations in both monolayers are the same, which is called the symmetric binding of peptides in the lipid bilayer (briefly, symmetric binding) (Levadnyy et al., 2019). Based on this scenario, the starting time for the increase of I_{rim} from $I_{rim}(1^{st})$ to $I_{rim}(2^{nd})$ (i.e., 81 s) indicates the starting time of the transfer of PGLa across the GUV bilayer. The time when I_{rim} reached a second stable value, $I_{rim}(2^{nd})$ (i.e., 113 s) indicates the time when the symmetric binding of CF-PGLa reaches.

Next, I performed the same experiments under the isotonic condition, i.e., the interaction of a mixture of 4 μM PGLa/CF-PGLa (containing 0.2 μM CF-PGLa) with single DOPC/DOPG (6/4)-GUVs. I found that the similar time course of three fluorescence intensities, indicating that osmotic pressure does not affect the PGLa binding across the GUV bilayer during the interaction, but the values of the starting time of the transfer of PGLa across the GUV bilayer under isotonic condition were larger than those under the osmotic pressure. The analysis of this starting time can be used for the estimation of the rate of PGLa transfer through the GUV bilayer and the comparison of the rate under different osmotic pressure. Since the increase of I_{rim} from $I_{rim}(1^{st})$ occurred stochastically, it is necessary to introduce the concept of probability, which has been used for estimating the rate of PGLa-induced pore formation. For this purpose, I used here a parameter, $P_{trans}(t)$, which is the fraction of GUVs where PGLa transfer across the GUV bilayer to the inner monolayer started or completed at interaction time (t) among all examined GUVs. For the GUVs under osmotic pressure due to $\Delta C^0 = 17$ mOsm L^{-1}, at

the beginning of the interaction $P_{trans}(t) = 0$, and it started to increase at 50 s, and then reached 1 at 200 s, whereas under isotonic condition at 100 s, it started to increase and but reached 0.75 at 360 s (Fig. 2.5 (c)). To evaluate the rate of increase in P_{trans}, its value at a specific interaction time, e.g., P_{trans}(150 s), was used here. P_{trans}(150 s) increased with increasing osmotic pressure. This analysis provides that the rate of transfer of PGLa across the GUV bilayer increases as osmotic pressure increases.

2.5. General discussion

The results obtained from the experiments regarding the effect of Π on the AF488 membrane permeation indicate that membrane tension due to Π enhances the rate of PGLa-induced nanopore formation in DOPC/DOPG (6/4)-GUVs without inducing a micropore and GUV burst. The increase of the rate of nanopore formation with membrane tension is the same as that for the case of Mag, whereas the evolution of PGLa-induced nanopore under the membrane tension is different from that for the case of Mag, where a nanopore is converted to a micropore, whose dimeter increases with time, and finally the GUV is transformed into a compact lipid aggregate (see Chap. 1) (Billah et al., 2022). I consider the mechanism underlying this difference. The results of PGLa-induced AF488 membrane permeation (shown in Fig. 2.3) indicate that the membrane permeability coefficient, $P(t)$, of AF488 progressively rises over time until it reaches a maximum and constant value. This characteristics of the time course of $P(t)$ is similar to that in the lysenin-induced pores (Alam et al., 2012). It is well known that lysenin forms a specific oligomer with a specific pore size in the membrane, and thus, the increase in $P(t)$ is due to the increase in the number of the pores. Two types of structures are well-known for nanopores composed of α-helix. One is barrel-stave pores or helix-bundle pores (Fig. 2.6 (a)), where the peptides insert vertically and then a fixed number of peptides associate strongly to each other to form an α-helical bundle (Montal, 1995). Inside the bundle, a water channel is formed. Since the barrel-stave pore is composed of an oligomer of α-helices, its pore has a specific size. Thus, one can reasonably infer that the time course of $P(t)$ in barrel-stave pores comprising several α-helices is similar to that in lysenin pore. These results suggest that a PGLa-induced nanopore may be a barrel-stave type based on the characteristics of the time course of $P(t)$. The other structure of nanopore is toroidal

pores (Fig. 2.6 (b)), where two monolayers bend and combined with each other at the pore and peptides are inserted in the combined monolayer at the pore, and thus, the pore wall is composed of hydrophilic surface of peptides and membrane interface of the monolayer composed of the hydrophilic segment and hydrophobic segments of lipids. It is considered that there is no specific and strong interaction between the peptides in a toroidal pore. One can infer that the size of a toroidal pore can be changed easily due to this characteristic. In case of Mag-induced nanopore formation in DOPC/DOPG (6/4)-GUVs, initially Mag forms larger pores in the bilayer and the sizes of the pores decrease over time into smaller ones (Tamba et al., 2010), supporting the above inference. This inference can explain the effect of membrane tension on Mag-induced nanopore formation. Membrane tension increases the diameter of a Mag-induced nanopore to a micropore, and then, increases the diameter of the micropore further until membrane tension becomes 0. Then, due to the attractive interaction between the Mag-bound lipid membranes due to electrostatic interaction, the membrane folding occurs at the edge of the micropore, eventually this process produces a compact membrane aggregate (Billah et al., 2024, 2022). In contrast, under membrane tension, PGLa does not induce GUV burst nor formation of a micropore. This result suggests that PGLa-induced nanopore does not have a toroidal pore structure.

The analysis of $P(t)$ at the steady state (i.e., P^s) indicates that osmotic pressure enhances the value of P^s. For this mechanism, a few factors can be considered. (A) Membrane tension may increase the number of pores: If membrane tension increases the binding constant of PGLa to the membrane, it may be possible because the number of pores depends on the PGLa concentration in the membrane. $P(t)$ value for ΔC^0 =12 mOsm L^{-1} is almost two-fold that for the isotonic condition. However, it may be difficult to consider the two-fold increase in the number of pores. (B) Membrane tension increases the size of a pore: Membrane tension may increase the number of peptides in a pore, which increase the size of pore. It may be also difficult to consider the two-fold increase in the size of pore. (C) Water efflux increases the membrane permeability of AF488: The higher hydrostatic pressure in the GUV lumen due to Π produces a large water efflux. It is reported that in the Π-induced pore formation in a GUV without AMPs, a large water

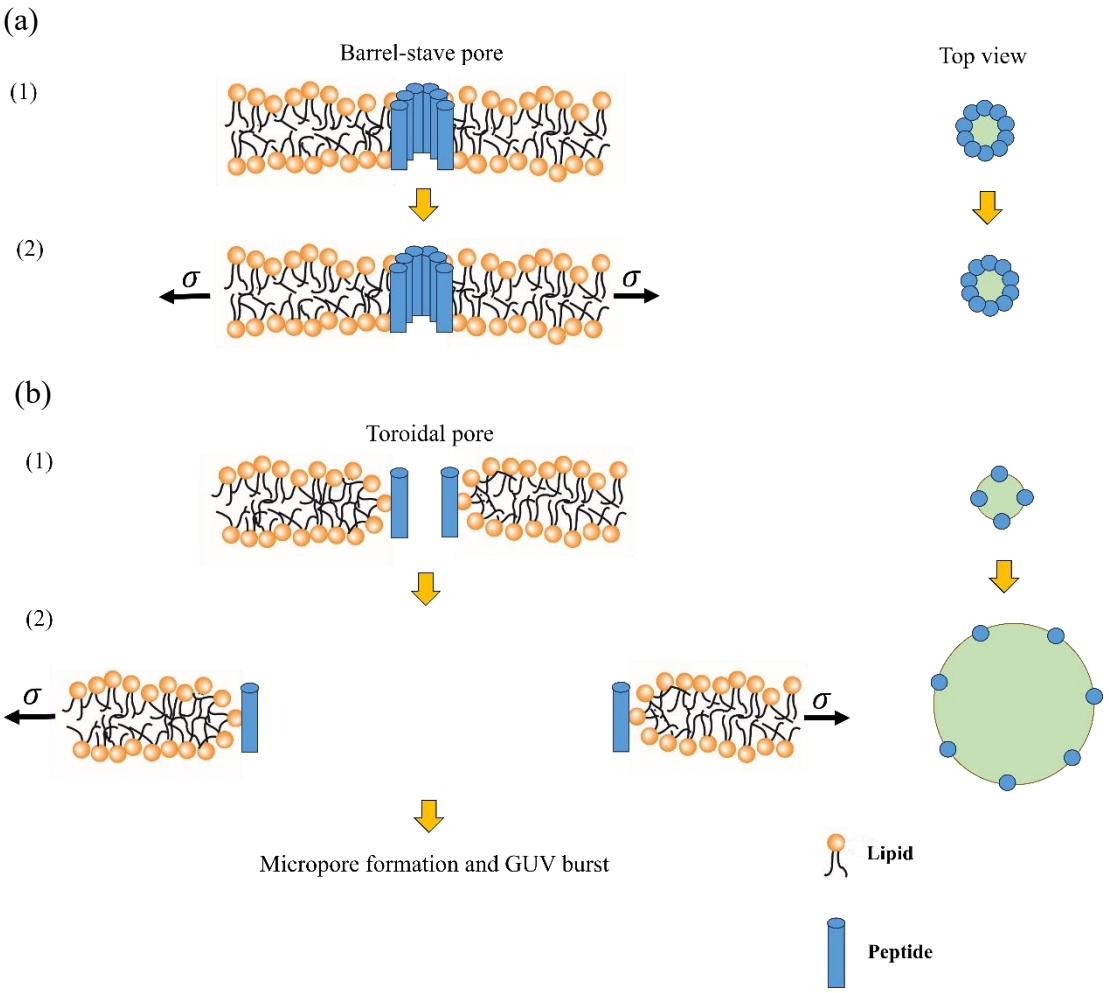

Figure 2.6: A scheme of two models of nanopore composed of α-helices and the effect of membrane tension on their structures. (a) Barrel-stave pore (or helix-bundle pore) where the peptides insert vertically and then a fixed number of peptides associate strongly to each other to form an α-helical bundle. Size of a barrel-stave pore does not change significantly. (b) Toroidal pore where two monolayers bend and combined with each other at the pore and peptides are inserted in the combined monolayer at the pore. Membrane tension increases the size of the toroidal nanopore, resulting in a micropore, and finally GUV burst occurs.

efflux concomitantly with efflux of sucrose was observed transiently (for ~100 ms) (Shibly et al., 2016). In this case, a large pore is closed rapidly because σ rapidly becomes small due to the large water efflux. However, in the PGLa-induced pore, the rate of water efflux is small (i.e., σ does not decrease significantly), and thus, the enhanced water efflux continues for at least 100 s. It is reasonably considered that the membrane permeation, or the flux of AF488 is coupled with water efflux, and thus, $P(t)$ of AF488 is enhanced. Currently, it is difficult to conclude which factor plays a key role in the Π-enhanced membrane permeability of AF488 due to the limited experimental results.

The results of the location of PGLa in a GUV indicate that the rate of transfer of PGLa across the GUV bilayer without pore formation is enhanced with increasing osmotic pressure. This transfer of PGLa may occur through a pre-pore in the lipid bilayer. As described in chapter one, a pre-pore is a nanoscale region of low density of lipids in a lipid bilayer in the L_α phase. The pre-pore wall is considered to possess a toroidal-like configuration where the outer and the inner monolayers are connected (Evans et al., 2003; Karal et al., 2016). As a result, the edge of a pre-pore has an extra free energy, called line tension, Γ, and thus, the lifetime of a pre-pore is extremely small. If it can be approximated that a pre-pore is a cylinder and a lipid bilayer is a significantly large thin sheet compared to the pre-pore radius (r_p), the free energy [$\Omega(r_p)$] associated with a pre-pore can be expressed as (Karal et al., 2016; Levadny et al., 2013),

$$\Omega(r_p) = 2\pi r_p \Gamma - \pi(\sigma + B) r_p^2 + \Omega_0 \qquad (2.22)$$

where Ω_0 is a free energy independent of σ, and B is the parameter of electrostatic interaction described as follows,

$$B \approx \frac{4\rho k_B T}{e}\left[\frac{1-q}{p} + \ln(p+q)\right] - \frac{\rho^2 \omega^2 h}{2\varepsilon_w \varepsilon_0} \qquad (2.23)$$

where ρ is the surface charge density of the bilayer, $p = 2\pi\lambda_B X/\kappa A$ (here, λ_B is Bjerrum length in water (= 0.716 nm at 25 °C), A is total membrane area), $q = (1 + p^2)^{1/2}$, ω denotes a factor that determines the ratio of the surface charge density of the pre-pore wall to that of the total bilayer (i.e., the surface charge density of the pre-pore wall is $\omega\rho$ ($0 \le \omega \le 1$)),

h is the bilayer thickness. In Eq. (2.22), the first term represents the free energy increase induced by creation of the pre-pore edge, which is proportional to the pre-pore perimeter (= $2\pi r_p$). The second term has two components; one ($-\pi\sigma r_p^2$) is the reduction in elastic energy due to a decrease in area of a stretched membrane, and the other ($-B\pi r_p^2$) indicates the decrease in the electrostatic free energy of the charged lipid bilayer due to the presence of a pre-pore. The last term of Eq. (2.22), Ω_0 can be regarded as the free energy of a pre-pore required for its nucleation based on the MD simulation result (Tolpekina et al., 2004; Wohlert et al., 2006). The values of Ω_0 were determined experimentally for the first time by the measurement of temperature dependence of the rate constant of constant-tension-induced GUV burst (see the details in section 3.3), because these experiments provide the activation energy of the tension-induced nanopore formation as a function of tension (Karal et al., 2016; Karal and Yamazaki, 2015). However, in most cases, the values of Ω_0 are not known. Therefore, the following equation has to be used as an approximation,

$$\Omega(r_p) = 2\pi r_p \Gamma - \pi(\sigma + B) r_p^2 \qquad (2.24)$$

Thermal force induces a pre-pore, but its radius decreases when its radius falls below a threshold radius ($< r_p^*$). This threshold radius [$r_p^* = \Gamma/(\sigma + B)$] corresponds to a maximum in the free energy [$\Omega_{max} = \pi\Gamma^2/(\sigma + B)$], which is the energy barrier for pore formation as shown in Fig. 2.7 (a). Conversely, if thermal force increases the pre-pore radius equal or larger than the threshold ($\geq r_p^*$), a pre-pore is transformed into a pore in the membrane.

When PGLa interacts with a single GUV, if a pre-pore is formed near the location of PGLa in the outer monolayer, PGLa can attach to the edge of a pre-pore, which makes the edge more stable and reduce its free energy, i.e., Γ. This enhances the lifetime of the pre-pore. If a pre-pore has a toroidal pore structure, lipid molecules can rapidly diffuse between the outer and the inner monolayer through the pre-pore wall because these monolayers are connected at the pre-pore edge. Thus, PGLa and the bound lipids can diffuse together from the outer to the inner monolayer through the pre-pore wall. This scenario can explain the transfer mechanism of PGLa without nanopore formation. Fig. 2.7 (b) indicate that as σ increases the slope of the curve [Ω (r_p) vs. r_p] below 10 k_BT of Ω is decreased. Thus, it is expected that as σ increases thermal force can increase the pre-

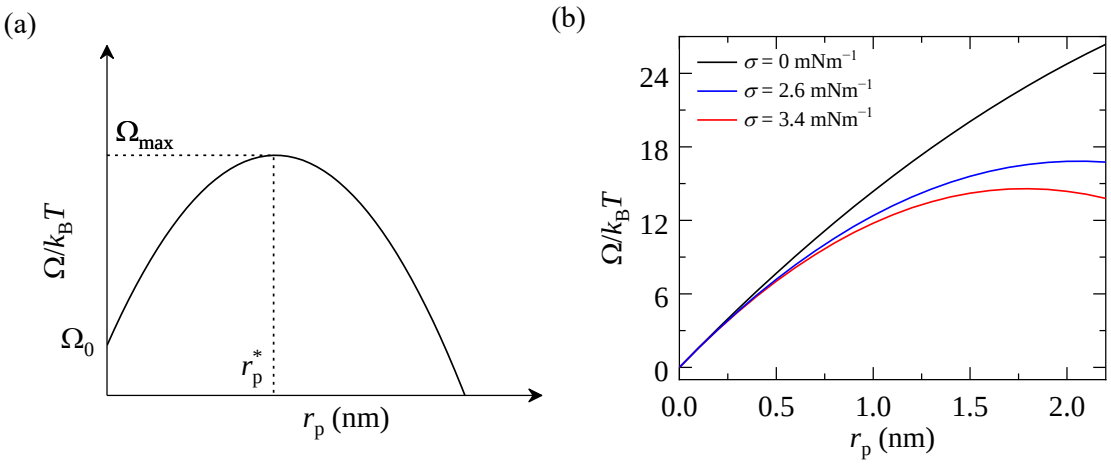

Figure 2.7: Free energy of a pre-pore in a lipid bilayer as a function of pre-pore radius and membrane tension. (a) Free energy (Ω) of a pre-pore vs. pre-pore radius (r_p) for a fixed membrane tension. At a threshold radius, r_p^*, the free energy is maximum, Ω_{max}. (b) Dependence of the free energy profile on membrane tension. The curves are plotted using Eq. (2.24) and Γ = 10.7 pN for DOPC/DOPG (6/4)-GUVs (Tazawa and Yamazaki, 2023). Black, blue, and red lines are drawn for σ = 0, 2.6 and 3.4 mN m^{-1}, respectively.

pore radius and the rate of pre-pore formation further. For this reason, membrane tension may enhance the rate of PGLa transfer across the pre-pore of the lipid bilayer without nanopore formation. This scenario is similar to the increasing rate of TP10 transfer in absence of pores with increasing the micropipette aspiration-induced σ (Islam et al., 2017).

This membrane tension-enhanced rate of PGLa transfer across the lipid bilayer is one of the causes of the higher rate of PGLa-induced nanopore formation since the symmetric binding of PGLa across the bilayer is required for the nanopore formation. In the case of Mag, membrane tension enhances the rate constant of nanopore formation (k_p^{Mag}) (Billah et al., 2022), but its cause is different from that for PGLa. For the mechanism underlying the Mag-induced nanopore formation in the absence of tension, the stretch-activated model has been considered (Karal et al., 2015a; Billah et al., 2024). The asymmetric binding of Mag across the bilayer is retained just before pore formation. The binding of

Mag in the outer monolayer increases the area of a GUV bilayer, inducing the stretching of the inner monolayer, and as a result, the membrane tension of the inner monolayer increases. This tension induces the instability of the inner monolayer, which triggers a nanopore formation in the bilayer. As the surface concentration of Mag in the outer monolayer increases, the δ increases, which enhances the inner monolayer tension. Thus, k_p^{Mag} increases with an increase in the surface concentration of Mag (Karal et al., 2015a). In the presence of membrane tension due to Π, the total tension in the inner monolayer of a GUV interacting with Mag is the summation of the membrane tension due to the binding of Mag and the membrane tension due to Π. This enhanced membrane tension in the inner monolayer due to Π, increases the k_p^{Mag}.

2.6 Conclusion

In this chapter, the effects of σ on PGLa-induced nanopore formation in DOPC/DOPG (6/4)-GUVs are described and discussed. Using the Π method to apply membrane tension to GUVs, I observed successfully the PGLa-induced nanopore formation in the lipid bilayers under σ and the evolution of pores. I found that membrane tension enhances the rate of PGLa-induced nanopore formation. It turned out that one of the reasons of this effect is the increase in the rate of transfer of PGLa from the outer to the inner monolayer without pore formation with increasing σ because the symmetric binding of PGLa is required for its pore formation. Under membrane tension less than 3.4 mN m^{-1}, PGLa did not induce micropore formation nor GUV burst, but the membrane permeability coefficient increases with time to reach a maximum, steady value, P^s, which is enhanced by osmotic pressure. The former result is highly contrast with that for Mag-induced nanopore formation where GUV burst occurs after the growth of a micropore in the GUV membrane at even $\sigma = 2.6$ mN m^{-1} (Billah et al., 2022). These characteristics of the evolution of PGLa-induced nanopore under membrane tension suggest that PGLa may not induce a toroidal type nanopore. The membrane tension-enhanced rate of transfer of PGLa across the lipid bilayer without pore formation is explained reasonably by the pre-pore model because the membrane tension-enhanced rate of production of a pre-pore and its size can be predicted by the theory.

Appendix

(Free energy of a lipid bilayer with a repulsive interaction proportional to a^{-2})

As described previously in the section 2.3.1, the general form of repulsive interaction in the equation of the free energy of an electrically neutral lipid bilayer is J_n/a^n where J_n is a parameter that describes the repulsive interaction between electrically neutral lipids and a is the area per lipid in the lipid bilayer (Marsh, 1996). Here, I express the theory for $n = 2$ (i.e., J_2/a^2).

A hydrocarbon chain of lipid molecules can be considered as a polymer chain comprising n_s segments, where a segment behaves as a rigid rod and at the joint of two segments they can rotate freely (i.e., freely jointed polymer model) (Rawicz et al., 2000). This hydrocarbon chain can adopt various conformations, resulting in different values of chain length (l_{hc}) in the direction of the normal of membrane surface. If it is approximated that all conformations have the same energy, the entropy (S_{hc}) of a hydrocarbon chain with a chain length of l_{hc} can be obtained using the total number of its conformations (W_{ch}) as follows,

$$S_{\mathrm{hc}} = k_B ln W_{ch} = \mathrm{const} - \frac{3k_B l_{hc}^2}{2\beta^2 n_s} \qquad (\mathrm{A}.1)$$

where β is the segment length, which is approximately twice the persistence length of the chain. The Helmholtz free energy of a lipid hydrocarbon chain (F_{ch}) can be described as follows, since the energy of the chain does not depend on its length, l_{hc}.

$$F_{\mathrm{hc}} = \frac{3k_B T l_{hc}^2}{2\beta^2 n_s} + \mathrm{const} \qquad (\mathrm{A}.2)$$

The volume of lipid hydrocarbon chain remains constant when its conformation changes (even if its large change occurs in the gel to L_α phase transition occurs). Thus, using the volume of a hydrocarbon chain (V_{hc}), the chain length can be described as follows.

$$l_{\mathrm{hc}} = \frac{V_{\mathrm{hc}}}{a_{\mathrm{hc}}} = \frac{2V_{\mathrm{hc}}}{a} \qquad (\mathrm{A}.3)$$

Here, $a = 2a_{hc}$ is used since the area per lipid molecule (a) is defined as its area at the interface between the hydrocarbon chain and the headgroup. Thus, the free energy of a lipid bilayer composed of $2N$ lipid molecules, $F(a)$, can be described as follows.

$$F(a) = 2N\left(\frac{6k_BTV_{hc}^2}{\beta^2 n_s}\right)\frac{1}{a^2} = 2N\frac{J_2}{a^2} \qquad (A.4)$$

where J_2 is a quantity that characterizes the repulsion between lipids that have no electrical charge. In this case, Eq. (2.6) in section 2.3.1 takes the following form.

$$F^{\mathrm{neu}} = 2N\left(\gamma a + \frac{J_2}{a^2}\right) \qquad (A.5)$$

When a neutral lipid bilayer is stretched, $a > a_{fr}$ and σ^{neu} appeared as expressed below,

$$\sigma^{\mathrm{neu}} = \left(\frac{\partial F^{\mathrm{neu}}}{\partial A}\right) = 2\left(\gamma - \frac{2J_2}{a^3}\right) \qquad (A.6)$$

where A (= Na) is the total area of a GUV membrane.

The electrostatic contribution to the membrane tension (σ^{el}) in a charged membrane is the same as Eq. (2.8) in the section 2.3.1.

$$\sigma^{\mathrm{el}} = -\frac{X^2e^2}{\varepsilon_{\mathrm{w}}\varepsilon_0\kappa}\frac{1}{a^2} = -2\frac{J^{\mathrm{el}}}{a^2} \qquad (A.7)$$

Here, J^{el} describes the repulsive electrostatic interaction between charged lipid molecules. Therefore, the total membrane tension, σ, is obtained from summation of the neutral and electrostatic part as follows,

$$\sigma = \sigma^{\mathrm{neu}} + \sigma^{\mathrm{el}} = 2\left(\gamma - \frac{J^{\mathrm{el}}}{a^2} - \frac{2J_2}{a^3}\right) \qquad (A.8)$$

Hence, the total free energy, F can be described by the equation below.

$$F = 2N\left(\gamma a + \frac{J^{\mathrm{el}}}{a} + \frac{J_2}{a^2}\right) \qquad (\mathrm{A.9})$$

The minimum value of F can be obtained at $a = a_{\mathrm{fr}}$ when the lipid bilayer is in mechanical equilibrium (i.e., $\sigma = 0$). If a_{fr} changed to a by Δa, then $a = a_{\mathrm{fr}} + \Delta a$. If $\Delta a / a_{\mathrm{fr}} << 1$, σ at a, is given by,

$$\sigma(a) = \sigma(a_{\mathrm{fr}} + \Delta a) \approx \frac{4}{a_{\mathrm{fr}}^4}\left(J^{el} a_{\mathrm{fr}} + 3J_2\right)\Delta a \qquad (\mathrm{A.10})$$

where $J^{\mathrm{el}} > 0$ and $J_2 > 0$. Eq. (A.10) indicates that if $a > a_{\mathrm{fr}}$ (i.e., $\Delta a > 0$), $\sigma(a) > 0$ and if $a < a_{\mathrm{fr}}$ (i.e., $\Delta a < 0$), $\sigma(a) < 0$. Due to this change in area per lipid, the free energy (F) increases by dF and thus expressed as follows,

$$\begin{aligned} dF &= 2N\left[\gamma(a + da) + \frac{J^{\mathrm{el}}}{a + da} + \frac{J_2}{(a + da)^2} - \gamma a - \frac{J^{\mathrm{el}}}{a} - \frac{J_2}{a^2}\right] \\ &= 2N\left(\gamma - \frac{J^{\mathrm{el}}}{a^2} - \frac{2J_2}{a^3}\right) da \\ &= \sigma dA \end{aligned} \qquad (\mathrm{A.11})$$

Since the same Eq. (2.12) in the section 2.3.1 can be used, the equation of the pressure difference between the inside and the outside of a GUV, ΔP, can be expressed as follows.

$$\Delta P = P_{\mathrm{in}} - P_{\mathrm{out}} = \frac{2\sigma}{r} \qquad (\mathrm{A.12})$$

If I use the equation for $n = 2$ (i.e., J_2/a^2) as the repulsive interaction, the total membrane tension, σ, can be expressed by Eq. (A.8), which is different from Eq. (2.9) in the section 2.3.1 obtained using $n = 1$ (i.e., J/a). However, Eq. (A.12) is the same as Eq. (2.13) in the section 2.3.1 which expresses the relationship between ΔP and σ.

CHAPTER THREE

Effect of line tension at the edge of a pre-pore on PGLa-induced pore formation

3.1. Introduction

Here, I consider two physical quantities describing important physical properties of lipid bilayers: the line tension (Γ) at the pre-pore edge and the spontaneous curvature of lipid monolayer (H_0). As described in section 1.5, the line tension at the pre-pore edge plays a vital role in the tension-induced pore formation and the rupture of lipid vesicles. In the transfer of CPPs across lipid bilayers, there is a mechanism based on a pre-pore (the pre-pore model) (Islam et al., 2018), and the rate of transfer of nona-arginine (R_9) and transportan 10 (TP10) is greatly affected by the Γ value (Hasan et al., 2019; Islam et al., 2017; Sharmin et al., 2016). Therefore, to elucidate the mechanism of PGLa-induced nanopore formation, it is indispensable to elucidate the effect of the line tension at the pre-pore edge on the PGLa-induced nanopore formation.

On the other hand, the monolayer spontaneous curvature (H_0) (see its definition in the later section 3.3) is well known to determine the phase stability of lipid membranes. For example, phosphatidylethanolamine (PE) monolayer and monoolein (MO) monolayer have a negative spontaneous curvature, and thus, these lipids tend to form the hexagonal II (H_{II}) phase and inverse bicontinuous cubic (Q_{II}) phase, depending on temperature and water content (Kinoshita et al., 2001; Li et al., 2001; Marsh, 1996; Rand et al., 1990; Seddon and Templer, 1995; Yamazaki, 2009). In contrast, the spontaneous curvature of phosphatidylcholine (PC) monolayer is almost 0 (Kollmitzer et al., 2013). The value of H_0 can be determined by small angle X-ray scattering (SAXS) using the H_{II} phase (see the details in the later section 3.3). For example, the H_0 value of DOPE/DOPG (6/4) in 150 mM NaCl was -0.22 nm^{-1}, indicating a negative curvature (Alley et al., 2008), whereas the H_0 value of DOPC/DOPG (6/4) is almost 0 because the two constituent lipids have the H_0 value of nearly 0. Moreover, the spontaneous curvature of lipid monolayer affects the shape change of lipid bilayers, membrane fusion, and vesicle fission. Thus, the spontaneous curvature of lipid monolayer may affect the PGLa-induced nanopore formation and its stability.

A recent study indicates experimentally that the value of Γ at the pre-pore edge depends greatly on the H_0 value based on the analysis of the constant tension-induced rupture (burst) of GUVs of various lipid compositions (Tazawa and Yamazaki, 2023). According to this study, the Γ in DOPE/DOPG (6/4) bilayer (15.6 pN) is much larger than

that in DOPC/DOPG (6/4) bilayer (10.7 pN).

In this chapter, I examined the effect of the line tension at the pre-pore edge on PGLa-induced nanopore formation using the single GUV method. Based on the study on the relationship between Γ and H_0 (Tazawa and Yamazaki, 2023), I selected DOPE/DOPG (6/4)-GUVs and DOPC/DOPG (6/4)-GUVs for this project, because the values of Γ at the pre-pore edge are very different in these bilayers which have the same surface charge density. It is important to use such lipid bilayers because the electrostatic interactions due to their surface charges greatly affect the interaction of AMPs with the lipid bilayers and AMPs-induced membrane damage such as nanopore formation. Here, I investigated the interaction of PGLa with single DOPE/DOPG (6/4)-GUVs, and compared the results with those obtained for DOPC/DOPG (6/4)-GUVs (Chap. 2). First, I studied the PGLa-induced AF488 membrane permeation from the inside of single DOPE/DOPG (6/4)-GUVs using FLM, to understand the effect of DOPE on the rate of pore formation by PGLa. I found that PGLa induces nanopore formation in the GUV membrane, but also induces burst of the GUVs and local burst. Generally, GUV burst (including both local burst and (complete) burst) is defined as the action of AMPs on a GUV where rapid membrane permeation occurs concomitantly with a decrease in GUV diameter, and for the (complete) burst of a GUV, the structure of the GUV is transformed into lipid membrane aggregates (Billah et al., 2024). Then, to reveal the mechanism underlying the PGLa-induced membrane permeation in GUVs, I examined the connection between the location of PGLa in the lipid bilayer and AF647 membrane permeation. For this reason, I examined the interaction of a mixture of PGLa/CF-PGLa with DOPE/DOPG (6/4)-GUVs using CLSM. To clarify the process of the GUV burst in detail, by doping a small molar fraction of a fluorescent lipid (NBD-PE) in DOPE/DOPG (6/4)-GUVs (i.e., DOPE/DOPG/NBD-PE (60/39/1)), I observed the PGLa-induced structural change of the GUVs at a high time resolution (10 ms) using FLM. Based on the obtained results, I discussed the mechanism of PGLa-induced burst of DOPE/DOPG (6/4)-GUVs, and compared the results of DOPE/DOPG (6/4)-GUVs with those of DOPC/DOPG (6/4)-GUVs.

3.2. Materials and methods

3.2.1. Chemicals

DOPE and 1,2-dioleoyl-*sn*-glycero-3-phosphoethanolamine-N-(7-nitro-2-1,3-benzoxadiazole-4-yl) (NBD-PE) were purchased from Merck & Co. Purchase information of other lipids, chemicals and reagents are the same as that in section 2.2.1.

3.2.2. Preparation and purification of several kinds of GUVs

DOPE/DOPG (6/4) GUVs encapsulating AF488 (or AF647) were prepared in buffer (10 mM PIPES, 150 mM NaCl and 1 mM EGTA; pH 7.0) comprising 100 mM sucrose and 6 μM AF488 (or AF647) using the natural swelling method described in section 2.2.2 for membrane permeation experiments. In case of the experiments to observe the structural change in GUVs in the interaction with PGLa, DOPE/DOPG/NBD-PE (60/39/1)-GUVs were prepared in buffer comprising 100 mM sucrose by the same technique as used for DOPE/DOPG (6/4)-GUVs. These GUVs were purified using the membrane filtering method (see the details in section 2.2.2).

3.2.3. PGLa and CF-PGLa synthesis, purification, and identification

The same methodology as described in section 2.2.4. was used for the synthesis, purification, and identification of PGLa and CF-PGLa.

3.2.4. PGLa-induced AF488 membrane permeation and the location of CF-PGLa in GUVs during their interaction

The experiments for AF488 permeation through the bilayer and the location of CF-PGLa across the bilayer were performed utilizing the same approach those used in section 2.2.5.

3.2.5. Structural change of GUVs during the interaction with PGLa

To enhance the contrast of GUV membrane in the microscopic observation, DOPE/DOPG membranes of the GUVs were doped with a low concentration of fluorescent lipid, NBD-PE as DOPE/DOPG/NBD-PE (60/39/1)-GUVs. PGLa in buffer comprising glucose was loaded to a 20-μm-diameter micropipette and applied to the

single GUVs from 70 μm distance by 30 Pa positive pressure as illustrated in Fig. 2.1. The fluorescence intensity of the membrane of GUVs due to NBD-PE was measured using a digital CMOS camera (ORCA-Flash 4.0 v3). An ND-25 filter was used to attenuate the incident light from a mercury arc lamp, which decreased the photobleaching of NBD-PE. High speed streaming mode was used to record the video at 10 ms exposure time and 36,000 maximum frames within 6 min. The other conditions of CMOS camera were used as binning: 2, sub-array: 512 × 256 pixels and video format: dcimg. HCImage software (v4.8) was used to analyze the structural change of the GUVs.

3.3. Theory

Here, I describe the basic theory of two physical quantities: monolayer spontaneous curvature and the line tension at the edge of a pre-pore. Spontaneous curvature (H_0) is an intrinsic property of lipid monolayers in a solution without interacting with another monolayer, which is defined as the monolayer curvature with a minimum bending energy of the monolayer. Fig. 3.1 (a) shows three different types of monolayers with (1) zero ($H_0 = 0$), (2) negative ($H_0 < 0$) and (3) positive ($H_0 > 0$) spontaneous curvature. The monolayer

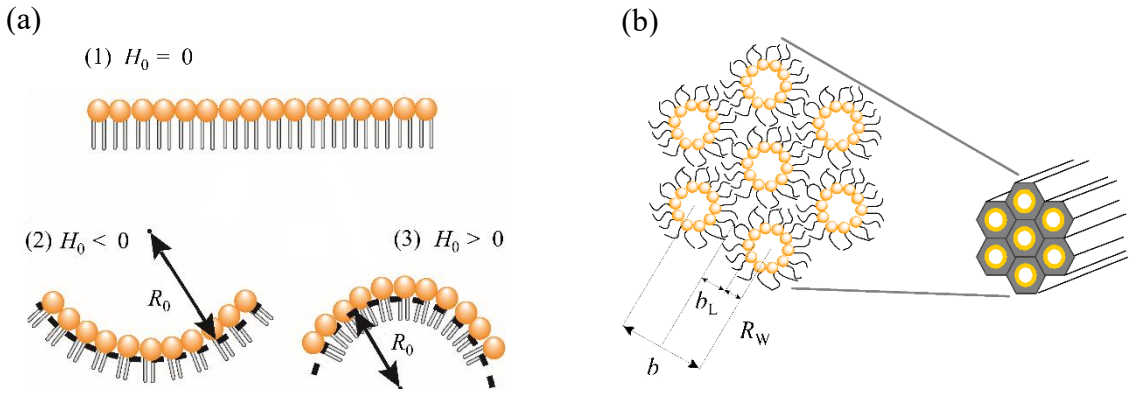

Figure 3.1: Scheme of monolayer spontaneous curvature, H_0. (a) A lipid monolayer with (1) zero (2) negative and (3) positive spontaneous curvature. R_0 is the radius of spontaneous curvature. (b) Structure of a hexagonal II (H_{II}) phase. Lipid monolayer bends to form a cylinder containing a narrow water channel which contacts with its lipid headgroups, and many cylinders pack hexagonally. b (= $2(b_L + R_W)$) is the distance between the center of the neighboring cylinders, b_L is the monolayer thickness and R_W is the radius of curvature of lipid monolayer. These figures are reprinted from the ref. (Yamazaki, 2009) with a permission of Elsevier.

spontaneous curvature is determined by the molecular structure of constituent lipids, intermolecular interactions, and interaction between solutions (such as solvents and ions) and the lipid bilayers. There are several methods to determine the H_0 of lipid monolayers. One of the typical methods is the measurement of distance (b) between the center of the neighboring cylinders in the H_{II} phase doped with hydrocarbon to eliminate the packing energy in the interstitial region of the hexagonal packing of cylinders (Fig. 3.1. (b)). This distance b depends on water contents in a lipid suspension. As water content changes under the excess water condition (i.e., water exists outside the lipid membranes in the H_{II} phase), the value of b remains constant, whereas under the non-excess water condition, the value of b decreases with decreasing water content. To determine the value of H_0, it is necessary to measure the value of b under the condition of a specific water content (i.e., the maximum water content under non-excess water condition). Based on this measurement, the radius of spontaneous curvature (R_0) is determined as the radius of the water channel in the cylinder (Fig. 3.1. (b)), and thus, $|H_0|$ is defined as the inverse of R_0 under this condition (i.e., $|H_0| = R_0^{-1}$).

The values of monolayer spontaneous curvature of various lipids have been reported. The H_0 values of DOPE and DOPC are -0.36 nm^{-1} (Alley et al., 2008) and -0.0091 nm^{-1} (Kollmitzer et al., 2013), respectively. Therefore, pure DOPE membrane forms the H_{II} phase at room temperature (Kinoshita et al., 2001), but DOPC membrane forms the L_α phase. The H_0 value of DOPG in 150 mM NaCl are -0.0067 nm^{-1} (Alley et al., 2008). The values of spontaneous curvature of monolayers comprising DOPE and DOPG at various ratios have been measured, and the H_0 value of DOPE/DOPG (6/4) in 150 mM NaCl was -0.22 nm^{-1} (Alley et al., 2008), as described in the introduction (section 3.1). On the other hand, the H_0 value of DOPC/DOPG (6/4) has not yet been measured, but based on the H_0 values of DOPC and DOPG, it can be inferred that -0.0091 nm^{-1} < H_0 of DOPC/DOPG (6/4) < -0.0067 nm^{-1}, indicating the H_0 value of DOPC/DOPG (6/4) is nearly 0. The curvature elastic energy (E) of a monolayer is related to its spontaneous curvature and bending rigidity. According to the continuum theory (Helfrich, 1973),

$$E = \int \{2\kappa_B(H - H_0)^2 + \overline{\kappa_B} K^G\}\, dA, \qquad (3.1)$$

where κ_B is the bending rigidity, H is the mean curvature of the monolayer, $\overline{\kappa_B}$ denotes saddle-splay modulus or Gaussian curvature modulus and K^G is the Gaussian curvature.

The definition of line tension (Γ) at the edge of a pre-pore is described in section 1.5. There are several methods to determine the value of Γ at the edge of a pre-pore. The experiments of constant-tension-induced GUV rupture (burst) are used for this purpose (Karal et al., 2015b; Levadny et al., 2013). The constant tension (σ) is applied to a GUV using its aspiration into a micropipette. If a pore is formed in the GUV membrane, it is rapidly (at least, less than 1 s and for most tension, less than 33 ms) aspirated into the micropipette completely. It is considered that immediately after pore formation the GUV burst may occur due to the membrane tension, and then the GUV is aspirated into the inside of the micropipette owing to the pressure difference. Thus, the time of aspiration of a GUV is approximated as that of GUV rupture as well as that of pore formation. If many GUVs are examined under the same condition, each GUV is aspirated at different time. This GUV rupture can be considered as a transition from the intact state to the ruptured state, and thus, a theoretical equation for the rate of constant-tension-induced GUV rupture is obtained. The experimental results of the rupture of many GUVs can be expressed as the time course of the fraction of intact GUVs (i.e., non-aspirated GUVs), P_{intact}, among all examined GUVs. By the fitting of the theoretical equation to the experimental data of the time course of P_{intact}, the rate constant of constant-tension-induced GUV rupture (k_r) is determined. As the theory of the tension-induced pore formation, Eq. (2.24) (the free energy of a pre-pore in a lipid bilayer, Ω) can be used. According to this theory, thermal force induces the fluctuation of the pre-pore radius, and if it reaches the threshold radius (r_p^*), a pre-pore converts into a pore. Therefore, if one knows the time when the pre-pore radius reaches r_p^* for the first time, the rate of pore formation is evaluated. For this purpose, the concept of mean-first passage time (MFPT), which has been used in the diffusion theory, has been applied (Levadny et al., 2013), because the random walk of a single molecule in the diffusion process is similar to the fluctuation of the pre-pore radius and both of them are driven by thermal force. The MFPT (τ) required for a pre-pore to reach r_p^* is calculated as a function of σ, Γ, and diffusion coefficient determining the fluctuation of the pre-pore radius. The k_r is the inverse of τ since the MFPT is the life-time of a pre-pore, which can be expressed as follows,

$$k_{\mathrm{r}} = \frac{1}{\tau} = \left(\frac{D_r\sqrt{3}}{k_{\mathrm{B}}T}\right)(\sigma + B)\exp\left\{-\frac{\pi\Gamma^2}{k_{\mathrm{B}}T(\sigma + B)}\right\}, \tag{3.2}$$

where D_r is the diffusion coefficient of a particle in r-phase space, which determines the damping force when fluctuation of r_{p} occurs. The experimental results of σ dependence of k_{r} (e.g., Fig. 3.2. (a)) is fitted by the inverse of MFPT, providing the values of Γ. These values obtained by the MFPT analysis are almost the same as those obtained by another method, demonstrating that the MFPT analysis is a reliable method. Next, an experimental method to determine the values of Γ has been developed (Karal et al., 2016; Karal and Yamazaki, 2015). In this method, first, the temperature dependence of k_{r} is measured to determine the activation energy, $\Omega_{\max}$, of pore formation. Then, the values of $\Omega_{\max}$ are measured as a function of σ. The relation between $\Omega_{\max}$ and $1/(\sigma + B)$ is linear, and the slope of this linear curve provides the values of Γ. This analysis leads to a finding of a new term of Ω which does not depend on membrane tension, Ω_0, and a new expression of $\Omega_{\max}$ as follows,

$$\Omega_{\max} = \Omega_0 + \frac{\pi\Gamma^2}{\sigma + B}\ . \tag{3.3}$$

The new term Ω_0 is interpreted as the nucleation free energy of the initial formation of a toroidal type hydrophilic pre-pore (Karal and Yamazaki, 2015). This experimental method has enabled us to obtain the energy barrier of tension-induced pore formation directly and the nucleation free energy for the first time. However, it requires a long time to perform many experiments to obtain the value of Γ and Ω_0, which is the disadvantage of this method. Moreover, the presence of Ω_0 prevents the accurate calculation of MFPT.

Recently, a new, simple method has been developed (Tazawa and Yamazaki, 2023). The k_{r} can be expressed by $\Omega_{\max}$ using the Arrhenius equation as,

$$k_{\mathrm{r}} = A\exp\left(-\frac{\Omega_0 + \frac{\pi\Gamma^2}{\sigma + B}}{k_{\mathrm{B}}T}\right), \tag{3.4}$$

where A denotes a frequency factor. Re-arrangement of Eq. (3.4) provides the following equation:

$$\ln k_{\mathrm{r}} = \left(\ln A - \frac{\Omega_0}{k_{\mathrm{B}}T}\right) - \frac{\pi\Gamma^2}{k_{\mathrm{B}}T}\left(\frac{1}{\sigma + B}\right) = C - \frac{\pi\Gamma^2}{k_{\mathrm{B}}T}\left(\frac{1}{\sigma + B}\right), \qquad (3.5)$$

where $C = [\ln A - (\Omega_0/k_{\mathrm{B}}T)]$. In Fig. 3.2 (b), the experimental data of ln k_{r} vs. $1/(\sigma + B)$ are fitted with Eq. (3.5) which provides the slope ($\pi\Gamma^2/k_{\mathrm{B}}T$) and intercept C. From this fitting, Γ values were determined as 15.6 ± 0.7 pN for DOPE/DOPG (6/4)-GUVs and 10.7 ± 0.4 pN for DOPC/DOPG (6/4)-GUVs (Tazawa and Yamazaki, 2023). These values of Γ agree with the Γ values obtained by the MFPT analysis using the same data set and assuming $\Omega_0 = 0$ (Tazawa and Yamazaki, 2023). They also calculated the value of Γ for the GUVs containing 18:1 Lyso-PC in the membrane which has a positive H_0. In this case, the value of Γ for DOPC/DOPG/Lyso-PC (55/40/10)-GUVs was 6.7 ± 0.2 pN (Tazawa and Yamazaki, 2023). From these experimental results of Γ, it is obvious that line tension increases with decreasing monolayer spontaneous curvature.

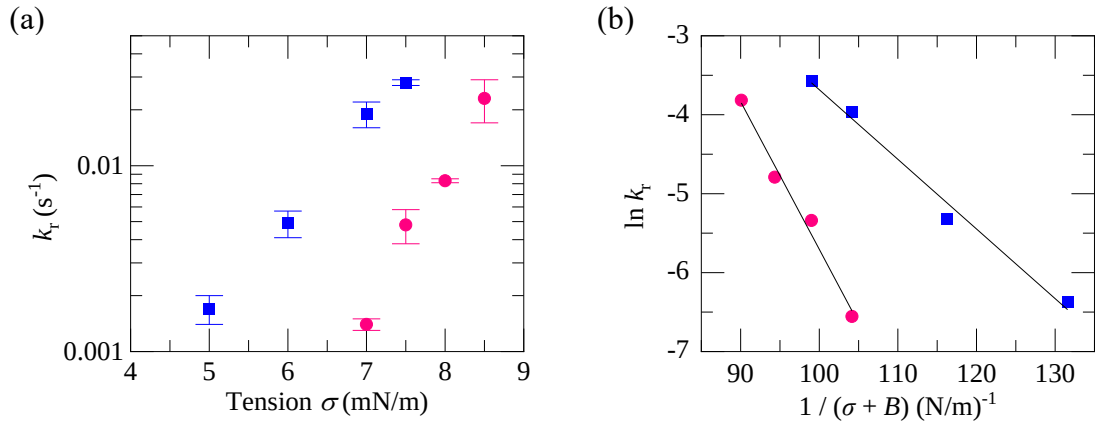

Figure 3.2: Determination of line tension (Γ) by Arrhenius equation. The graphs are reprinted from ref. (Tazawa and Yamazaki, 2023) with permission from AIP publishing. (a) Experimentally obtained values of k_{r} with different σ for DOPC/DOPG (6/4)-GUVs (blue ■) and DOPE/DOPG (6/4)-GUVs (red ●). (b) The solid lines: Best fitted curve using Eq. (3.6) provided Γ = 15.6 pN for DOPE/DOPG (6/4)-GUVs and Γ = 10.7 pN for DOPC/DOPG (6/4)-GUVs.

Here, I consider the relationship between Γ and H_0 theoretically. It is considered that a main factor determining the value of Γ is the curvature elastic energy (E) of a pre-pore wall as a monolayer. To determine this energy, I try to use the Helfrich equation (Eq. 3.1). The first term in Eq. (3.1) is determined by H_0 and the mean curvature, H. The pre-pore wall has various values of curvature, depending on the location of a point and the radius of the pre-pore. The side-view of a pre-pore in chapter 1 (Fig. 1.4a) shows maximum curvature (C_{max}) of the monolayer at the pre-pore wall, but in the top view of the midplane of the lipid bilayer shows minimum curvature (C_{min}). Generally, the mean curvature (H) of a point in a 3-dimensional surface is defined as $(C_{max} + C_{min})/2$. In the case of a pre-pore wall, the value of C_{max} is the same for all points, but the value of C_{min} depends on the location of a point: if the point locates in the midplane of the bilayer, it has the maximum negative value. As the radius of a pre-pore decreases, the absolute value of C_{min} greatly increases (i.e., the negative curvature increases). Thus, in a pre-pore, $H < 0$ in some cases. In contrast, for a micropore whose radius is order of micrometer, $C_{min} \sim 0$, and thus, $H = C_{max}/2$, which is always positive. On the other hand, the curvature elastic energy (E) of a monolayer due to the saddle bending elasticity ($\int \overline{\kappa_B} K^G \, dA$) is estimated using the Gauss–Bonnet theorem and the value of $\overline{\kappa_B}$, which provides the estimation of Γ due to the saddle bending elasticity by assuming that the value of Γ is determined only by the value of E (Tazawa and Yamazaki, 2023). This analysis indicates that the value of Γ due to the saddle bending elasticity is large compared with its experimental values and independent of the pre-pore radius, and thus, it might be related to Ω_0. Therefore, the curvature elastic energy of a pre-pore wall which does not depend on its radius (ΔE) can be expressed based on Eq. (3.1) as follows,

$$\Delta E = \int \{2\kappa_B (H - H_0)^2\} \, dA. \qquad (3.6)$$

The above experimental results (i.e., Γ increases with decreasing H_0) indicates that the contribution of the points with a positive mean curvature in a pre-pore wall is large, which may disagree with the above analysis of the mean curvature of a pre-pore. This disagreement as well as larger evaluation of Γ due to the saddle bending elasticity may

suggest that Helfrich equation (Eq. 3.1) for the continuum mechanics cannot be used for the estimation of the curvature elastic energy of a pre-pore wall.

3.4. Results

3.4.1. PGLa-induced AF488 membrane permeation from single DOPE/DOPG (6/4)-GUVs

To understand the effect of line tension at the pre-pore edge on the rate of pore formation by PGLa, I studied the membrane permeation of AF488 from the inside of single DOPE/DOPG (6/4)-GUVs. The results of the interaction of 14 μM PGLa with DOPE/DOPG (6/4)-GUVs showed several patterns of membrane permeation and structural changes of GUVs. Fig. 3.3(a) shows that after the AF488 membrane permeation the diameter and the shape of the GUV were the same as those before the interaction with PGLa, indicating that PGLa induces nanopore formation in the bilayer. To analyze the membrane permeation of AF488 more quantitatively, the time course of $I_N(t)$ of the GUV lumen due to AF488 was plotted (Fig. 3.3(d)). $I_N(t)$ started to decrease at 234 s, indicating that the AF488 membrane permeation from the GUV lumen started at this time. Thus, the onset time of nanopore formation is 234 s. After the onset time, a three-step decrease in the $I_N(t)$ was observed. In contrast, Fig. 3.3(b) shows that after the membrane permeation of AF488 the diameter of the GUV was reduced significantly from the initial one, indicating that local burst of GUV occurred (Billah et al., 2024). Moreover, several high contrast particles and apparent small vesicles appeared in the GUV lumen and on the GUV membrane, which is different from the Mag-induced local burst of GUVs under osmotic pressure, where no high contrast particles appeared (Billah et al., 2022). Fig. 3.3(e) shows that $I_N(t)$ started to decrease at 225 s, indicating that the onset time of nanopore formation is 225 s. After the onset time, initially a stepwise decrease in $I_N(t)$ occurred followed by a gradual decrease, and finally $I_N(t)$ became zero at 360 s. In some cases of PGLa-induced local burst of GUVs, only gradual decrease in $I_N(t)$ without stepwise decrease was observed (Fig. 3.3(c), (f)).

I examined 16 single GUVs (m = 16) under the same conditions. Fig. 3.3(g) shows the time course of $I_N(t)$ of several GUVs among them. Different onset time of membrane permeation of AF488 was observed for different GUVs, indicating that pore formation

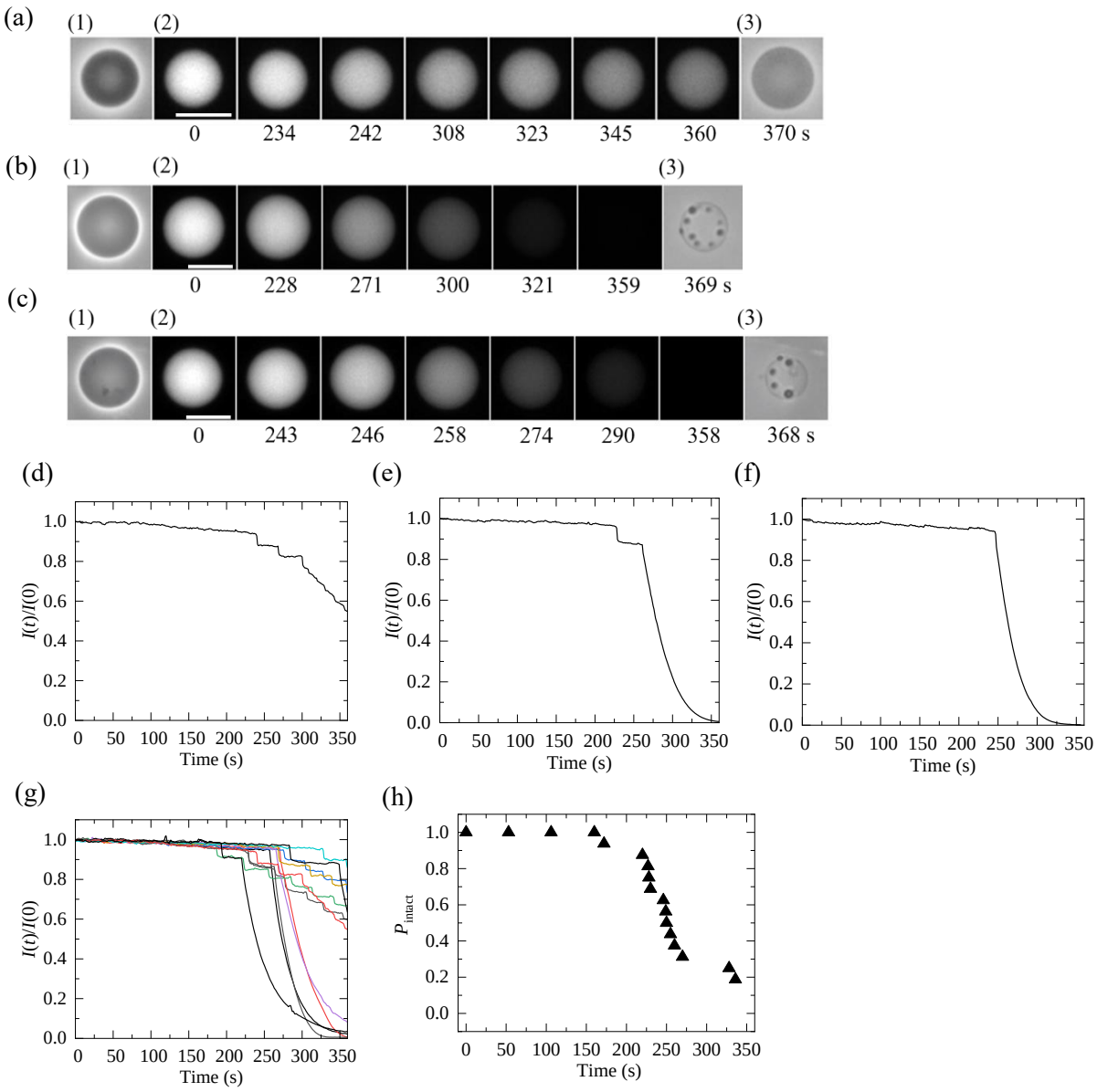

Figure 3.3: PGLa-induced membrane permeation of AF488 from single DOPE/DOPG (6/4)-GUVs. (a), (b) and (c) Phase contrast (panel (1) and (3)) and fluorescence microscopic images due to AF488 (panel (2)) of three typical single GUVs interacting with 14 µM PGLa. Bar, 20 µm. The number below each image denotes the interaction time. (a) nanopore formation and (b), (c) local burst of the GUVs. (d), (e) and (f) time courses of change in normalized fluorescence intensity, $I_N(t)$, of the GUVs shown in panel a, b and c, respectively. (g) $I_N(t)$ for many single GUVs in the interaction with 14 µM PGLa. (h) Time course of P_{intact} for 14 µM PGLa.

occurred stochastically. The number of steps during the decrease in $I_N(t)$ was also different, ranging from 0 to 5. Judging from the phase contrast image of the GUVs after 6 min interaction with PGLa, the numbers of GUVs where nanopore formation, local burst and burst occurred were 8, 4 and 1, respectively, while the other GUVs were intact, i.e., no membrane permeation was observed.

PGLa-induced nanopore formation, GUV local burst and burst are apparently different phenomena. However, as discussed in later sections, PGLa-induced GUV local burst and burst originate from the nanopore formation. Here, a result supporting this conclusion is shown. Fig. 3.4 shows the result of the interaction of 14 μM PGLa with DOPE/DOPG (6/4)-GUVs (under the same conditions as Fig. 3.3) for 8 min. The $I_N(t)$ of the GUV lumen decreased significantly at 400 s, whereas the GUV diameter did not change, indicating nanopore formation. However, the fluorescence image of the GUV at 471 s indicates the decrease in GUV diameter, and the phase contrast image at 490 s shows aggregates of lipids, indicating that burst of the GUV occurred. This result shows that first nanopore formation occurs and later GUV burst occurs, suggesting that PGLa-induced GUV burst originates from the nanopore formation.

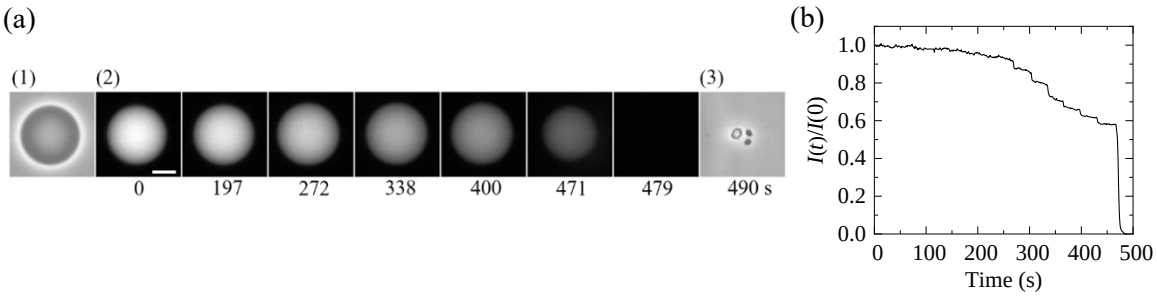

Figure 3.4: PGLa-induced AF488 membrane permeation from a single DOPE/DOPG (6/4)-GUV for 8 min interaction. (a) Phase contrast (panel 1 and 3) and fluorescence images due to AF488 (panel 2) of the GUV interacting with 14 μM PGLa. Bar, 20 μm. The number below each image indicates the interaction time. (b) Change in $I_N(t)$ of the GUV shown in panel a over time.

As described in Chap. 2, the fraction of intact GUVs among all GUVs, $P_{intact}(t)$, is used as a measure of the rate of PGLa-induced nanopore formation. If the GUV local burst and burst originate from the PGLa-induced nanopore formation, i.e., in the initial

interaction only nanopore formation occurs, one can use $P_{intact}(t)$ for the estimation of the rate of PGLa-induced nanopore formation in DOPE/DOPG (6/4)-GUVs. Figure 3.3 (h) shows the time course of P_{intact} of the GUVs interacting with 14 μM PGLa. I performed three independent experiments under the same condition ($M = 3$). The mean value and SE of P_{intact}(6 min) was 0.17 ± 0.02. The mean value and SE of the fraction of GUVs experienced local burst of GUVs (P_{LB}(6 min)) and burst of GUVs (P_B(6 min)) after 6 min interaction among all examined GUVs are 0.21 ± 0.03, and 0.10 ± 0.03, respectively.

Next, I investigated the interaction of higher concentration (i.e., 19 μM) of PGLa with DOPE/DOPG (6/4)-GUVs. Fig. 3.5(a)(b) show that the rapid membrane permeation from a GUV began at 153 s and finally the GUV was transformed into lipid aggregates, indicating that GUV burst occurred. Fig. 3.5 (c) shows $I_N(t)$ for several GUVs for 19 μM interaction. After examining 15 single GUVs ($m = 15$), I found that no GUVs were intact within 6 min. In other two independent experiments under the same condition, membrane permeation occurred in all GUVs by 6 min, i.e., P_{intact}(6 min) = 0 ($M = 3$). The mean value with SE of P_{LB}(6 min), and P_B(6 min) were 0.22 ± 0.06, and 0.41 ± 0.11, respectively.

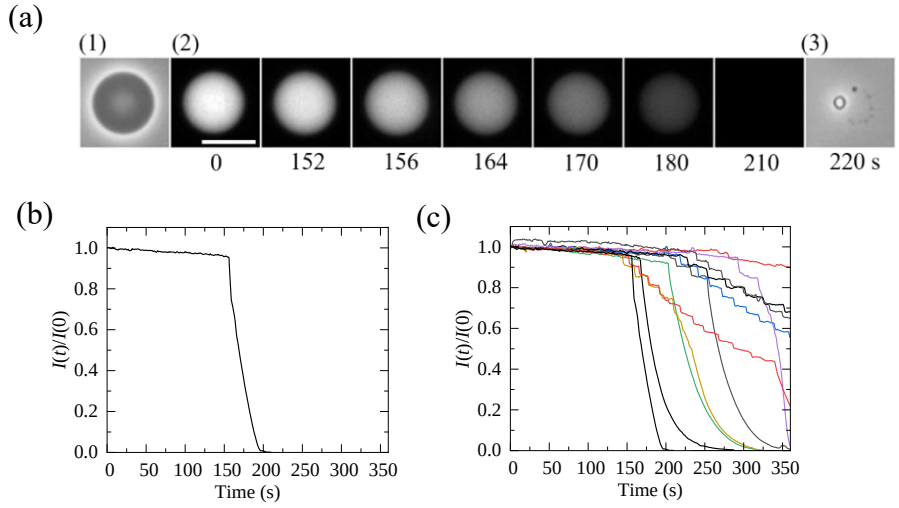

Figure 3.5: 19 μM PGLa-induced membrane permeation of AF488 from a single DOPE/DOPG (6/4)-GUV. (a) Phase contrast (panel 1 and 3) and fluorescence images due to AF488 (panel 2) of the GUV interacting with 19 μM PGLa. Bar, 20 μm. The number below each image indicates the interaction time. (b) Change in $I_N(t)$ of the GUV shown in panel a over time. (c) $I_N(t)$ for many single GUVs in the interaction with 19 μM PGLa.

Finally, I investigated the interaction of lower concentration (i.e., 10 μM) of PGLa with single DOPE/DOPG (6/4)-GUVs. Fig. 3.6 (a) indicates that nanopore formation occurred in a single GUV. Stepwise decrease of fluorescence intensity of this GUV was found (Fig. 3.6(b)). Fig. 3.6(c) indicates that AF488 membrane permeation started after a long-time interaction compared with other PGLa concentration. Thus, P_{intact} (6 min) was 0.50 ± 0.07 (M = 3). The values of P_{LB}(6 min), and P_{B}(6 min) were 0.07 ± 0.04, and 0, respectively.

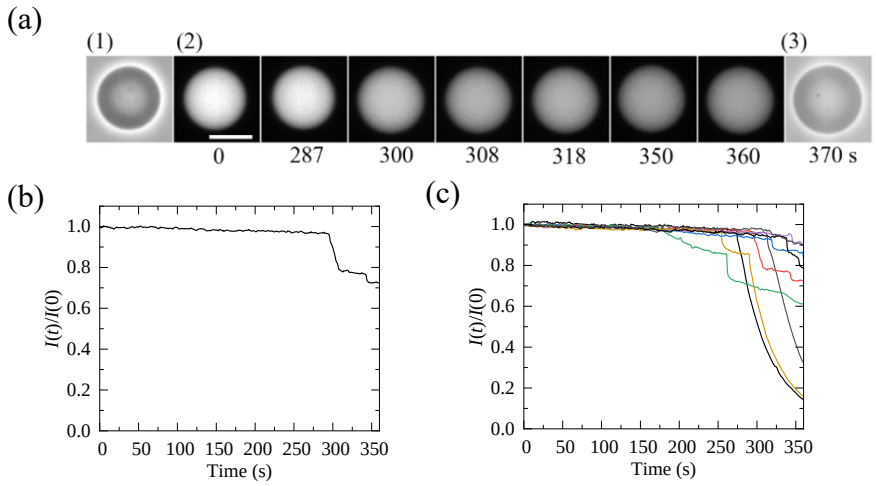

Figure 3.6: 10 μM PGLa-induced membrane permeation of AF488 from a single DOPE/DOPG (6/4)-GUV. (a) Phase contrast (panel (1) and (3)) and fluorescence images due to AF488 (panel (2)) of the GUV interacting with 10 μM PGLa. Bar, 20 μm. The number below each image denoted the interaction time. (b) Change in $I_N(t)$ of the GUV shown in panel a over time. (c) $I_N(t)$ for many single GUVs in the interaction with 10 μM PGLa.

Fig. 3.7(a) shows the time course of P_{intact} for the interaction of 19 (blue □), 14 (▲) and 10 μM (red ○) PGLa. The rate of decrease in P_{intact} increased with an increase in PGLa concentration. As described in Chap. 2, the PGLa-induced pore formation is not the two-state transition from the intact state of a GUV to its pore state, and thus, the rate constant for pore formation, k_p, cannot be obtained. In this case, the fraction of leaking GUVs among all examined ones after the interaction time (t), $P_{leak}(t)$, can be used as a measure of the rate of PGLa-induced nanopore formation. As for a specific interaction time, 300 s was used. The mean values and SEs of P_{leak}(300 s) (M = 3) for 10, 14 and 19

μM PGLa were 0.32 ± 0.02, 0.63 ± 0.06 and 0.98 ± 0.02, respectively (blue ○, Fig. 3.7(b)), indicating that the rate of PGLa-induced nanopore formation is enhanced with an increased PGLa concentration.

The relationship between the fraction of GUVs experienced local burst (P_{LB}, blue □), and burst (P_B, red △) of GUVs among all examined GUVs and PGLa concentration (10, 14 and 19 μM) is shown in Fig. 3.7(c). The fraction of burst GUVs is 0.43 for 19 μM whereas there is no burst event for 10 μM PGLa. This means that probability of burst increases with the increase in PGLa concentration.

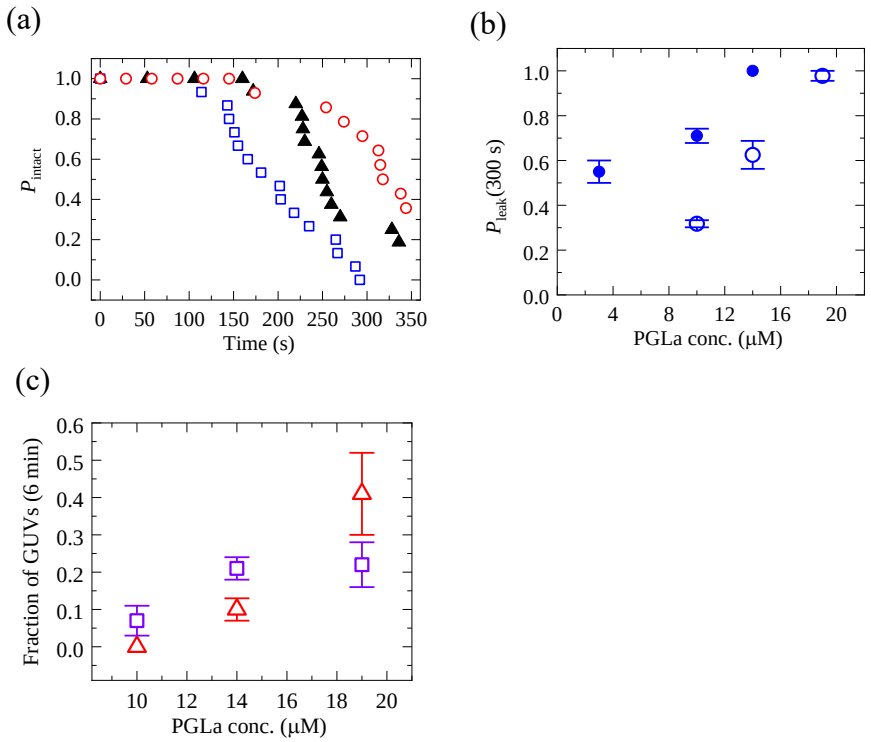

Figure 3.7: Rate of PGLa-induced nanopore formation in DOPE/DOPG (6/4)-GUVs. (a) Time course of change in P_{intact}, (red ○) 10, (▲) 14, and (blue □) 19 μM PGLa. (b) The effect of PE on P_{leak} (300 s). (blue ●) DOPC/DOPG (6/4) and (blue ○) DOPE/DOPG (6/4)-GUVs. (c) The fraction of GUVs experienced local burst (P_{LB}, blue □), and burst (P_B, red △) of GUVs among all examined GUVs for 10, 14 and 19 μM PGLa. Mean values and SEs among 3 independent experiments are shown.

To reveal the effect of the line tension at pre-pore edge on the rate of PGLa-induced pore formation, I compared the $P_{leak}(t)$ values of DOPE/DOPG (6/4)-GUVs with those of DOPC/DOPG (6/4)-GUVs (Fig. 3.7(b)). P_{leak}(300s) values of DOPE/DOPG (6/4)-GUVs were smaller than those of DOPC/DOPG (6/4)-GUVs at the same PGLa concentration, showing that the rate of PGLa-induced nanopore formation in DOPE/DOPG (6/4)-GUVs is smaller, indicating that the line tension at pre-pore edge affects the rate of pore formation.

3.4.2. The location of PGLa in DOPE/DOPG (6/4)-GUVs during their interaction

To elucidate the mechanism underlying the PGLa-induced pore formation in DOPE/DOPG-GUVs, it is indispensable to find the connection between the binding of PGLa in a GUV and membrane permeation of internal contents during PGLa-induced pore formation. Here, I utilized the same method in the section 2.4.2 to examine the PGLa location during the interaction of PGLa with single GUVs.

First, the interaction of 19 μM PGLa/CF-PGLa mixture with single DOPE/DOPG (6/4)-GUVs encapsulating 6 μM AF647 were examined using CLSM. In Fig. 3.8 (a), panel (1) and (2) show the $I_N(t)$ of the GUV due to AF647 and CF-PGLa, respectively. The time course of these intensities are reflected by the blue line in Fig. 3.8 (b) as $I_N(t)$ (left axis) and by the red triangles as $I_{rim}(t)$ (right axis). It was found that $I_N(t)$ did not change until 118 s and then started to decrease gradually, showing that the membrane permeation of AF647 started at 118 s. After the membrane permeation almost completes at 360 s, the spherical GUV with the same diameter remains, indicating that PGLa induces nanopore formation in DOPE/DOPG (6/4)-GUVs. Fig. 3.8 (b) shows a similar two-step increase of $I_{rim}(t)$ observed in DOPC/DOPG-GUVs (see section 2.4.2): the first stable state of $I_{rim}(1^{st})$ was achieved at t = 49 s and remained unchanged until 100 s, and then I_{rim} restarted to increase to reach a second stable state, $I_{rim}(2^{nd})$, within a short time (at 127 s). The starting time of the increase of I_{rim} from $I_{rim}(1^{st})$ (100 s) is a little earlier than the starting time of AF647 membrane permeation (118 s), and $I_{rim}(2^{nd})$ was achieved after AF647 membrane permeation started. I observed the similar phenomena (i.e., the two-step-increase in I_{rim} and its relationship with the onset time of AF647 membrane permeation) in 55 GUVs (m = 55 in M = 3). The average value and SE of the ratio of

$I_{rim}(2^{nd})$ to $I_{rim}(1^{st})$ was 1.8 ± 0.2 (n = 10). Significant stepwise decrease in $I_N(t)$ due to AF647 was not observed in most GUVs, which is different from the results in section 3.4.1.

Next, I investigated the location of PGLa using a lower concentration (10 μM) of CF-PGLa/PGLa to single DOPE/DOPG (6/4)-GUVs (m = 32 in M = 2). When AF647 membrane permeation occurred (in ~50% GUVs among all GUVs), I_{rim} increased in two stepwise (Fig. 3.8 (a)(b)). On the other hand, when the GUVs were kept intact without membrane permeation of AF647 during the observation time, I_{rim} increased in only a

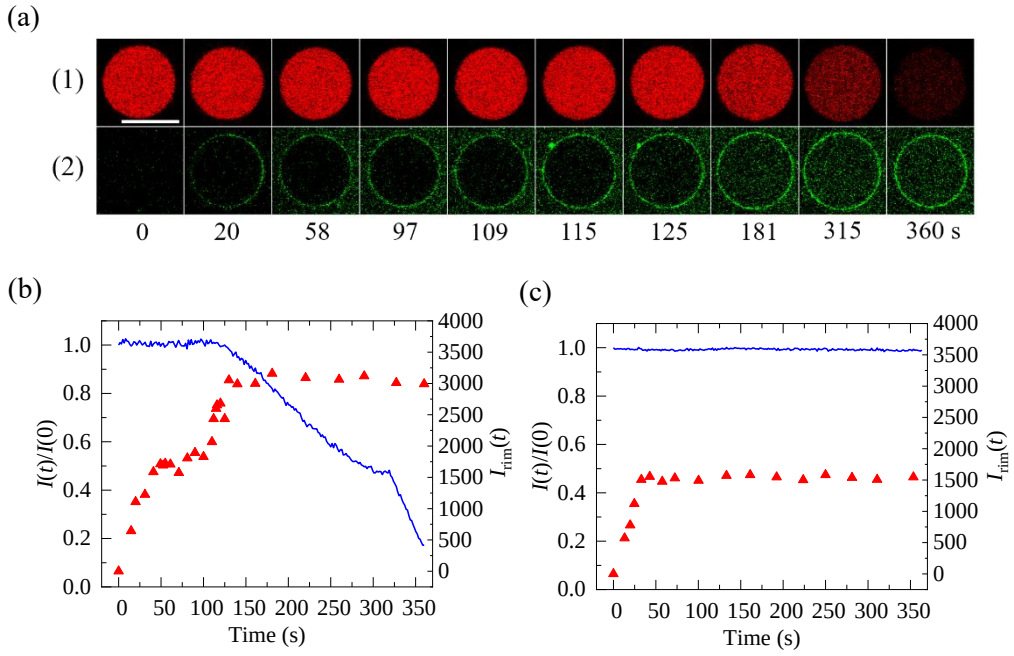

Figure 3.8: Effect of PE on the location of PGLa in a GUV. Interaction of PGLa/CF-PGLa mixture with single GUVs was observed using CLSM. (a) Confocal microscopic images of the interaction of a DOPE/DOPG (6/4)-GUV with 19 μM PGLa/CF-PGLa, due to fluorescence of AF647 (panel 1) and due to fluorescence of CF-PGLa (panel 2). Bar, 20 μm. The interaction time is described below each image. (b) Change of two kinds of fluorescence intensities of the GUV over time. The data correspond to panel a. (c) One step increase in $I_{rim}(t)$ during the interaction of 10 μM PGLa/CF-PGLa with a DOPE/DOPG (6/4)-GUV. In both panel b and c, left axis for blue line ($I_N(t)$ (= $I(t)/I(0)$) of the GUV lumen due to AF647) and right axis for red ▲ ($I_{rim}(t)$ due to CF-PGLa).

stepwise. A typical result of one stepwise increase is shown in Fig. 3.8 (c), where no decrease in $I_N(t)$ was found.

The results that the two-step-increase in I_{rim} occurs only at the start of pore formation indicate that PGLa molecules transfer from the outer to the inner monolayer when pore formation starts. This behavior is different from that of the transfer of PGLa in DOPC/DOPG-GUVs where the PGLa transfer occurs much before the pore formation (Fig. 2.5 in Chap. 2), but is the same as that of the transfer of Mag in DOPC/DOPG-GUVs (Karal et al., 2015a). If one considers that PGLa induces a toroidal pore in the DOPE/DOPG (6/4)-GUV membrane similar to Mag-induced pore, a following scenario can be inferred, which can explain the above results reasonably. At first, a small pore is induced by PGLa in the membrane which does not enable AF647 to permeate. As the pore size increases, first CF-PGLa starts to diffuse from the outer monolayer near the pore to the pore wall, then to that of the inner monolayer, whereas AF647 cannot permeate through the pore because the size of AF647 is large (its R_{SE} is 0.9 nm (Hasan et al., 2018b)). As the pore size increases further, the membrane permeation of AF647 starts. Then, the transfer of CF-PGLa terminates when its concentration in the inner monolayer equals to that in the outer monolayer. Thus, $I_{rim}(2^{nd})/I_{rim}(1^{st})$ ~2 (see the details in section 2.4.2). All of the above results indicate that asymmetric binding of PGLa is responsible for the pore formation in DOPE/DOPG (6/4)-GUVs instead of symmetric binding.

3.4.3. Structural change of DOPE/DOPG (6/4)-GUVs during their interaction with PGLa

As described in section 3.4.1, local burst and burst of DOPE/DOPG (6/4)-GUVs were observed in their interaction with PGLa. To elucidate the mechanism of the GUV burst, it is indispensable to clarify its detailed process. For this purpose, two points are necessary for the experiments. One is the increase in the time-resolution of the observation of a GUV during its interaction with PGLa, and the other is the enhancement of contrast of the GUV membrane to detect its structural changes. Here, a small molar fraction of a fluorescent lipid, NBD-PE, was doped in DOPE/DOPG (6/4)-GUVs (i.e., DOPE/DOPG/NBD-PE (60/39/1)) to increase the contrast of the GUV membrane, and

the structural change of a GUV was observed at a high time-resolution (10 ms) using a high-sensitive fluorescence camera. This method has been successfully used to detect a micropore in a lipid bilayer and its evolution during the interaction of Mag with DOPC/DOPG-GUVs under osmotic pressure (Billah et al., 2022).

First, I describe the structural changes of PGLa-induced local burst of GUVs. The images of a DOPE/DOPG/NBD-PE (60/39/1)-GUV on its interaction with 14 μM PGLa are shown in Fig. 3.9 (a). Panel (1) and (3) represent the phase contrast images before the interaction with PGLa (at $t = 0$) and after the interaction (at $t = 219$ s), respectively. These images show that after the interaction the GUV diameter and the phase contrast of the GUV decreased significantly and several high contrast particles appeared near the membrane and the GUV lumen, which is similar to the images shown in Fig. 3.3 (b) and (c). This result indicates that PGLa induces local burst of the GUV. Panel (2) represents the fluorescence microscopic images of the GUV during the interaction. At the beginning of the interaction (e.g., at 193.09 s), the membrane fluorescence due to NBD-PE shows a homogeneous distribution of intensity across the membrane. Several small and high contrast particles were visible in the GUV membrane at 193.50 s, and their number and brightness increased with time. After 198.10 s, several small vesicles of diameter ~1–2 μm appeared inside the GUV lumen. The time course of the GUV diameter indicates that the diameter of the GUV started to decrease at 197.5 s and then gradually decreased over 16 s (Fig. 3.9 (c)). After starting a decrease in GUV diameter, the number and brightness of high contrast particles and small vesicles increased further. The local burst event of another GUV is shown in Fig. 3.9 (b): similar high contrast particles appeared in the GUV membrane, but their number is smaller than those in Fig. 3.9 (a) and small vesicles appeared whereas their size is larger than those in Fig. 3.9 (b). Fig. 3.9 (d) indicates that the diameter of the GUV started to decrease at 318 s and then gradually decreased over 6 s. 41 GUVs ($m = 41$ in $M = 2$) were examined under this condition, and among them the local burst were found in 13 GUVs, where similar structural changes of GUVs were observed.

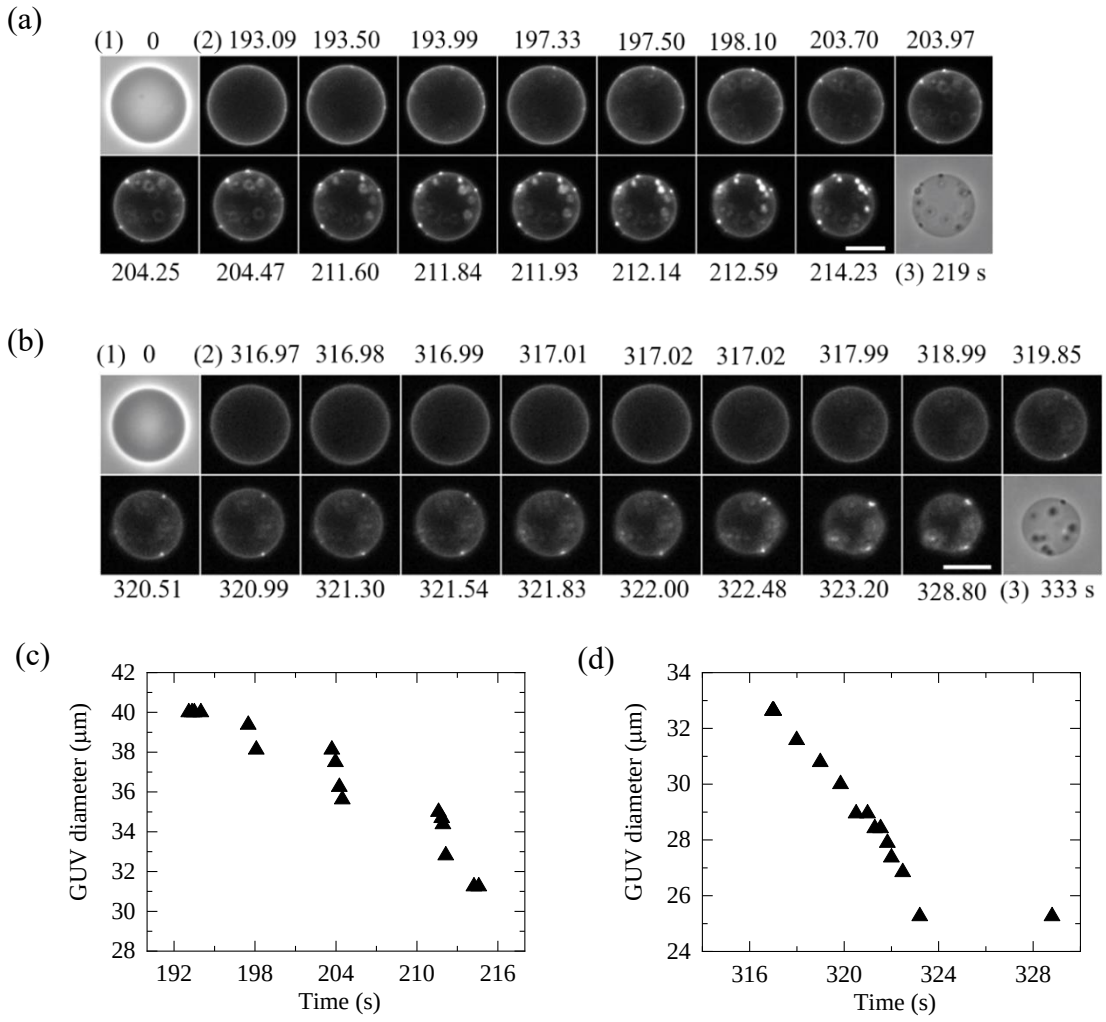

Figure 3.9: Structural change of DOPE/DOPG/NBD-PE (60/39/1)-GUVs during local burst event observed at 10 ms time resolution in the interaction with PGLa. (a) and (b): Microscopic images of local burst of GUVs during their interaction with 14 μM PGLa. Phase contrast (1 and 3) and fluorescence images (2) due to NBD-PE in the membrane are shown. Bar, 20 μm. The interaction time is described above and below each image. Some small, bright particles and smaller vesicles appeared and increased in number eventually in this process. (c) and (d): The change in GUV diameter of (a) and (b), respectively, over time.

Next, I describe the structural changes of PGLa-induced burst of GUVs. The images of a DOPE/DOPG/NBD-PE (60/39/1)-GUV on its interaction with 19 μM PGLa are shown in Fig. 3.10 (a) and (b). Phase contrast images of the GUVs before and after the interaction (panel (1) and (3)) indicate that GUV burst is induced in these two GUVs. Several small and high contrast particles were visible at 265.10 s and 300.87 s in the GUVs in Fig 3.10 (a) and (b), respectively. Fig. 3.10 (c) indicates that the diameter of the GUV (corresponding to Fig. 3.10 (a)) started to decrease at 266.0 s and then rapidly decreased over 1.5 s, and Fig. 3.10 (d) indicates that the diameter of the GUV (corresponding to Fig. 3.10 (b)) started to decrease at 301.4 s and then rapidly decreased over 1.5 s. Then, the number of high contrast particles and apparent small vesicles increased for both GUVs. Finally, the high contrast particles and vesicles aggregated together, resulting in a large-sized bright particle at 270.55 s in (a) and 305.59 s in (b). Burst events were observed in 20 GUVs among 33 GUVs in M = 2, where similar structural changes of GUVs were observed.

Based on these results, I compare the structural change of the GUVs during the GUV burst induced by PGLa with that induced by Mag. In the interaction of Mag with DOPC/DOPG (6/4)-GUVs under osmotic pressure, burst of the GUV occurred where initially a micropore is formed (Billah et al., 2022). The size of the micropore increased within very short time (~100 ms) and during this time high contrast particles appeared at the micropore edge. Finally, the GUV transformed into the aggregate of lipids i.e., burst of the GUV occurred. A similar process in GUV burst was observed in the interaction of Mag with single *E. coli* polar lipid GUVs under isotonic condition, where a micropore turned into lipid membrane aggregates within 50 ms (Billah et al., 2023). In contrast, in the PGLa-induced burst of GUVs, no micropore was formed in the GUV membrane, but instead high contrast particles and apparent small vesicles appeared in the membrane and the GUV lumen concomitantly with rapid decrease in GUV diameter, finally a compact lipid membrane aggregate was formed.

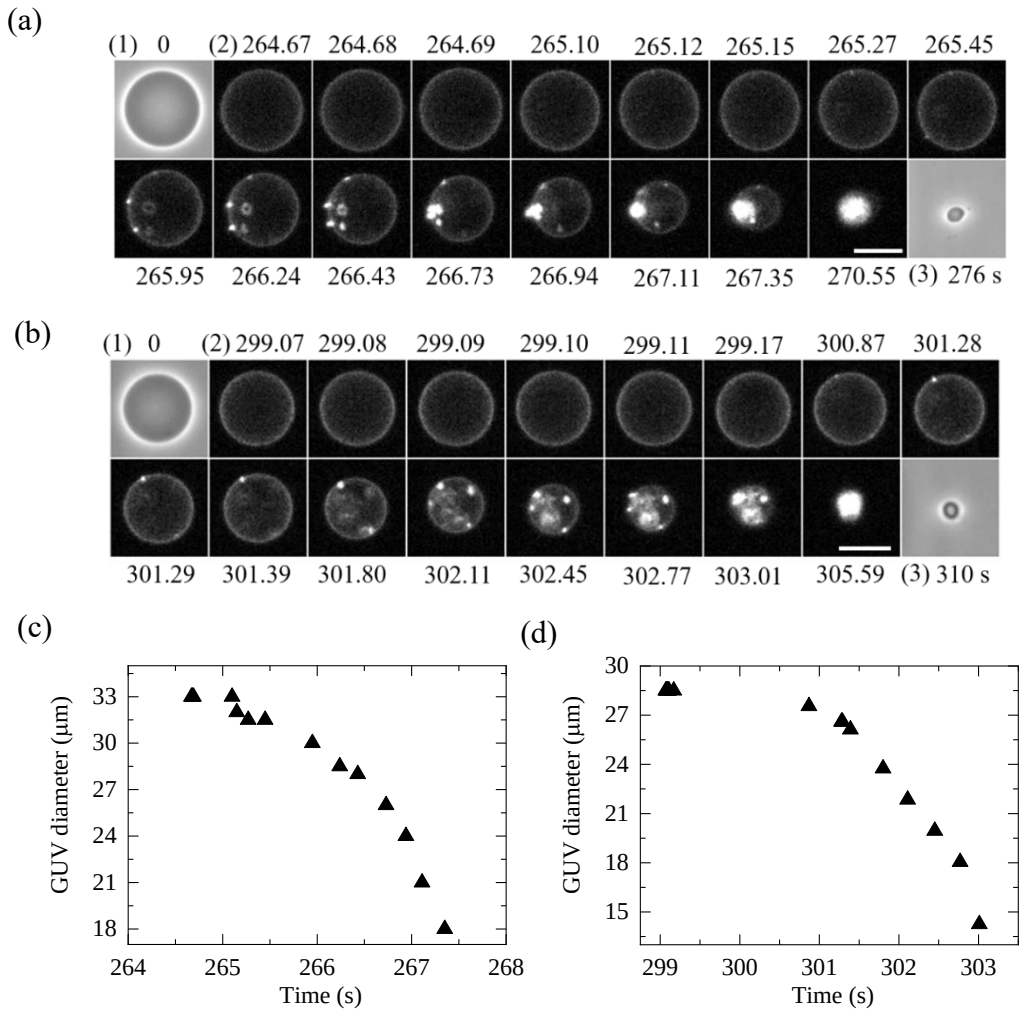

Figure 3.10: Structural change of DOPE/DOPG/NBD-PE (60/39/1)-GUVs during burst event observed at 10 ms time resolution in the interaction with PGLa. Phase contrast (1 and 3) and fluorescence images (2) due to NBD-PE in the membrane are shown. Bar, 20 μm. The interaction time is described above and below each image. (a) and (b) images of burst events experienced by two GUVs induced by 19 μM PGLa. Appearance and increase of small, bright particles with smaller vesicles followed by their association to a large bright spot (a lump of membrane aggregates). (c) and (d) shows change in GUV diameter of (a) and (b), respectively, over time.

3.4.4. Connection between the structural change of DOPE/DOPG (6/4)-GUVs and the AF647 membrane permeation during PGLa-induced GUV burst

The results in the previous section show the structural change of DOPE/DOPG (6/4)-GUVs during the PGLa-induced local burst and burst events. However, the connection between the structural changes of the GUVs and the membrane permeation of fluorescent probes is unclear, because the experiments of the structural changes of the GUVs cannot provide the information of the change in membrane permeation. One may consider several scenarios. For example, the structural change may induce the membrane permeation, instead of nanopores in the membrane. To elucidate this connection, I reanalyzed the results obtained using CLSM (e.g., Fig. 3.8) from a different point of view. Fig. 3.8 shows only the case of nanopore formation (i.e., membrane permeation of fluorescent probe without changing the GUV diameter. However, some GUVs exhibit the local burst and burst.

First, I consider the case of 19 μM PGLa/CF-PGLa-induced local burst of GUVs. Fig. 3.11 (a) (1) and (c) show that the AF647 membrane permeation starts at 60 s. On the other hand, Fig. 3.11 (a)(2) shows the CLSM images of the same GUV due to CF-PGLa, indicating that high contrast particles appeared at 214 s and their number and contrast increased with time and the GUV diameter started to decrease at 299 s, although the CLSM image of a GUV provides only a rough estimation of change in GUV diameter. At that time, the membrane permeation almost completed (I_N (t) ≈ 0.10). 4 events of GUV local burst were examined under this condition, and the same connection between the structural changes of the GUVs and the membrane permeation of AF647 were observed in 4 GUVs local burst.

A similar connection can be found in the case of GUV burst. Fig. 3.11 (b)(1) and (d) show that the membrane permeation of AF647 starts at 70 s. On the other hand, Fig.3.11 (b)(2) indicates that high contrast particles appeared at 192 s, whose number and contrast increased with time, and the GUV diameter started to decrease at 192 s, when the membrane permeation almost completed (I_N (t) ≈ 0.03), and then the GUV is converted into membrane aggregates at 289 s. 18 events of GUV burst were examined under this condition, and the same connection between the structural changes of the GUVs and the AF647 membrane permeation were observed in 18 GUVs burst.

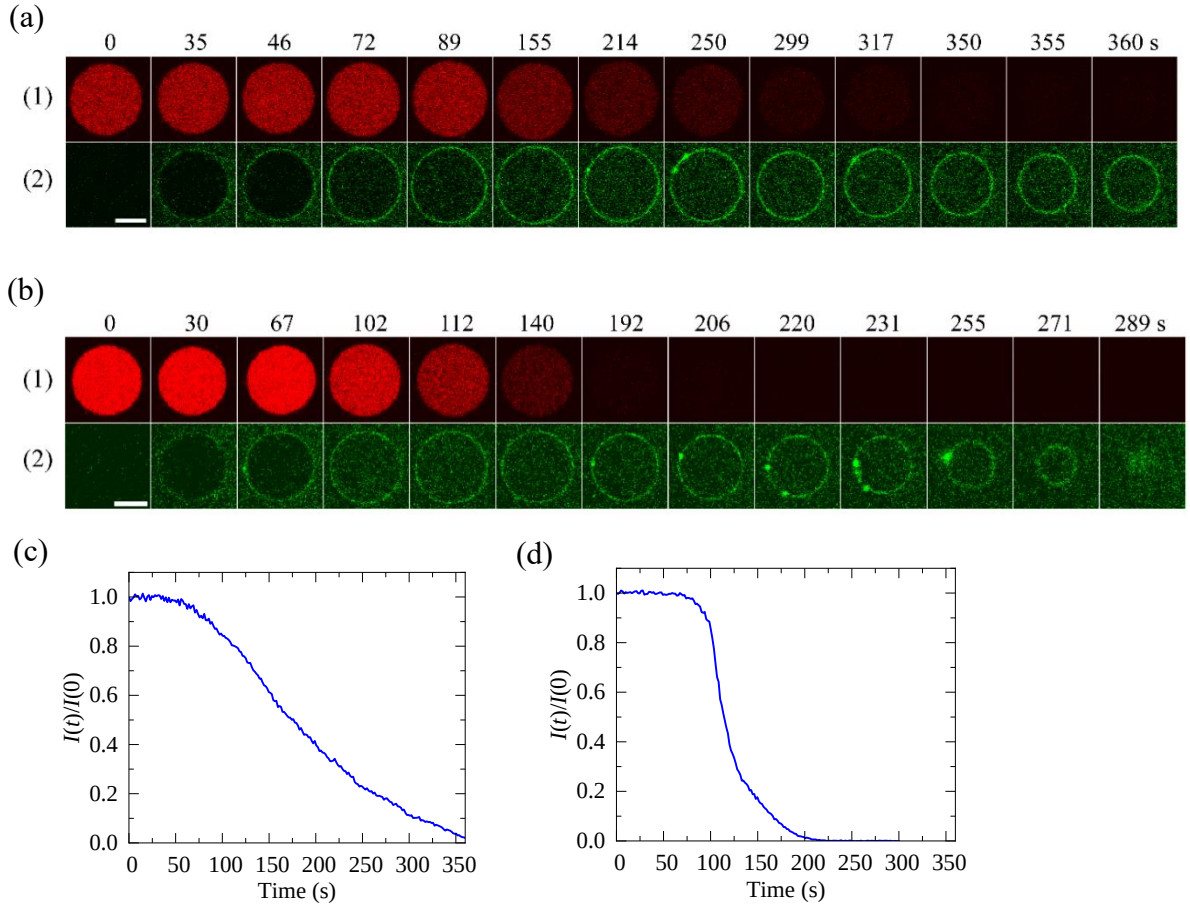

Figure 3.11: Structural change of DOPE/DOPG (6/4)-GUVs and the membrane permeation of AF647 during local burst and burst in the interaction with PGLa. (a) Local burst (b) burst of two ingle DOPE/DOPG (6/4)-GUVs in the interaction with 19 µM PGLa/CF-PGLa; CLSM images due to fluorescence of AF647 (panel 1) and due to fluorescence of CF-PGLa (panel 2) are shown. Bar, 10 µm. The interaction time is described above each image. (c) and (d) $I_N(t)$ (= $I(t)/I(0)$) of the GUVs in (a) and (b), respectively.

These results show that in the PGLa-induced local burst and burst of GUVs, first membrane permeation of AF647 starts, and after an extended time, high contrast particles started to appear and their number and contrast increases with time, finally the GUV diameter started to decrease when the AF647 membrane permeation almost completed.

This common connection indicates that initially nanopores in the bilayer are induced by PGLa, which remains stable for a long interval, and then high contrast particles appear in the GUV membrane, which may induce instability of the GUV, resulting in the reduction of GUV diameter. Therefore, it can be inferred that the origin of the local burst and burst events is the nanopore formation in GUV bilayer.

3.5. General discussion

From the results of the AF488 membrane permeation from DOPE/DOPG (6/4)-GUVs during the 6 min interaction (Fig. 3.3), I found three apparently different events: nanopore formation (membrane permeation without change in GUV diameter), local burst (membrane permeation concomitant with significant decrease in GUV diameter) and burst of the GUVs (membrane permeation concomitant with the conversion of GUVs into lipid aggregates). Generally, the word "GUV burst" includes both phenomenon (i.e., local burst and burst of GUVs) because for both cases membrane permeation occurs concomitantly with the decrease in GUV diameter and only the difference of the degree in the decrement of GUV diameter (Billah et al., 2024). Hereafter, I use "GUV burst" for two phenomena in most cases. In some GUVs, nanopore formation occurred after 6 min interaction, but after a prolonged interaction GUV burst occurred (Fig. 3.4). To reveal the process of GUV burst, the structural changes of the GUVs interacting PGLa were observed at high time-resolution by doping fluorescent lipids (Fig. 3.9 and 3.10). The results indicate that high contrast particles and apparent lipid vesicles with a diameter of ~1–2 μm were observed in the GUVs, then the GUV diameter started to decrease, resulting in GUV burst. The results of the simultaneous CLSM measurement of the location of PGLa and AF647 membrane permeation during the interaction of PGLa indicate that first AF647 membrane permeation starts, and after an extended time, high contrast particles started to appear in the GUV and their number and contrast increases with time, followed by the decrease in the GUV diameter, resulting in GUV burst (Fig. 3.11). These results indicate that PGLa-induced GUV burst originate from the nanopore formation. Thus, it can be concluded that the P_{leak} values are determined by PGLa-induced nanopore formation in lipid bilayers. The results show that P_{leak} of DOPE/DOPG-GUVs had lower values than that of DOPC/DOPG-GUVs at the same PGLa concentration (Fig.

3.7), indicating that the rate of PGLa-induced nanopore formation in DOPE/DOPG-GUVs was lower than that in DOPC/DOPG-GUVs.

The simultaneous CLSM measurement also indicate that PGLa locates only in the outer monolayer of DOPE/DOPG-GUVs just before AF647 membrane permeation (Fig. 3.8). This kind of binding of peptide is called asymmetric (Levadnyy et al., 2019). Thus, the asymmetric binding of PGLa is responsible for nanopore formation in DOPE/DOPG (6/4)-GUVs. Such kind of behavior is similar to the Mag-induced pore formation reported previously (Karal et al., 2015a), but is different from PGLa-induced nanopore formation in DOPC/DOPG (6/4)-GUVs, where the symmetric binding induces nanopore formation (see Chap. 2). As described in section 2.4.2, PGLa transfers across a DOPC/DOPG (6/4) bilayer without pore formation. Its mechanism is explained by the pre-pore model. Based on the free energy profile of a pre-pore, as the slope of the curve of Ω vs. r_p less than ~10 k_BT increases, the rate of pre-pore formation and the size of a pre-pore decreases (section 2.5). Two curves in Fig. 3.12 are drawn based on Eq. (2.24) using Γ = 15.6 pN for DOPE/DOPG bilayer and Γ = 10.7 pN for DOPC/DOPG bilayer in the case of a membrane tension of 3.0 mN m^{-1}. It is clear that the slope of the curve of Ω vs. r_p for DOPE/DOPG bilayer is larger than that for DOPC/DOPG bilayer. This result indicates that the great increase in Γ for DOPE/DOPG bilayer diminishes the frequency of the pre-pore formation and its size. This may be the reason why PGLa cannot transfer from the outer to the inner monolayer without pore formation. However, high concentrations of PGLa can induce nanopore formation, which induces a transfer of PGLa into the inner monolayer. For this reason, the rate of PGLa-induced nanopore formation in DOPE/DOPG-GUVs is lower than that in DOPC/DOPG-GUVs for a same PGLa concentration. In Fig. 3.12, as membrane tension value, 3.0 mN m^{-1} was used as a tentative one, but if the value of membrane tension is changed, the main point of the above conclusion does not change. The binding of AMPs such as Mag induces stretching of the lipid bilayer, inducing membrane tension (Karal et al., 2015a), and binding of PGLa also increases the fractional area of the DOPC/DOPG bilayer (Parvez et al., 2018). However, its membrane tension cannot be determined accurately because the elastic modulus of DOPC/DOPG bilayer bound with PGLa is unknown due to the orientation of PGLa (i.e., T state).

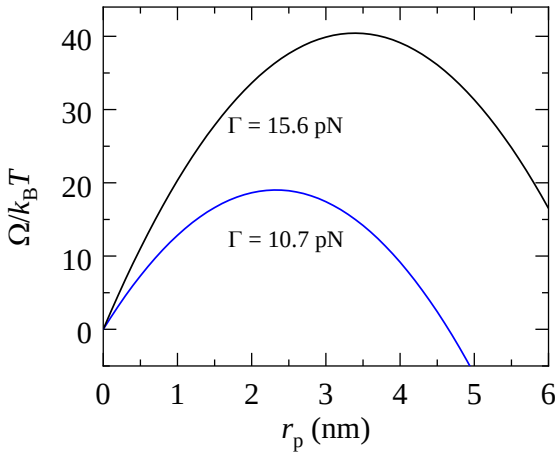

Figure 3.12: Relationship between Ω with different line tensions (Γ). Blue line: DOPC/DOPG (6/4)-GUVs (Γ = 10.7 pN) and black line: DOPE/DOPG (6/4)-GUVs (Γ = 15.6 pN) (Tazawa and Yamazaki, 2023). σ = 3 mN m^{-1} is used here.

A similar phenomenon was reported for a CPP, transportan 10 (TP10) (Islam et al., 2017). TP10 can transfer across DOPC/DOPG bilayer without pore formation at their low concentrations (Islam et al., 2014; Moghal et al., 2020). However, the presence of high concentrations of cholesterol inhibits the transfer of TP10, whereas high concentration of TP10 induces pore formation in the GUVs containing the same concentration of cholesterol, through which TP10 transfers into the inner monolayer (Islam et al., 2017). Since it was reported that the line tension of a micropore edge in DOPC-GUV increases with increasing mole fraction of cholesterol (Karatekin et al., 2003), it is expected that the line tension of a pre-pore in DOPC/DOPG bilayer has a large value in the presence of high concentration of cholesterol. This inference can reasonably explain the inhibition of transfer of TP10 across the bilayer.

The results of AF488 membrane permeation from DOPE/DOPG (6/4)-GUVs using FLM (Fig. 3.3) show discontinuous decrease in $I_N(t)$ where several stepwise decreases occur. This is in contrast with the almost continuous decrease in $I_N(t)$ in DOPC/DOPG (6/4)-GUVs (Fig. 2.1). This discontinuous decrease in $I_N(t)$ indicates the discontinuous AF488 membrane permeation. On the other hand, this stepwise decrease was not observed using CLSM (Fig. 3.8), probably due to the following reason. In the CLSM

measurement, only a cross-section was observed. If pore formation occurs in this cross-section and the pore continues to exist there, the stepwise decrease may be observed. However, this probability is low. Some possible factors can be considered behind this discontinuous membrane permeation. The first factor is the decrease in GUV diameter during the GUV burst. This GUV diameter decrease must involve local structural changes of the GUV membrane such as membrane folding, which may induce discontinuous membrane permeation. However, the decrease in GUV diameter starts after the membrane permeation almost finishes, whereas the phenomena of the stepwise decrease in $I_N(t)$ are always observed at the initial stage of membrane permeation (Fig. 3.3 and 3.4). Therefore, the first factor is implausible. The second factor is the appearance of high contrast particles. Currently, the mechanism of the formation of these particles is unknown, but small aggregation of membranes induced by their interaction with PGLa is involved. It is reasonable to consider that such particle formation induces instability of the local site of the GUV membrane, resulting in a short time membrane permeation. The production of small aggregation may occur discontinuously, and thus, the stepwise membrane permeation may be induced. The results obtained by the simultaneous measurement using CLSM (Fig. 3.11) indicate that membrane permeation of AF647 starts, and after an extended time, high contrast particles started to appear and their number and contrast increases with time. Since the phenomena of the step-wise decrease in $I_N(t)$ are always observed at the initial stage of membrane permeation. Therefore, the second factor is also implausible. The third factor is the opening and closing of a nanopore, which clearly explains the stepwise membrane permeation. It is well known that most ion channels exhibit the opening and the closing due to thermal fluctuation. However, there has been no report on the opening and the closing of AMPs-induced nanopores: these nanopores are always open. Thus, it is important to find the cause of the closing of a nanopore. It is reasonably considered that the value of the line tension at the edge of a nanopore is the same as that at the pre-pore edge because the diameter of a nanopore is the same order as that of a pre-pore. Therefore, the line tension of a nanopore edge in DOPE/DOPG (6/4) bilayer is 15.6 pN, which is much larger than that in DOPC/DOPG (6/4) bilayer (10.7 pN). The presence of peptides in the wall of a nanopore may decrease the line tension, but it may still have a large value. Based on a similar discussion in section 2.5, large line

tension tends to close the nanopore rapidly. Currently, I consider that third factor is most plausible. However, to verify this hypothesis, more experimental evidence is indispensable.

The appearance of the high contrast particles and apparent lipid vesicles after the PGLa-induced nanopore formation is a special characteristic for DOPE/DOPG (6/4)-GUVs, which is not observed in DOPC/DOPC (6/4)-GUVs. Based on the resolution of optical microscopy, it is not clear that these apparent lipid vesicles are free lipid vesicles inside the GUV lumen or the invaginated structure attached with the mother GUV membrane. It is inferred that these high contrast particles are composed of lipid bilayers and PGLa, and are formed due to the electrostatic interaction between the positively charged PGLa-bound lipid bilayer and negatively charged PGLa-free lipid bilayer. This attractive force is demonstrated by the association between the high contrast particles (resulting in larger particles) (Fig. 3.10 (a)(b)). The mechanisms underlying the formation of the high contrast particles and apparent lipid vesicles are unknown currently, but the negative spontaneous curvature of DOPE ($H_0 = -0.36$ nm^{-1}) may play an important role in their formation. It is well established that the electrostatic interaction due to the surface charges of lipid bilayers controls the monolayer spontaneous curvature (Awad et al., 2005; Li et al., 2001). Due to the presence of negatively charged DOPG, the H_0 of DOPE/DOPG (6/4) monolayer is -0.22 nm^{-1}, whose absolute value is smaller than that of DOPE. However, the binding of PGLa decreases the surface charge density of DOPE/DOPG (6/4) monolayer, resulting in an increase of negative curvature. If the bending of the lipid bilayer occurs in a GUV, membrane folding may occur near a nanopore by the same way as in a micropore, which was observed in the case of Mag (Fig. 1.3) (Billah et al., 2022, 2023). This change in spontaneous curvature may also induce invagination of the GUV membrane at a local site, which may be related to the production of apparent lipid vesicles.

It is reasonably considered that production of these high contrast particles and apparent small vesicles diminishes the membrane area of a GUV. If the GUV volume remains constant, the reduction of the membrane area stretches the GUV membrane, inducing positive membrane tension (i.e., $\sigma > 0$). If the invaginated structure appears toward the GUV lumen or free vesicles are generated in the GUV lumen, the GUV volume

would increase, which enhance the membrane tension more. As described in chapter 1, in the case of the interaction of Mag with DOPC/DOPG-GUVs, this membrane tension transforms a nanopore to a micropore (Billah et al., 2022). No micropore formation in the interaction of PGLa with DOPE/DOPG (6/4)-GUVs may be explained by the large Γ at the edge of nanopore. Instead, this positive membrane tension may induce a large efflux of internal solution across the nanopore to decrease the area of the GUV membrane and its elastic energy. As a result, the volume of the GUV may decrease concomitantly with production of high contrast particles and apparent lipid vesicles. This can reasonably explain the results that the rate of decrease in GUV volume is higher for 19 μM PGLa than for 10 and 14 μM (Fig. 3.9 and 3.10), because the number of the high contrast particle and smaller vesicle formation is larger in higher PGLa concentration, inducing higher membrane tension. However, the above hypotheses on mechanisms underlying the formation of high contrast particles and apparent lipid vesicles, and concomitant decrease in GUV volume should be examined by further experiments and theories.

In most AMPs/AMCs-induced GUV burst, a micropore is formed in a GUV membrane as an intermediate stage (Billah et al., 2024). The study on Mag-induced GUV burst under membrane tension indicates that a micropore is formed as a result of the evolution of a nanopore (Billah et al., 2022). The results in this chapter demonstrate that in the PGLa-induced burst of DOPE/DOPG-GUVs, the GUV diameter decreases without formation of a micropore, which is a new type of process of AMPs/AMCs-induced GUV burst.

3.6. Conclusion

One of the largest differences of PGLa-induced nanopore formation in DOPE/DOPG (6/4)-GUVs from that in DOPC/DOPG (6/4)-GUVs is that the asymmetric binding of PGLa induces the nanopore formation in DOPE/DOPG (6/4)-GUVs. This result indicates that the transfer of PGLa across the lipid bilayer without pore formation is suppressed in the DOPE/DOPG (6/4) bilayer, probably due to the larger line tension at the pre-pore edge (Γ). This suppression can be reasonably explained using the free energy of a pre-pore. As a result, the rate of PGLa-induced nanopore formation in the DOPE/DOPG (6/4) bilayer is lower than that in the DOPC/DOPG (6/4) bilayer. During the nanopore formation,

stepwise decrease in $I_N(t)$ of several GUVs is observed, which may indicate pore opening and subsequent closure. However, its mechanism is not totally clear currently, and thus, further study is indispensable. After PGLa-induced nanopore formation in DOPE/DOPG (6/4)-GUVs, high contrast particles and smaller vesicles are produced in the GUV membrane and lumen, which decreases the GUV diameter gradually, resulting in local burst and burst of the GUVs. This is also one of the largest differences of the interaction of PGLa with DOPE/DOPG (6/4)-GUVs from that in DOPC/DOPG (6/4)-GUVs. In addition, PGLa does not evolve any micropores during GUV burst and local burst unlike the Mag interaction with *E. coli* polar lipids (Billah et al, 2023), which may be related to the high Γ in DOPE/DOPG (6/4) bilayer. The formation of high contrast particles and smaller vesicles may be induced by the negative spontaneous curvature of DOPE/DOPG (6/4) monolayer, but their processes and mechanism have not been revealed, and hence, future investigations are necessary.

CHAPTER FOUR

General Conclusion

It is well recognized that some AMPs target the lipid bilayer region in plasma membrane and AMPs-induced cell membrane damage induces bacterial cell death. Thus, it is indispensable to elucidate the effect of physical properties of lipid bilayers on the pore formation. In this thesis, I investigated the effect of membrane tension (σ) and line tension at pre-pore edge (Γ) on the interaction of PGLa with lipid bilayers.

In chapter 2, using the Π method, I succeeded in revealing the effect of σ on the PGLa-induced nanopore formation in DOPC/DOPG (6/4)-GUVs and its evolution. The rate of PGLa-induced nanopore formation estimated by the fraction of leaking GUVs (P_{leak}) increases with increasing σ, and the nanopore does not grow to a micropore nor GUV burst. One of the causes underlying this result is that the σ-enhanced rate of PGLa transfer across the bilayer without nanopore formation since the PGLa-induced nanopore formation in these GUVs requires the symmetric binding of PGLa across the GUV membrane. As the mechanism of the PGLa transfer, I considered a pre-pore model: PGLa transfers from the outer to the inner monolayer via diffusion along the wall of a pre-pore in the bilayer produced by thermal force. The free energy of a pre-pore decreases with increasing σ, resulting in the increment of the pre-pore radius and the rate of pre-pore formation. Thus, membrane tension enhances the rate of PGLa transfer. Another process (the pore formation from the symmetric binding of PGLa) is also important in the PGLa-induced nanopore formation. However, currently its detailed process and mechanism are unknown, and thus, further studies on this process are required.

It is valuable to compare the effect of σ on PGLa with that on Mag. The rate constant of Mag-induced nanopore formation ($k_{\mathrm{p}}^{\mathrm{Mag}}$) increases with increasing σ (Billah et al., 2022), which is the same as that for PGLa. However, its cause is different from that for PGLa. In the case of Mag, the asymmetric binding of peptides across the bilayer increases the membrane tension of the inner monolayer, which triggers a nanopore formation in the bilayer (the stretch-activated model: Karal et al., 2015a). The presence of membrane tension due to Π increases the total tension in the inner monolayer, which enhances the $k_{\mathrm{p}}^{\mathrm{Mag}}$. On the other hand, membrane tension converts a Mag-induced nanopore to a micropore, and finally GUV burst. Mag induces a toroidal nanopore, where no strong interaction between the peptides in the pore, and thus, the pore radius can change easily. Therefore, membrane tension can increase the radius of Mag-induced nanopore, resulting

in a micropore, whose radius further increases until σ vanishes, and subsequently the GUV bursts due to another reasons (Billah et al, 2022). The different characteristics of the effect of σ on PGLa-induced nanopore formation from that for Mag suggest that PGLa-induced nanopore has a different structure from the toroidal pore. This inference is also supported by the result of the time course of membrane permeability coefficient. However, the structure of PGLa-induced nanopore and the mechanism underlying its formation have not been revealed yet, and hence, further studies are necessary.

In chapter 3, I elucidate the effect of Γ on the PGLa-induced nanopore formation by examining the interaction of PGLa with DOPE/DOPG (6/4)-GUVs, which possess higher Γ than DOPC/DOPG (6/4)-GUVs. The results of the PGLa-induced membrane permeation of fluorescent probes from single GUVs indicate that PGLa induced apparently three events: nanopore formation, local burst and burst of GUVs. The observation of pore formation at 10 ms exposure time as well as the CLSM observation revealed that local burst and burst events have the same origin, i.e., the nanopore formation. The rate of PGLa-induced nanopore formation in DOPE/DOPG (6/4)-GUVs is lower than that in DOPC/DOPG (6/4)-GUVs. Moreover, the asymmetric binding of PGLa across the GUV membrane is retained before nanopore formation, indicating that PGLa transfer across the bilayer without nanopore formation is inhibited, which is one of main causes of the lower rate of nanopore formation. Thus, the mode of PGLa-induced nanopore formation in DOPE/DOPG (6/4)-GUVs is similar to Mag-induced nanopore formation. As the Γ increases, the free energy of a pre-pore increases, resulting in the decrement of the pre-pore radius and the rate of pre-pore formation. Thus, higher Γ attenuates the rate of transfer of PGLa across the lipid bilayer. After the nanopore formation, high contrast particles and apparent lipid vesicles appear in the GUV membrane and lumen, which may induce continuous decrease in GUV diameter, resulting in GUV burst and local burst. This is a new type of GUV burst induced by AMPs and antimicrobial substances. The high Γ and large negative spontaneous curvature of the monolayer may be related to these structural changes of the GUVs. However, currently there is no experimental evidence in the formation mechanism of the high particles and vesicles during GUV burst and local burst, and hence, its further investigation is required.

The results in this thesis clearly revealed that the physical properties of lipid bilayers such as membrane tension and line tension at pre-pore edge greatly affect the rate and the mechanism of PGLa-induced nanopore formation and the evolution of the nanopore. These data are valuable to elucidate the mechanism underlying the membrane damage induced by PGLa and other AMPs.

References

Ahmed, M., Billah, M.M., Tamba, Y., Yamazaki, M., 2024a. Estimation of negative membrane tension in lipid bilayers and its effect on antimicrobial peptide magainin 2-induced pore formation. J Chem Phys 160, 011101.

Ahmed, M., Islam, M.Z., Billah, M.M., Yamazaki, M., 2024b. Effect of membrane tension on antimicrobial peptide PGLa-induced pore formation in lipid bilayers. Biochem. Biophys. Res. Commun. 695, 149452.

Akimov, S.A., Volynsky, P.E., Galimzyanov, T.R., Kuzmin, P.I., Pavlov, K.V., Batishchev, O.V., 2017. Pore formation in lipid membrane I: Continuous reversible trajectory from intact bilayer through hydrophobic defect to transversal pore. Sci Rep 7, 12152.

Alam, J.M., Kobayashi, T., Yamazaki, M., 2012. The Single-Giant Unilamellar Vesicle Method Reveals Lysenin-Induced Pore Formation in Lipid Membranes Containing Sphingomyelin. Biochemistry 51, 5160–5172.

Ali, M.H., Shuma, M.L., Dohra, H., Yamazaki, M., 2021. Translocation of the nonlabeled antimicrobial peptide PGLa across lipid bilayers and its entry into vesicle lumens without pore formation. Biochimica et Biophysica Acta (BBA)−Biomembranes 1863, 183680.

Alley, S.H., Ces, O., Barahona, M., Templer, R.H., 2008. X-ray diffraction measurement of the monolayer spontaneous curvature of dioleoylphosphatidylglycerol. Chemistry and Physics of Lipids 154, 64–67.

Anishkin, A., Loukin, S.H., Teng, J., Kung, C., 2014. Feeling the hidden mechanical forces in lipid bilayer is an original sense. Proceedings of the National Academy of Sciences 111, 7898–7905.

Awad, T.S., Okamoto, Y., Masum, S.M., Yamazaki, M., 2005. Formation of Cubic Phases from Large Unilamellar Vesicles of Dioleoylphosphatidylglycerol/Monoolein Membranes Induced by Low Concentrations of Ca2+. Langmuir 21, 11556–11561.

Ayala, Y.A., Omidvar, R., Römer, W., Rohrbach, A., 2023. Thermal fluctuations of the lipid membrane determine particle uptake into Giant Unilamellar Vesicles. Nat Commun 14, 65.

Baumgart, T., Hess, S.T., Webb, W.W., 2003. Imaging coexisting fluid domains in biomembrane models coupling curvature and line tension. Nature 425, 821–824.

Bechinger, B., Zasloff, M., Opella, S.J., 1998. Structure and Dynamics of the Antibiotic Peptide PGLa in Membranes by Solution and Solid-State Nuclear Magnetic Resonance Spectroscopy. Biophysical Journal 74, 981–987.

Bechinger, B., Zasloff, M., Opella, S.J., 1993. Structure and orientation of the antibiotic peptide magainin in membranes by solid-state nuclear magnetic resonance spectroscopy. Protein Science 2, 2077–2084.

Billah, M.M., Ahmed, M., Islam, M.Z., Yamazaki, M., 2024. Processes and mechanisms underlying burst of giant unilamellar vesicles induced by antimicrobial peptides and compounds. Biochimica et Biophysica Acta (BBA) - Biomembranes 184330.

Billah, M.M., Or Rashid, M.M., Ahmed, M., Yamazaki, M., 2023. Antimicrobial peptide magainin 2-induced rupture of single giant unilamellar vesicles comprising *E. coli* polar lipids. Biochimica et Biophysica Acta (BBA) - Biomembranes 1865, 184112.

Billah, M.M., Saha, S.K., Rashid, M.M.O., Hossain, F., Yamazaki, M., 2022. Effect of osmotic pressure on pore formation in lipid bilayers by the antimicrobial peptide magainin 2. Phys. Chem. Chem. Phys. 24, 6716–6731.

Blazyk, J., Wiegand, R., Klein, J., Hammer, J., Epand, R.M., Epand, R.F., Maloy, W.L., Kari, U.P., 2001. A Novel Linear Amphipathic β-Sheet Cationic Antimicrobial Peptide with Enhanced Selectivity for Bacterial Lipids*. Journal of Biological Chemistry 276, 27899–27906.

Bobone, S., Stella, L., 2019. Selectivity of Antimicrobial Peptides: A Complex Interplay of Multiple Equilibria, in: Matsuzaki, K. (Ed.), Antimicrobial Peptides: Basics for Clinical Application. Springer, Singapore, pp. 175–214.

Boggs, J.M., Jo, E., Polozov, I.V., Epand, R.F., Anantharamaiah, G.M., Blazyk, J., Epand, R.M., 2001. Effect of magainin, class L, and class A amphipathic peptides on fatty acid spin labels in lipid bilayers. Biochimica et Biophysica Acta (BBA) - Biomembranes 1511, 28–41.

Brochard-Wyart, F., de Gennes, P.G., Sandre, O., 2000. Transient pores in stretched vesicles: role of leak-out. Physica A: Statistical Mechanics and its Applications 278, 32–51.

Brogden, K.A., 2005. Antimicrobial peptides: pore formers or metabolic inhibitors in bacteria? Nat Rev Microbiol 3, 238–250.

Dai, J., Sheetz, M.P., 1999. Membrane Tether Formation from Blebbing Cells. Biophysical Journal 77, 3363–3370.

De Gennes, P.-G., Brochard-Wyart, F., Quéré, D., 2004. Capillarity and Wetting Phenomena. Springer, New York, NY.

Eibl, H., Woolley, P., 1979. Electrostatic interactions at charged lipid membranes. Hydrogen bonds in lipid membrane surfaces. Biophysical Chemistry 10, 261–271.

Evans, E., Heinrich, V., Ludwig, F., Rawicz, W., 2003. Dynamic Tension Spectroscopy and Strength of Biomembranes. Biophysical Journal 85, 2342–2350.

Evans, E., Rawicz, W., 1990. Entropy-driven tension and bending elasticity in condensed-fluid membranes. Phys. Rev. Lett. 64, 2094–2097.

Evans, E., Smith, B.A., 2011. Kinetics of hole nucleation in biomembrane rupture. New J. Phys. 13, 095010.

Evans, E.A., Waugh, R., Melnik, L., 1976. Elastic area compressibility modulus of red cell membrane. Biophysical Journal 16, 585–595.

Fuertes, G., Giménez, D., Esteban-Martín, S., Sánchez-Muñoz, O.L., Salgado, J., 2011. A lipocentric view of peptide-induced pores. Eur Biophys J 40, 399–415.

Glaser, R.W., Leikin, S.L., Chernomordik, L.V., Pastushenko, V.F., Sokirko, A.I., 1988. Reversible electrical breakdown of lipid bilayers: formation and evolution of pores. Biochimica et Biophysica Acta (BBA) - Biomembranes 940, 275–287.

Glaser, R.W., Sachse, C., Dürr, U.H.N., Wadhwani, P., Afonin, S., Strandberg, E., Ulrich, A.S., 2005. Concentration-Dependent Realignment of the Antimicrobial Peptide PGLa in Lipid Membranes Observed by Solid-State 19F-NMR. Biophysical Journal 88, 3392–3397.

González-Bermúdez, B., Guinea, G.V., Plaza, G.R., 2019. Advances in Micropipette Aspiration: Applications in Cell Biomechanics, Models, and Extended Studies. Biophysical Journal 116, 587–594.

Gregory, S.M., Pokorny, A., Almeida, P.F.F., 2009. Magainin 2 Revisited: A Test of the Quantitative Model for the All-or-None Permeabilization of Phospholipid Vesicles. Biophysical Journal 96, 116–131.

Guo, Q., Park, S., Ma, H., 2012. Microfluidic micropipette aspiration for measuring the deformability of single cells. Lab Chip 12, 2687–2695.

Hallett, F.R., Marsh, J., Nickel, B.G., Wood, J.M., 1993. Mechanical properties of vesicles. II. A model for osmotic swelling and lysis. Biophysical Journal 64, 435–442.

Hasan, M., Karal, M.A.S., Levadnyy, V., Yamazaki, M., 2018a. Mechanism of Initial Stage of Pore Formation Induced by Antimicrobial Peptide Magainin 2. Langmuir 34, 3349–3362.

Hasan, M., Moghal, M.M.R., Saha, S.K., Yamazaki, M., 2019. The role of membrane tension in the action of antimicrobial peptides and cell-penetrating peptides in biomembranes. Biophys Rev 11, 431–448.

Hasan, M., Saha, S.K., Yamazaki, M., 2018b. Effect of membrane tension on transbilayer movement of lipids. The Journal of Chemical Physics 148, 245101.

Heyman, N.S., Burt, J.M., 2008. Hindered Diffusion through an Aqueous Pore Describes Invariant Dye Selectivity of Cx43 Junctions. Biophysical Journal 94, 840–854.

Hirsh, D.J., Hammer, J., Maloy, W.L., Blazyk, J., Schaefer, J., 1996. Secondary Structure and Location of a Magainin Analogue in Synthetic Phospholipid Bilayers. Biochemistry 35, 12733–12741.

Hochmuth, R.M., 2000. Micropipette aspiration of living cells. Journal of Biomechanics 33, 15–22.

Hoffmann, W., Richter, K., Kreil, G., 1983. A novel peptide designated PYLa and its precursor as predicted from cloned mRNA of Xenopus laevis skin. The EMBO Journal 2, 711–714.

Hossain, F., Billah, M.M., Yamazaki, M., 2022. Single-Cell Analysis of the Antimicrobial and Bactericidal Activities of the Antimicrobial Peptide Magainin 2. Microbiology Spectrum 10, e00114-22.

Hossain, F., Dohra, H., Yamazaki, M., 2021. Effect of Membrane Potential on Entry of Lactoferricin B-Derived 6-Residue Antimicrobial Peptide into Single Escherichia coli Cells and Lipid Vesicles. Journal of Bacteriology 203, 10.1128/jb.00021-21.

Hossain, F., Moghal, M.M.R., Islam, M.Z., Moniruzzaman, M., Yamazaki, M., 2019. Membrane potential is vital for rapid permeabilization of plasma membranes and lipid bilayers by the antimicrobial peptide lactoferricin B. Journal of Biological

Chemistry 294, 10449–10462.

Hossein, A., Deserno, M., 2020. Spontaneous Curvature, Differential Stress, and Bending Modulus of Asymmetric Lipid Membranes. Biophysical Journal 118, 624–642.

Huang, H.W., 1995. Elasticity of Lipid Bilayer Interacting with Amphiphilic Helical Peptides. J. Phys. II France 5, 1427–1431.

Islam, M.Z., Ariyama, H., Alam, J.M., Yamazaki, M., 2014. Entry of Cell-Penetrating Peptide Transportan 10 into a Single Vesicle by Translocating Across Lipid Membrane and Its Induced Pores. Biochemistry 53, 386–396.

Islam, M.Z., Hossain, F., Ali, M.H., Yamazaki, M., 2023. Relationship between antimicrobial peptides-induced cell membrane damage and bactericidal activity. Biophysical Journal 122, 4645–4655.

Islam, M.Z., Sharmin, S., Levadnyy, V., Shibly, S.U.A, Yamazaki, M., 2017. Effects of Mechanical Properties of Lipid Bilayers on the Entry of Cell-Penetrating Peptides into Single Vesicles. Langmuir 33, 2433–2443.

Islam, M.Z., Sharmin, S., Moniruzzaman, M., Yamazaki, M., 2018. Elementary processes for the entry of cell-penetrating peptides into lipid bilayer vesicles and bacterial cells. Appl Microbiol Biotechnol 102, 3879–3892.

Israelachvili, J.N., 2011. Intermolecular and Surface Forces, 3rd edition. ed. Academic Press, Burlington (Mass.).

Jähnig, F., 1976. Electrostatic free energy and shift of the phase transition for charged lipid membranes. Biophysical Chemistry 4, 309–318.

Karal, M.A.S., Alam, J.M., Takahashi, T., Levadny, V., Yamazaki, M., 2015a. Stretch-Activated Pore of the Antimicrobial Peptide, Magainin 2. Langmuir 31, 3391–3401.

Karal, M.A.S., Levadnyy, V., Tsuboi, T., Belaya, M., Yamazaki, M., 2015b. Electrostatic interaction effects on tension-induced pore formation in lipid membranes. Phys. Rev. E 92, 012708.

Karal, M.A.S., Levadnyy, V., Yamazaki, M., 2016. Analysis of constant tension-induced rupture of lipid membranes using activation energy. Phys. Chem. Chem. Phys. 18, 13487–13495.

Karal, M.A.S., Yamazaki, M., 2015. Communication: Activation energy of tension-induced pore formation in lipid membranes. The Journal of Chemical Physics 143, 081103.

Karatekin, E., Sandre, O., Guitouni, H., Borghi, N., Puech, P.-H., Brochard-Wyart, F., 2003. Cascades of Transient Pores in Giant Vesicles: Line Tension and Transport. Biophysical Journal 84, 1734–1749.

Kinoshita, K., Li, S., Yamazaki, M., 2001. The mechanism of the stabilization of the hexagonal II (HII) phase in phosphatidylethanolamine membranes in the presence of low concentrations of dimethyl sulfoxide. Eur Biophys J 30, 207–220.

Kollmitzer, B., Heftberger, P., Rappolt, M., Pabst, G., 2013. Monolayer spontaneous curvature of raft-forming membrane lipids. Soft Matter 9, 10877–10884.

Levadny, V., Tsuboi, T., Belaya, M., Yamazaki, M., 2013. Rate Constant of Tension-Induced Pore Formation in Lipid Membranes. Langmuir 29, 3848–3852.

Levadnyy, V., Hasan, M., Saha, S.K., Yamazaki, M., 2019. Effect of Transmembrane Asymmetric Distribution of Lipids and Peptides on Lipid Bilayers. J. Phys. Chem. B 123, 4645–4652.

Levina, N., Tötemeyer, S., Stokes, N.R., Louis, P., Jones, M.A., Booth, I.R., 1999. Protection of Escherichia coli cells against extreme turgor by activation of MscS and MscL mechanosensitive channels: identification of genes required for MscS activity. The EMBO Journal 18, 1730–1737.

Li, F., Chan, C.U., Ohl, C.D., 2014. Rebuttal to a Comment by Richard E. Waugh on our Article “Yield Strength of Human Erythrocyte Membranes to Impulsive Stretching.” Biophysical Journal 106, 1832–1833.

Li, S.J., Yamashita, Y., Yamazaki, M., 2001. Effect of Electrostatic Interactions on Phase Stability of Cubic Phases of Membranes of Monoolein/Dioleoylphosphatidic Acid Mixtures. Biophysical Journal 81, 983–993.

Lin, J., Alexander-Katz, A., 2016. Probing Lipid Bilayers under Ionic Imbalance. Biophysical Journal 111, 2460–2469.

Lowe, L.A., Kindt, J.T., Cranfield, C., Cornell, B., Macmillan, A., Wang, A., 2022. Subtle changes in pH affect the packing and robustness of fatty acid bilayers. Soft Matter 18, 3498–3504.

Ludtke, S.J., He, K., Heller, W.T., Harroun, T.A., Yang, L., Huang, H.W., 1996. Membrane Pores Induced by Magainin. Biochemistry 35, 13723–13728.

Marsh, D., 2007. Lateral Pressure Profile, Spontaneous Curvature Frustration, and the Incorporation and Conformation of Proteins in Membranes. Biophysical Journal 93, 3884–3899.

Marsh, Derek, 1996. Lateral pressure in membranes. Biochimica et Biophysica Acta (BBA) - Reviews on Biomembranes 1286, 183–223.

Marsh, D., 1996. Intrinsic curvature in normal and inverted lipid structures and in membranes. Biophysical Journal 70, 2248–2255.

Matsuki, H., Goto, M., Tamai, N., 2019. Membrane States of Saturated Glycerophospholipids: A Thermodynamic Study of Bilayer Phase Transitions. Chemical and Pharmaceutical Bulletin 67, 300–307.

Matsuzaki, K., Mitani, Y., Akada, K., Murase, O., Yoneyama, S., Zasloff, M., Miyajima, K., 1998. Mechanism of Synergism between Antimicrobial Peptides Magainin 2 and PGLa. Biochemistry 37, 15144–15153.

Melo, M.N., Ferre, R., Castanho, M.A.R.B., 2009. Antimicrobial peptides: linking partition, activity and high membrane-bound concentrations. Nat Rev Microbiol 7, 245–250.

Moghal, M.M.R., Hossain, F., Yamazaki, M., 2020. Action of antimicrobial peptides and cell-penetrating peptides on membrane potential revealed by the single GUV method. Biophys Rev 12, 339–348.

Moghal, M.M.R., Islam, M.Z., Hossain, F., Saha, S.K., Yamazaki, M., 2020. Role of Membrane Potential on Entry of Cell-Penetrating Peptide Transportan 10 into Single Vesicles. Biophysical Journal 118, 57–69.

Montal, M., 1995. Design of Molecular Function: Channels of Communication. Annual Review of Biophysics 24, 31–57.

Mou, Q., Xu, M., Deng, J., Hu, N., Yang, J., 2023. Studying the roles of salt ions in the pore initiation and closure stages in the biomembrane electroporation. APL Bioengineering 7, 026103.

Mui, B.L., Cullis, P.R., Evans, E.A., Madden, T.D., 1993. Osmotic properties of large unilamellar vesicles prepared by extrusion. Biophysical Journal 64, 443–453.

Needham, D., Nunn, R.S., 1990. Elastic deformation and failure of lipid bilayer membranes containing cholesterol. Biophysical Journal 58, 997–1009.

Park, C.B., Yi, K.-S., Matsuzaki, K., Kim, M.S., Kim, S.C., 2000. Structure–activity analysis of buforin II, a histone H2A-derived antimicrobial peptide: The proline hinge is responsible for the cell-penetrating ability of buforin II. Proceedings of the National Academy of Sciences 97, 8245–8250.

Parvez, F., Alam, J.M., Dohra, H., Yamazaki, M., 2018. Elementary processes of antimicrobial peptide PGLa-induced pore formation in lipid bilayers. Biochimica et Biophysica Acta (BBA)-Biomembranes 1860, 2262–2271.

Petelska, A.D., Figaszewski, Z.A., 2002. Interfacial tension of bilayer lipid membrane formed from phosphatidylethanolamine. Biochimica et Biophysica Acta (BBA) - Biomembranes 1567, 79–86.

Polozov, I.V., Anantharamaiah, G.M., Segrest, J.P., Epand, R.M., 2001. Osmotically Induced Membrane Tension Modulates Membrane Permeabilization by Class L Amphipathic Helical Peptides: Nucleation Model of Defect Formation. Biophysical Journal 81, 949–959.

Propheter, D.C., Chara, A.L., Harris, T.A., Ruhn, K.A., Hooper, L.V., 2017. Resistin-like molecule β is a bactericidal protein that promotes spatial segregation of the microbiota and the colonic epithelium. Proceedings of the National Academy of Sciences 114, 11027–11033.

Rand, R.P., Fuller, N.L., Gruner, S.M., Parsegian, V.A., 1990. Membrane curvature, lipid segregation, and structural transitions for phospholipids under dual-solvent stress. Biochemistry 29, 76–87.

Rand, R.P., Parsegian, V.A., 1989. Hydration forces between phospholipid bilayers. Biochimica et Biophysica Acta (BBA) - Reviews on Biomembranes 988, 351–376.

Rangamani, P., 2022. The many faces of membrane tension: Challenges across systems and scales. Biochimica et Biophysica Acta (BBA) - Biomembranes 1864, 183897.

Raval, J., Iglič, A., Góźdź, W., 2021. Investigation of Shape Transformations of Vesicles, Induced by Their Adhesion to Flat Substrates Characterized by Different Adhesion Strength. International Journal of Molecular Sciences 22, 13406.

Rawicz, W., Olbrich, K.C., McIntosh, T., Needham, D., Evans, E., 2000. Effect of Chain Length and Unsaturation on Elasticity of Lipid Bilayers. Biophysical Journal 79, 328–339.

Sachs, F., 2010. Stretch-Activated Ion Channels: What Are They? Physiology 25, 50–56.

Saha, S.K., Shibly, S.U.A, Yamazaki, M., 2020. Membrane Tension in Negatively Charged Lipid Bilayers in a Buffer under Osmotic Pressure. J. Phys. Chem. B 124, 5588–5599.

Sandre, O., Moreaux, L., Brochard-Wyart, F., 1999. Dynamics of transient pores in stretched vesicles. Proceedings of the National Academy of Sciences 96, 10591–10596.

Schroeder, B.O., Wu, Z., Nuding, S., Groscurth, S., Marcinowski, M., Beisner, J., Buchner, J., Schaller, M., Stange, E.F., Wehkamp, J., 2011. Reduction of disulphide bonds unmasks potent antimicrobial activity of human β-defensin 1. Nature 469, 419–423.

Seddon, J.M., Templer, R.H., 1995. Chapter 3 - Polymorphism of Lipid-Water Systems, in: Lipowsky, R., Sackmann, E. (Eds.), Handbook of Biological Physics, Structure and Dynamics of Membranes. North-Holland, pp. 97–160.

Sharmin, S., Islam, M.Z., Karal, M.A.S., Shibly, S.U.A, Dohra, H., Yamazaki, M., 2016. Effects of Lipid Composition on the Entry of Cell-Penetrating Peptide Oligoarginine into Single Vesicles. Biochemistry 55, 4154–4165.

Shibly, S.U.A., Ghatak, C., Karal, M.A.S, Moniruzzaman, M., Yamazaki, M., 2016. Experimental Estimation of Membrane Tension Induced by Osmotic Pressure. Biophysical Journal 111, 2190–2201.

Shkulipa, S.A., den Otter, W.K., Briels, W.J., 2006. Thermal Undulations of Lipid Bilayers Relax by Intermonolayer Friction at Submicrometer Length Scales. Phys. Rev. Lett. 96, 178302.

Sochacki, K.A., Barns, K.J., Bucki, R., Weisshaar, J.C., 2011. Real-time attack on single Escherichia coli cells by the human antimicrobial peptide LL-37. Proceedings of the National Academy of Sciences 108, E77–E81.

Strandberg, E., Tremouilhac, P., Wadhwani, P., Ulrich, A.S., 2009. Synergistic transmembrane insertion of the heterodimeric PGLa/magainin 2 complex studied

by solid-state NMR. Biochimica et Biophysica Acta (BBA) - Biomembranes, Amphibian Antimicrobial Peptides 1788, 1667–1679.

Sukharev, S.I., Blount, P., Martinac, B., Blattner, F.R., Kung, C., 1994. A large-conductance mechanosensitive channel in E. coli encoded by mscL alone. Nature 368, 265–268.

Tamba, Y., Ariyama, H., Levadny, V., Yamazaki, M., 2010. Kinetic Pathway of Antimicrobial Peptide Magainin 2-Induced Pore Formation in Lipid Membranes. J. Phys. Chem. B 114, 12018–12026.

Tamba, Y., Terashima, H., Yamazaki, M., 2011. A membrane filtering method for the purification of giant unilamellar vesicles. Chemistry and Physics of Lipids 164, 351–358.

Tamba, Y., Yamazaki, M., 2009. Magainin 2-Induced Pore Formation in the Lipid Membranes Depends on Its Concentration in the Membrane Interface. J. Phys. Chem. B 113, 4846–4852.

Tamba, Y., Yamazaki, M., 2005. Single Giant Unilamellar Vesicle Method Reveals Effect of Antimicrobial Peptide Magainin 2 on Membrane Permeability. Biochemistry 44, 15823–15833.

Tazawa, K., Yamazaki, M., 2023. Effect of monolayer spontaneous curvature on constant tension-induced pore formation in lipid bilayers. The Journal of Chemical Physics 158, 081101.

Tolpekina, T.V., Den Otter, W.K., Briels, W.J., 2004. Nucleation free energy of pore formation in an amphiphilic bilayer studied by molecular dynamics simulations. The Journal of Chemical Physics 121, 12060–12066.

Träuble, H., Eibl, H., 1974. Electrostatic Effects on Lipid Phase Transitions: Membrane Structure and Ionic Environment. Proceedings of the National Academy of Sciences 71, 214–219.

Tremouilhac, P., Strandberg, E., Wadhwani, P., Ulrich, A.S., 2006. Synergistic Transmembrane Alignment of the Antimicrobial Heterodimer PGLa/Magainin *. Journal of Biological Chemistry 281, 32089–32094.

University of Nebraska Medical Center. Antimicrobial Peptide Database (APD3). https://aps.unmc.edu/ (accessed Apr 25, 2024)

Vaz Gomes, A., de Waal, A., Berden, J.A., Westerhoff, H.V., 1993. Electric potentiation, cooperativity, and synergism of magainin peptides in protein-free liposomes. Biochemistry 32, 5365–5372.

Wade, D., Boman, A., Wåhlin, B., Drain, C.M., Andreu, D., Boman, H.G., Merrifield, R.B., 1990. All-D amino acid-containing channel-forming antibiotic peptides. Proceedings of the National Academy of Sciences 87, 4761–4765.

Wakabayashi, H., Matsumoto, H., Hashimoto, K., Teraguchi, S., Takase, M., Hayasawa, H., 1999. N-Acylated and d Enantiomer Derivatives of a Nonamer Core Peptide of Lactoferricin B Showing Improved Antimicrobial Activity. Antimicrobial Agents and Chemotherapy 43, 1267–1269.

Williams, R.W., Starman, R., Taylor, K.M.P., Gable, K., Beeler, T., Zasloff, M., Covell, D., 1990. Raman spectroscopy of synthetic antimicrobial frog peptides magainin 2a and PGLa. Biochemistry 29, 4490–4496.

Wohlert, J., den Otter, W.K., Edholm, O., Briels, W.J., 2006. Free energy of a trans-membrane pore calculated from atomistic molecular dynamics simulations. The Journal of Chemical Physics 124, 154905.

Yamazaki, M., 2009. Chapter 7 Transformation Between Liposomes and Cubic Phases of Biological Lipid Membranes Induced by Modulation of Electrostatic Interactions, in: Advances in Planar Lipid Bilayers and Liposomes, Advances in Planar Lipid Bilayers and Liposomes. Academic Press, pp. 163–209.

Yamazaki, M., 2008. Chapter 5 The Single Guv Method to Reveal Elementary Processes of Leakage of Internal Contents from Liposomes Induced by Antimicrobial Substances, in: Advances in Planar Lipid Bilayers and Liposomes. Academic Press, pp. 121–142.

Yeaman, M.R., Yount, N.Y., 2003. Mechanisms of Antimicrobial Peptide Action and Resistance. Pharmacol Rev 55, 27–55.

Zasloff, M., 2002. Antimicrobial peptides of multicellular organisms. Nature 415, 389–395.

Zasloff, M., 1987. Magainins, a class of antimicrobial peptides from Xenopus skin: isolation, characterization of two active forms, and partial cDNA sequence of a precursor. Proceedings of the National Academy of Sciences 84, 5449–5453.